Analysis, Design Optimization, and Semi-Active Control of Skid Landing Gear Featuring Bi-Fold Magnetorheological Dampers

Muftah Saleh

A Thesis
In the Department
of
Mechanical, Industrial, and Aerospace Engineering

Presented in Partial Fulfillment of the Requirements
for the Degree of
Doctor of Philosophy (Mechanical Engineering) at
Concordia University
Montreal, Quebec, Canada

November 2017

© Muftah Saleh, 2017

CONCORDIA UNIVERSITY
School of Graduate Studies

This is to certify that the thesis prepared

By: Muftah Saleh

Entitled: Analysis, Design Optimization, and Semi-Active Control of Skid Landing Gear Featuring Bi-Fold Magnetorheological Dampers

and submitted in partial fulfillment of the requirements for the degree of

Doctor of Philosophy (Mechanical Engineering)

complies with the regulations of the University and meets the accepted standards with respect to originality and quality.

Signed by the final Examining Committee:

_____ Chair

Dr. G. Gopakumar

_____ External Examiner

Dr. Amir Khajepour

_____ External to Program

Dr. Khaled Galal

_____ Examiner

Dr. Ion Stiharu

_____ Examiner

Dr. Wen-Fang Xie

_____ Thesis Co-supervisor

Dr. Rama Bhat

_____ Thesis Co-supervisor

Dr. Ramin Sedaghati

Approved by: _____

Dr. A. Dolatabadi, Graduate Program Director

Dean of Faculty: _____

Dr. Amir Asif, Dean

Faculty of Engineering and Computer Science

15 November 2017

Abstract

Analysis, Design Optimization, and Semi-Active Control of Skid Landing Gear Featuring Bi-Fold Magnetorheological Dampers

Muftah Saleh, Ph.D.
Concordia University, 2017.

Providing safer environment and minimizing the fatalities during helicopter harsh impacts and crashes have been a concern to scientists, engineers, and the regulating agencies since the dawn of helicopter industry. Tremendous efforts have been devoted to enhance the crashworthiness capabilities of helicopter's skid landing gear (SLG) system. These efforts have been aiming to improve the energy absorption capabilities of the conventional SLG designs while maintaining minimum weight and adequate strength to comply with the airworthiness requirements. The emerging of smart materials and the advances in control engineering have provided a new horizon to design lightweight landing gears with enhanced energy absorption capacity.

In this context, the main objectives of the present dissertation research are to investigate the crashworthiness performance of the conventional SLG; to formulate a design optimization strategy to design light-weight SLG with enhanced energy absorption capacity and finally to propose an adaptive SLG utilizing bi-fold magnetorheological dampers in an attempt to exceed the requirements of the crashworthiness specifications for skid landing gear systems while minimizing the level of sudden acceleration experienced by the aircraft occupants in the event of impact. The present research consists of four synergistically related phases. In the first phase, the dynamic response analysis has been conducted on the baseline conventional skid landing gear system in order to assess its capabilities and to establish a reference benchmark for the subsequent work. In the second phase, a design optimization strategy has been formulated to identify the optimal cross sectional dimensions of the round shaped crosstubes in the SLG system to maximize their energy absorption at sink rate of 2.44 m/s and to minimize the crosstubes mass. The optimization results showed that the specific energy absorption of the design optimized SLG could be substantially increased by 35% compared to that of baseline design and the crosstubes mass was decreased by

24.5%. Deign curves and guidelines have also been presented to directly determine the required effective mass of the helicopter and the corresponding desired maximum deflection of the helicopter under given sink rate and different values of rotor lift factor.

In the third phase, governing equations to predict the damping force and dynamic range of a bi-fold magnetorheological energy absorber (MREA) under impact have been presented. To predict the behavior of the MREA more accurately under high impact velocities, the Bingham plastic model with minor loss factors (BPM) has been incorporated in the problem formulation. The optimal geometrical parameters of the candidate bi-fold magnetorheological energy absorber (MREA) under volume constraint to maximize the damping force at piston velocity of 5 m/s have then been presented. Results showed a dynamic range of around two has been attained at this design speed. The proposed optimization problem has been solved using combined stochastic based (Genetic Algorithm) and nonlinear mathematical programming (Sequential Quadratic Programming Algorithm) techniques.

In the fourth phase, the MREA device model has been incorporated in a single degree of freedom helicopter model to assess the performance of the adaptive SLG system. The comparison of the responses revealed that the proposed adaptive SLG equipped with the MREA could minimize the induced acceleration while utilizing the full energy absorption stroke without encountering end-stop impact. The MREA performance was evaluated in terms of Bingham numbers for compression and rebound strokes. New optimum Bingham numbers-rotor lift factor chart has been introduced to control the generation of the required damping force based on the activated rotor lift force. Finally, to investigate the closed-loop performance of the tuneable MREA in the SLG system, a simple semi-active control strategy has been presented. The semi-active controller was designed based on the optimum Bingham numbers identified previously. Using the values of the velocity at the impact instant and the mass of the helicopter, the controller evaluates the required current for the MREA to generate desired yield force.

Dedication

I dedicate this thesis to

My parents

for their endless support and encouragement

My wife

for her patience and incredible support

My lovely children

for their support and encouragement

ACKNOWLEDGMENT

All praise and thanks to Allah the exalted, the Lord of the universe, who guided me alone and made all things easy and possible to be realized by His majesty.

I wish to express my sincere thanks and gratitude to my supervisors Dr. Ramin Sedaghati and Dr. Rama Bhat for their guidance, continuous supervision and support throughout the research and the rest of the course of my study at Concordia University. Their enthusiasm and interest in the work have been very encouraging. I would never forget their attitude and efforts to overcome the obstacles of the research. This thesis would not have been possible without their guidance and help.

Special thanks goes also to the Libya Ministry of Education for their trust and continuous financial support during the years of my graduate study at Ph.D. level.

A great thanks go to my beloved parents, my first tutors in life, and siblings for their continued support and prayers.

Gratitude is expressed to my supportive wife, Um Assim, and my wonderful children Warda, Sheima, and Assim, who have made this hard time much more enjoyable. Their encouragement, patience, and helpfulness have motivated me to achieve my ambitions.

Last but not least, may Allah bless us with his love and make this work purely for his sake and bless all we do.

Table of Contents

List of Figures

Chapter 1

Chapter 2

Chapter 3

Chapter 4

List of Tables

Chapter 5

Chapter 6

List of Abbreviations

AWM	Airworthiness manual
BBD	Box-Bechnken design
BP	Bingham plastic model
BPH	Bingham plastic model coupled with low speed hysteresis
BPM	Bingham plastic model with minor loss factors
CCD	Central composite design
DoE	Design of experiment
EA	Energy absorber
EREA	Electrorheological energy absorber
FAR	Federal aviation regulation
FEMM	Finite element magnetic method
GA	Genetic algorithm
HM	Hydro-mechanical model
MIL-STD	Military standard
MREA	Magnetorheological energy absorber
MRF	Magnetorheological fluid
PEEQ	Equivalent plastic strain
RSM	Response surface method
SDOF	Single degree of freedom
SLG	Skid landing gear
SQP	Sequential quadratic programming
TCCA	Transport Canada Civil Aviation

Nomenclatures

A	Inequality constraints in vector form
A_d	Effective area of the MR valve normal the flow, m^2
A_j	Area of the j-th link of the magnetic circuit normal to flux lines, m^2
A_1, A_{1n}, B_2, B_{1n}	Constants
A_p	Effective area of the piston, m^2
A_y	Vertical Acceleration, m/s2
A_τ	Surface area of the equivalent single MR valve, m^2
$A(\zeta)$	Acceleration of the passively damped model, m/s^2
B	Magnetic flux density, T
B_{avg}	Average magnetic flux density, T
Bi	Bingham number
Bi_c	Bingham number for compression stroke
Bi_c^o	Optimum Bingham number for compression stroke
Bi_r	Bingham number for rebound stroke
Bi_r^o	Optimum Bingham number for rebound stroke
B_j	Magnetic flux density of the j-th link of the magnetic circuit, T
$B_{s,sat}$	Saturation magnetic flux density of the bobbin material, T
B_τ	Magnetic flux density in the MR valve volume, T
B(s)	Nodal value of the magnetic flux density, T
$B_{\tau,sat}$	Saturation magnetic flux density of MR fluid, T
b	Bounds of the inequality constraints in vector form
c	Gradient of the cost function; Viscous damping coefficient, N.s/m
C_1, C_2, C_{1n}, C_{2n}	Constants
$c_{e,all}$	Overall equivalent viscous linear damping coefficient, N.s/m
c_{on}	Equivalent damping coefficient of the MR fluid in the on-state, N.s/m
c_q	Coefficient of the quadratic component of the damping force, $N.s^2/m^2$
c_R	Damping coefficient ratio of on-state damping to off-state damping
c_w	Speed of elastic wave, m/s
D	Dynamic range

D_b	Diameter of the equivalent single MR valve, m
D_{b1}	Diameter of inner MR valve, m
D_{b2}	Diameter of outer MR valve, m
D_h	Hydraulic diameter of the MR valve, m
D_i	Diameter of bobbin's core, m
D_{in}	Inner diameter of damper cylinder, m
D_o	Inner diameter of the outer flange, m
D_p	Piston head diameter, m
D_r	Piston rod diameter, m
D_s	Diameter of the MREA cylindrical shell, m
d	Search direction; Thickness of the MR valve, m
E	Modulus of elasticity, Pa
E_b	Total bending energy, J
E_{b_e}	Elastic bending energy, J
$E_{b_{e,y}}$	Elastic bending energy at yield point, J
E_{b_i}	Inelastic bending energy, J
E_{FD}	Frictional dissipation, J
E_{TOT}	Total energy, J
E_{VD}	Viscous dissipation, J
E_W	Work of the external force, J
e	Bounds of the equality constraints in vector form
F	Spring force in the inelastic zone, N; Damping force, N; Fitness function
F_f	Friction force, N
F_{ml}	Damping force due to minor losses, N
F_{off}	Off-state damping force, N
F_{on}	On-state damping force, N
F_y	Stroking load, N
F_τ	MR yield force, N
F_η	Darcy friction viscous damping force
F_{off}	Field-off damping force, N
F_s	Spring force, N

$\bar{F}$	Non-dimensional force
f	Nonlinear component of damping and stiffness forces, N
f_i	Individual cost function
f_{max}	Value of the highest performing individual
$f\{\text{-}\}$	Internal load, N
$\bar{f}$	Quadratic programming subproblem
f_y	Yield force, N
f_{y_c}	Yield force in compression stroke, N
f_{y_r}	Yield force in rebound stroke, N
G_x	Direction of accelerative force parallel to x-axis
G_y	Direction of accelerative force parallel to y-axis
G_z	Direction of accelerative force parallel to z-axis
g	Gravitational acceleration, 9.81 m/s^2
$g(.)$	Inequality constraint
H	Bobbin length, m; magnetic field strength, A/m
h	Height of free fall, m
I	Applied current, A
K	Fluid coefficient
k	Number of sample design points; Linear elastic stiffness, N/m
k_c	Cubic coefficient of the 3rd order term inelastic stiffness, N^3/m^3
k_e	Elastic stiffness, N/m
$k_{e,b}$	Equivalent linear stiffness of the baseline SLG, N/m
$k_{e,o}$	Equivalent Linear stiffness of the optimum SLG, N/m
k_i	Inelastic stiffness, N/m
k_q	Quadratic coefficient of the 2nd order term inelastic stiffness, N^2/m^2
$K_{ml\text{-}i}$	Minor loss coefficient
$\bar{k}$	Stiffness ratio
L	Rotor lift factor; Total active length of the MR valve, m
L_1, L_2, L_{1n}, L_{2n}	Constants
L_{min}	Length of the shortest side of element, m
l	Fraction size; Active length of the MR valve, m

l_c	Length of the coil, m
l_j	Length of the j-th link of the magnetic circuit, m
m	Mass, kg; Fluid coefficient
m_{ct}	Mass of crosstubes, kg
m_e	Effective mass, kg
[M]	Diagonal mass matrix, kg
N	Equality constraints in vector form; Number of wire turns per coil
n	Load factor, g's; Number of design variables; Total number of links
n_{max}	Maximum load factor
p	Number of regression coefficients
$P\{\text{-}\}$	External force, N
Re	Reynolds number
R_t	Total reluctance
R^2	Coefficient of multiple determination
R^2-adj	Adjustable coefficient of multiple determination
S	Maximum permissible stroke of EA, m
s	Number of design points to generate the meta-model
SEA	Specific energy absorption, J/kg
SSE	Error sum of squares
SST	Total sum of squares
sgn (.)	Signum function
t	Time, second
T	Kinetic energy, J
$\bar{t}$	Non-dimensional time
$\bar{t}_c$	Non-dimensional time at the end of the compression stroke
$\bar{t}_r$	Non-dimensional time at the end of the rebound stroke
U	Internal energy, J
V_b	Volume of single bobbin, m^3
V_d	Fluid velocity in the MR valve, m/s
V_p	Piston velocity, m/s
v_0	Impact velocity, m/s

$\bar{v}_0$	Non-dimensional impact velocity
w	Coil width, m
x	Displacement
X	Design variables in matrix form; Specific magnitude of current signal, A
X_0	Initial points in vector form
$X(\zeta)$	Displacement of the passively damped model, m
x	Displacement, m
x_1	External radius of the aft crosstube, m
x_2	Thickness of the aft crosstube, m
x_3	External radius of the forward crosstube, m
x_4	Thickness of the forward crosstube, m
x_i	Design variable
x_j	Design variable
x_L	Lower bound of design variables, m
x_U	Upper bound of design variables, m
$\dot{x}$	Velocity, m/s
$\ddot{x}$	Acceleration, m/s^2
$\bar{x}$	Non-dimensional displacement
$\dot{\bar{x}}$	Non-dimensional velocity
$\ddot{\bar{x}}$	Non-dimensional acceleration
y	True response in vector form
y_i	True individual output response
$\bar{y}$	Averaged true response
$\hat{y}$	Approximated response in vector form
ω_n	Undamped natural frequency, rad/s^2
ω_d	Damped natural frequency, rad/s^2
$\bar{\omega}_d$	Non-dimensional damped natural frequency
η	Field-independent viscosity of MR fluid, Pa-s
η_e	Elastic viscosity of MR fluid, Pa-s
β	Regression coefficients in vector form; Scaling factor

$\beta_0, \beta_j, \beta_{ij}, \beta_{jj}$	Regression coefficients
γ	Scaling factor
$\dot{\gamma}$	Shear strain rate, s^{-1}
ζ	Damping ratio
δ	Deflection, m
δ_{max}	Maximum deflection, m
δ_{st}	Static deflection of the spring, m
$\bar{\delta}_{st}$	Non-dimensional static deflection
δ_y	Yield deflection, m
ρ	Density of the MR fluid, kg/m^3
$\varnothing$	Magnetic flux, T
α	Coefficient
τ	Shear stress, Pa
τ_y	Yield stress, Pa
$\tau_{y,max}$	Maximum yield stress, Pa
μ	Permeability, N/A^2
μ_s	Permeability of the bobbin material, N/A^2
μ_τ	Permeability of the MR fluid, N/A^2
$\sigma_1,\sigma_2,\sigma_3$	Principle stresses, Pa
σ_v	von Mises stress, Pa
$\sigma_{\dot{x}}$	Root mean square value of velocity, m/s
σ_y	Yield stress, Pa
ε	Error in vector form; Surface roughness, Control gain
ε_1	Uniaxial strain
ε_p	Equivalent plastic strain
ρ	Density, kg/m^3
Δt	Time step, second
ΔP_{ml}	Viscous pressure drop due to minor losses, Pa
ΔP_η	Viscous pressure drop due to Darcy friction, Pa

ΔP_τ	Pressure drop due to MR effect, Pa

Superscript

i	Increment counter
T	Transpose

CHAPTER 1

Introduction and Literature Review

Military Standard 1290 [7] defines the term “aircraft crashworthiness” as the “ability of an airframe structure to maintain a protective shell around occupants during a crash and minimize accelerations applied to the occupiable portion of the aircraft during crash impacts”. The vehicles are required to provide an adequate level of energy absorption to dissipate tremendous amount of impact energy. This alleviates the fatality and the seriousness of the injuries due to exposure of the passengers/occupants to undesirable high accelerative forces. The vehicle occupants having upper torso restrained can tolerate different magnitudes of sudden acceleration based on the impact magnitude and direction. The successful crashworthy design is the design that attenuates the resultant impact forces, for the given design envelope, to minimize the fatality and severity of the injury in the crash. The helicopter is generally designed to provide energy dissipation capabilities in three typical crashworthy systems, namely, the landing gear, the fuselage sub-floor structure, and the occupant seat. The following two sections discuss briefly the human tolerance to abrupt acceleration and the crashworthy systems of a helicopter.

1.1 Human body tolerance to abrupt acceleration

Numerous experimental studies have been conducted to evaluate the whole human body resistance to sudden acceleration force, see for example [1-5]. The collected data are made available to engineers and agencies to be implemented as guidelines for design, testing, and certification of the crashworthy structural elements and systems. It has been found that the survivability of the occupant in the event of an impact is influenced by the following five external factors [1]:

1- Magnitude of the acceleration: The higher the magnitude, the occupant is more vulnerable to injury.
2- Direction: The human body tolerates the uttermost acceleration in the forward direction such as in frontal impact of a vehicle. The least tolerable acceleration is in the vertical direction for the seated occupant.

3- Duration: for the same magnitude of the acceleration, the human body can tolerate more abrupt acceleration for the shorter pulse. The duration of crash usually does not exceed 250 milliseconds while the other prolonged accelerations have longer period.
4- Rate of onset: rate of onset characterizes the rapidity of the application of the acceleration and it is equivalent to the slope of the acceleration pulse between the point of initiation and the peak acceleration. The steeper the slope the less tolerable the acceleration. For the human body the rate of onset is limited between 3 to 20 g/second [5].
5- Position/Restraint/Support: The degree of restraint determines how much load is distributed over the body in the event of crash. When the body is fully restrained, the crash load is distributed over a larger surface. On the other hand, more relaxation of the restraints reduces the surface exposed to impact loads, hence increases the acceleration experienced by the occupant.

Table 1.1 summarizes the magnitude of the sudden acceleration, measured in g's, that is bearable by the human body in the positive and negative directions along the three principal axes. Furthermore, the Eiband curve for abrupt upward acceleration is presented in Figure. 1.2. The Figure shows that the fully restrained human body is vulnerable to abrupt acceleration in the vertical impact ($-G_z$) [2]. In this case the spinal column can sustain up to 15 g's for pulses lasting up to approximately 40 milliseconds without being exposed to moderate or severe injuries. Table 1.1 and Figure 1.2 reveal that the damage of the spinal column is most likely to occur when the acceleration load reaches an approximate value of 20-25 g's [1].

Table 1.1. Human body tolerance to sudden acceleration [4].

Direction of accelerative force	Occupant's inertia response	Tolerance level, g's
Headward ($+G_z$)	Eyeballs down	20-25
Tailward ($-G_z$)	Eyeballs up	15
Lateral right ($+G_y$)	Eyeballs left	20
Lateral left ($-G_y$)	Eyeballs right	20
Neck to chest ($+G_x$)	Eyeballs out	45
Chest to neck ($-G_x$)	Eyeballs in	45

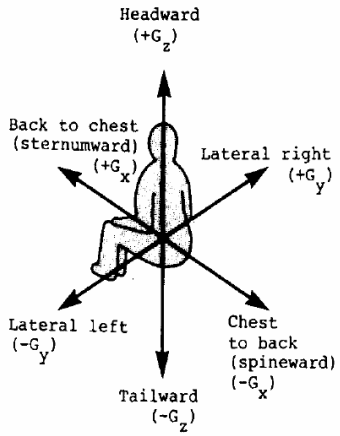

Fig. 1.1. Directions of forces on human body [1].

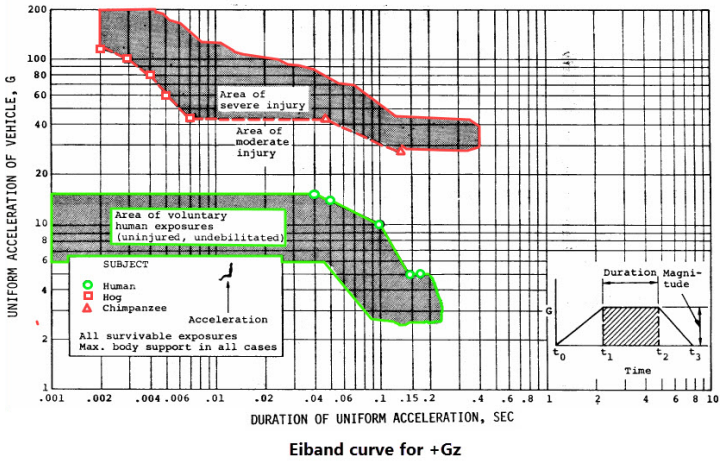

Fig. 1.2. Eiband curve for upward vertical acceleration [1].

1.2 Crashworthiness specifications

The differences in the nature of missions of diverse types of helicopters, such as civil, navy, and army helicopters, have led to the establishment of category-specific crashworthiness requirements. These requirements are distinguished by impact speed and direction, weight, attitude of the helicopters with respect to the terrain, type of mission, etc. In addition to airworthiness requirements, each crashworthy system of the helicopter has to meet the respective crashworthiness requirements. The crashworthy systems are: landing gear, fuselage sub-floor structure, and occupant seat. For instance, the certification requirements of skid landing gears (SLGs) incorporated in civilian helicopters are less strict than those of the military counterpart.

Chapter 527 of Airworthiness Manual (AWM) of Transport Canada Civil Aviation (TCCA) and Part 27 of the United States Federal Aviation Regulations (FARs) for normal category helicopter require that the landing gear be able to endure 2.44 m/s reserve energy drop test and 2.0 m/s limit load drop test at level attitudes [6]. In the limit load drop test, a rotor lift force equivalent to 67% of the rotorcraft maximum weight is applied at the instant of touchdown whereas in the reserve energy test the rotor lift force is set equal to the full weight of the helicopter at landing. On the contrary, the landing gears of the military rotorcrafts are designed to tolerate higher impact loads at higher impact velocity and at different attitudes (level, pitch, and roll). In this context, the U.S. Army's military standard, MIL-STD-1290(A)AV [7], entails rigorous crashworthiness requirements for the rotary wing aircrafts. It requires that the landing gear be capable of decelerating the helicopter at maximum sink rate of 6.1 m/s and rotor lift to weight ratio of unity at level attitude. In the meanwhile, no contact is permitted between the fuselage and ground and no damage to the remainder structure of the aircraft is allowed except the landing gear and the rotor blades. A rotor lift factor, L is defined as [6]

$$L = \frac{\text{Rotor lift force}}{\text{Helicopter weight}} \tag{1.1}$$

The variation in the rotor lift factor (L) represents the contribution of upward rotor lift force to mitigate the acceleration transmitted to the occupants by reducing or eliminating the potential energy to be absorbed by the crosstubes. This objective can be achieved by increasing the rotor lift force or L. The Concept of using L in drop tests is further discussed in the subsequent chapter.
Due to the limited energy absorption capabilities of the conventional SLG systems, their performance can be further enhanced by incorporating external energy absorption devices such as dampers to meet or even exceed the requirements of the crashworthiness standards over a wider range of sink rates.

1.3 Crashworthy systems of helicopters

In the event of vertical impact, the helicopter attenuates the impact force by the landing gear, sub-floor structure, and energy absorption seats. It is typically expected that about 50% of the impact energy is dissipated by the landing gear, 15% by the sub-floor structure, and the remainder is dissipated by the energy absorbing seats [8]. Unlike the commercial/passenger airplanes, the

limited amount of energy dissipated by the helicopter's sub-floor structure is due to the inadequacy of the crushable structure in the vertical direction. Therefore, the energy dissipation mechanism in helicopters relies more on landing gear than on the other two sub-systems. For lightweight helicopter, the landing gear is usually of the skid type due to its structural simplicity and cost effectiveness. The conventional skid landing gear, illustrated in Figure 1.3, consists of two crosstubes connected to the fuselage by four attachments, and two skids run parallel to the helicopter's longitudinal axis and attached to the either end of the crosstubes. The skids provide stability to the crosstubes during the landing and are used in ground handling. The four attachments are non-slender beams which are made from rigid material having strength numerously higher than that of the crosstubes' material. This ensures utilization of the entire stroke of the crossmembers to maximize the absorption of the impact energy by bending before the crosstubes collapse. The excessive energy is then dissipated through a controlled crushing of the sub-floor structure simultaneously with the controllable displacement of the crashworthy occupant seat. Nevertheless, the energy dissipation capabilities of the fuselage sub-floor structure and the seats are limited due to the short depth of the fuselage's sub-floor structure and the relatively short stroke of the occupant seat. In order to preserve adequate volume around the occupants in the compartment, avoid severe damage to the fuselage during and post the impact, and assure no accelerative forces are transmitted in excess of human tolerance, several state-of-the-art techniques and devices have been developed. These devices are designed to meet the requirements of the crashworthiness regulations for different categories of helicopters. Since the objective of this research is to improve

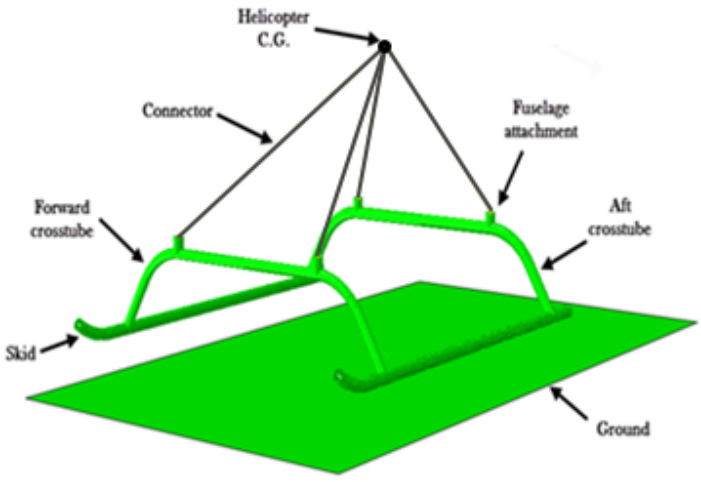

Fig. 1.3. Schematic of the conventional skid landing

the energy absorption capability of the SLGs, more emphasis and elaboration will be devoted to different configurations of these types of gears.

1.3.1 Conventional skid landing gear

The conventional skid landing gears are usually employed in the normal category helicopters which weigh around 3175 kg (7000 lb) or less as defined in Part 27 of FARs [9]. In realistic crash scenarios, the helicopter may fall from 15-30 m height so that the passengers may experience sudden acceleration in range of 60 to 100 g's [8]. To meet the certification requirements stated in [7] and [9], SLGs must be designed, analyzed and drop tested to endure sink velocity of 2.0 m/s with load factor of L = 2/3 and also to endure sink velocity of 2.44 m/s with L = 1.0 all at level attitude. For impact velocity beyond 2.44 m/s, the SLG may incorporate additional energy dissipation means such as impact dampers. The energy dissipation mechanism of the conventional SLG is generally by the bending of its flexural members, i.e. the crosstubes. To dissipate tremendous amount of energy, the SLG is permitted to deform plastically. Under all circumstances, the fuselage should remain intact and does not come in contact with the terrain. However, the crosstubes have limited energy dissipation capability, which is solely dependent on the size and the elasto-plastic characteristics of the crosstube material. From the crashworthiness perspective, the strength of the cross members plays an important role in sustaining the impact loads. Therefore, the SLG has neither to be very stiff nor soft beyond certain design limits. In other words, if the skid gear is very stiff, tremendous accelerative loads could be transmitted to the passengers. On the contrary, very soft SLG structure may fail without being able to absorb reasonable amount of impact energy. In this case, the consequence is a transfer of high impact force to the passengers by the contact between the sub-floor and the ground. From the structural strength perspective, it is recommended to maintain the limit load factor (n) in the range between negative 1.0 to positive 3.5 g's [9]. The limit load factor is a measure of the amount of the load that can be sustained by the structure. The above range ensures that the developed stresses do not exceed the structural strength of the fuselage. Therefore, the SLG should be optimized to increase its energy absorption capacity without compromising the airworthiness requirements. In this case, the load factor is considered as a performance limit and can be expressed as [9]:

$$n = \frac{m_e}{m}\left(\frac{A_y + g}{g}\right) + L \tag{1.2}$$

where

m_e : Effective mass of the helicopter,

m : Maximum gross mass,

A_y : Maximum vertical acceleration of the helicopter at touchdown,

g : Acceleration of gravity (9.81 m/s^2), and

L : Rotor lift load factor.

Literature on the analysis and testing of skid landing gears is, however, limited. Minderhoud [6] used nonlinear explicit finite element (FE) software LS-DYNA to investigate the response of a sleigh type skid landing gear developed by Bell Helicopter. Correlation of the maximum reaction loads predicted by LS-DYNA with those obtained in limit load and reserve energy tests was very good with error ranging from negative 2% to positive 4%. Mikhailov *et al*. [10] suggested an analytical technique for calculating the stress-strain state of a circular cross-sectional skid landing gear during level landing. In their study, the geometry and material nonlinearities were taken into consideration. They extended the study to include the second landing impact. The percentage of error in the magnitudes of the reaction force between the numerical and the experimental results was found less than 10%. Chernoff [11] employed numerical technique to calculate the bending energy in the crosstubes considering two types of material models, bilinear elasto-plastic and perfectly plastic materials. The analytical results were validated with a drop test results and the difference was found within 6%. Tho *et al*. [12] employed LS-DYNA software to simulate the response of skid landing gear of UH-1Y helicopter in a drop test. Four landing attitudes were simulated; level landing, landing with drag, rolled attitude landing, and level landing with sideward obstruction. By modeling the skid gear as beam elements instead of shell elements, the simulation time was reduced from 1 to 2 days period to 12 minutes with appreciative accuracy. The simulation results were favorably compared with drop test data conducted at Bell Helicopter Textron. Sareen *et al*. [13] used MSC/DYTRAN code to analyze the structural behaviour of a helicopter skid landing gear during hard landing. Three impact conditions were simulated under different sink rates and the results were compared with test results. Authors demonstrated that the simulation results have good agreement with the corresponding dynamic drop tests. Williams and Bolukbasi [14] evaluated skid landing gear design at different landing conditions using KRASH program. In this study, the crosstubes were modeled as nonlinear springs. The study objectives were to limit

the strains in the crosstubes below the allowable material strains and to maintain a positive clearance between the fuselage and the ground plane. The dynamic response of the skid gear simulated in level impact was validated experimentally with two level drop tests. Very good correlation was found between the results of numerical simulation and the drop tests. Stephens and Evans [15] used general purpose FE software MSC/DYTRAN to obtain the structural behavior of skid landing gear of two helicopter models, UH-1Y and UH-1Z, at various landing conditions. The FE results were validated with the analytical methodology developed by Bell Helicopter Textron Inc. known as "CPS10P". The cross members of the gear have rectangular cross-section and were designed to meet the energy absorption requirements under six different landing conditions (level, level with drag, level with side load, one-skid landing, rolled attitude, and one-skid restricted). The FE software results correlated well with CPS10P dynamic drop results. Kim and Kim [16] also employed LS-DYNA software to conduct nonlinear transient impact analysis of a skid landing gear under different crash models. For two impact conditions (level and landing with a drag) the numerical results agreed well with experimental ones within 5% deviation. Élie-dit-Cosaque *et al*. [17] studied the impact of the manufacturing process of the metallic skid landing gears on their performance during drop test simulations. In their study, they took into account the history of the manufacturing of the crosstubes material. The approach was successfully implemented in ABAQUS/CAE software. The authors concluded that the bending process of the cross beam has appreciable effect on the level of stresses and strains during the drop tests. Thus, it has to be taken into consideration.

1.3.2 SLGs equipped with passive viscous EAs

The limited energy dissipation capability of the conventional skid landing gears prompted implementing supplemental devices such oleo-pneumatic shock absorbers to dissipate the tremendous amount of energy during impact. The intentions were to avoid destructing the fuselage in hard impacts and to maintain the abrupt acceleration within the human tolerance range. However, the passive viscous dampers were found unsuitable due to their lack of real-time adaptability to the impact environments because they are usually designed to accommodate acceleration loads at the condition of maximum gross weight and maximum design impact velocity. If, for example, the helicopter hits the ground at a velocity lower than the design velocity, then the occupants may experience accelerations higher than those when the helicopter equipped

with the conventional SLG. On contrary, if the helicopter impacts at a speed higher than the design value, then the damper suffers end-stop impact and high impact load would be transmitted to the occupants. In shock and impact mitigation applications, the damping coefficient can be optimized either to minimize the acceleration or to limit the payload travel or stroke [18]. The minimization of acceleration requires low stiffness of the hydraulic liquid so that the shock absorber can travel large displacements. However, this may result in end-stop impact. Constraining the piston travel to avoid end-stop impact, on the other hand, requires a stiffer damper which in turn may result in input acceleration higher than that the peak of undamped SLG system. Since the passive viscous damper cannot handle these requirements concurrently, adaptive energy dissipation devices are incorporated in the SLGs to provide the required protection to the occupants under varying environmental conditions.

1.3.3 SLGs equipped with smart MREAs

The evolution of high speed computers and the advances in the smart materials and control sciences have motivated employing adaptable dampers in the landing gear systems. Different configurations of the well-known electrorheological energy absorbers (EREAs) and magnetorheological energy absorbers (MREAs) have often been quoted in literature as the most successful adaptive energy absorbers to protect occupants during hard impact and crash events. The key advantages of MREA compared with their electrorheological counterparts are: Fast adjustment of the stroking load within the very short impact duration, low power consumption, wide temperature operating range from −40 to 150^{o} C with only slight variations in yield stress, less sensitivity to the contaminants and fail-safe features [19].

In this context, single and multi-coil conventional single-flow path MR dampers have been extensively studied, optimized and validated for use in landing gears under different impact load conditions. Batterbee *et al*. [20, 21] optimized and experimentally validated a single-flow path MR damper retrofitted from a passive damper. The study was conducted at a sink rate of 2.43 m/s using a drop mass of 473 kg. Hengbo *et al*. [22] proposed a new phenomenological model based on the Bouc-Wen model to predict the MR response under the influence of impact loads. The study showed that the estimated damping forces were in good agreement with the impact test results. Choi *et al*. [23] designed and drop tested a multi-coil single-flow mode MR damper for the use in a landing gear system of a helicopter. The proposed MR damper was developed based on Bingham

plastic model which accounts for minor loss factors, called BPM model. The system demonstrated its capability of attenuating the impact loads for a sink rate range of 1.83 to 3.65 m/s. Mao *et al*. [24, 25] designed and successfully drop tested a MREA at sink rate of up to 5 m/s. In their studies, BPM model predicted the off-state damping force more accurately than the basic BP model because the BPM model took into consideration the effect of non-linear velocity squared damping effect along with the minor losses. These minor losses are mainly due to both the change in the geometry profile and the type of flow inside the MR valve. Singh *et al*. [26] carried out an optimization study on a conventional MREA to maximize its dynamic range at impact velocity of up to 8 m/s. The study compares the device performance for 3, 4, and 5 coils. Using BPM model, the damper achieved dynamic range of 1.73 at impact velocity of 8 m/s when operated at a maximum current of 5.5 A.

1.3.3.1 SLGs equipped with bi-fold MR energy absorbers

The requirement of delivering large stroke load in a limited space prompted designing compact bi-fold MREAs. These devices can produce the required damping force and attain high dynamic range at high impact velocity without violating the volume constraints. Mao *et al*. [27-29] designed bi-fold MREAs, developed analytical models to predict their response, and experimentally validated these models under different impact velocities. In [27], a hydro-mechanical (HM) model was developed to account for fluid compressibility and inertia as well as the losses due to minor factors. The HM model was used to characterize the MREA under shock and impact loads for a piston velocity of up to 6.71 m/s. Based on this model, the MR damper was fabricated and tested using a drop test rig. The device performance was evaluated by dropping a mass of 45.5 kg on the damper's shaft at speeds 1, 2, and 3 m/s. The results showed that the HM model could accurately predict the behavior of the MREA device. In [28], the authors designed and fabricated a bi-fold flow-mode MREA. The device performance was assessed under high end velocity of 6.75 m/s for shock energy dissipation and at low velocity of 0.1 m/s for mitigating the residual vibration. To characterize the damper, two analytical models were adapted: The BP model to capture the response of the damper at high speed impact and the Bingham Plastic model coupled with low speed hysteresis (BPH) to account for the hysteretic characteristics of the MR damper at low velocity. Mao and co-authors [29] designed three MREAs based on the following three analytical models, Unsteady-BP, unsteady-BPM, and HM dynamic models. The performances of

the above MREA device were validated by conducting drop tests for a drop speed of up to 6.75 m/s. The comparison of the simulation and test results revealed that the developed HM model was more accurate than the other two models in the prediction of the response of the bi-fold MREA because it accounts for fluid compressibility in addition to the inertia of the MR fluid inside the MR gap.

One objective of the present research dissertation is to geometrically optimize a bi-fold MREA to maximize its dynamic range for an impact velocity of up to 5 m/s. Thus, maintaining good controllability of the MREA without violating the constraints.

1.4 Finite element modeling of helicopter for crashworthiness studies

The impact is highly nonlinear short-duration dynamic phenomenon. Therefore, the crashworthiness problems are usually solved using numerical techniques. The advent of powerful digital computers in the 1960s and the improvement in the computational mechanics have appreciably contributed to the development of finite element programs for use in crashworthiness analyses. In recent years, the use of the finite element based programs in the computation of the helicopter response has become a trend since they have been proven to be very efficient in reducing the cost and in avoiding the burden of the relatively prolonged time of the development and certification of aircrafts. As a consequence, a fewer number of tests may be conducted to validate the simulation results or study the effects of some poorly understood phenomena [30]. Several governmental agencies, institutions, and companies around the world have developed their transient dynamic drop simulation programs, either individually or jointly, to analyze the behavior of aircrafts and their subsystems during the course of landing or crash. ABAQUS/Explicit, DYNA-3D, LS-DYNA, and MSC/DYTRAN are examples of these programs. Some of these FE codes solve the non-linear impact problems using the explicit time integration method to maintain the numerical stability of the model, dramatically decrease the execution time, and provide the program with the required robustness [30]. In the following section, the explicit time integration method is briefly discussed.

1.4.1 Explicit time integration method

The numerical solution of the nonlinear short-duration dynamic response problems such as helicopter and vehicle crashes entails using the explicit scheme [30]. The method is very efficient

in solving problems that incur large dynamic load and deformation during very short time [31, 32]. The method solves the equation of motion of the system to obtain the approximate displacement of the node at the future time step, t+Δt, based on the previous time-history response of the accelerations, velocities, and displacements. This relation can be generally expressed as [31]

$$x(t+\Delta t) = f\{x(t), \dot{x}(t), \ddot{x}(t), x(t-\Delta t), \dot{x}(t-\Delta t), \ddot{x}(t-\Delta t), \dots\} \tag{1.3}$$

where Δt is the time step and $x(t), \dot{x}(t), \ddot{x}(t)$ are the nodal displacement, velocity, and acceleration vectors, respectively. In ABAQUS/Explicit, the central difference integration is the most commonly used rule to integrate the equation of motion of the system using the diagonal lumped mass matrix to reduce the computation burden. Using this method, the governing equation of motion may be written in the form as [32]:

$$[\mathrm{M}]\{\ddot{x}(\mathrm{t})\}^i + f^i\{x(\mathrm{t}), \dot{x}(t)\} = P^i\{x(t), t\} \tag{1.4}$$

where [M] is the diagonal mass matrix, $f\{\text{-}\}$ represent the internal force vector, $P\{\text{-}\}$ is the external force vector, and i is the increment counter. Rearranging expression (1.4) yields

$$\{\ddot{x}(\mathrm{t})\}^i = [\mathrm{M}]^{-1}(\{P\}^i - \{f\}^i) \tag{1.5}$$

Equation (1.5) solves the nodal accelerations with no iterations at the beginning of every time increment. Using the known nodal values of acceleration at time t, the explicitly updated nodal velocity at the next time step $t + \frac{\Delta t}{2}$ and the displacement at time step $t + \Delta t$ can be calculated respectively as [32]

$$\{\dot{x}(t)\}^{i+\frac{1}{2}} = \{\dot{x}(t)\}^{i-\frac{1}{2}} + \frac{\Delta t^{i+1} + \Delta t^i}{2}\{\ddot{x}(\mathrm{t})\}^i \tag{1.6}$$

$$\{x(t)\}^{i+1} = \{x(t)\}^i + \Delta t^{i+1}\{\dot{x}(t)\}^{i+\frac{1}{2}} \tag{1.7}$$

The calculation of velocity and displacement require that the initial velocity, $\{\dot{x}(t)\}^{i-\frac{1}{2}}$, be given. $i-\frac{1}{2}$ and $i+\frac{1}{2}$ are the mid-increment values of the constitutive time steps before and after the current time increment. For the solution to be stable, it is necessary to have the time step, Δt, less than that required for the stress wave to traverse the smallest element dimension in the model [30,

31]. Therefore, the explicit central difference solution is conditionally stable [33]. The speed of the elastic wave can be computed as

$$c_w = \sqrt{\frac{E}{\rho}} \tag{1.8}$$

here E is the modulus of elasticity of the material and ρ is the material density. Assuming that the shortest element dimension is L_{min}, the approximate time step is given as [32]

$$\Delta t \approx \frac{L_{min}}{c_w} \tag{1.9}$$

From Eq. (1.9) it is apparent that a large number of time steps is required to solve the crash problem implementing the explicit technique.

1.4.2 Validation of the FE model response in the absence of experimental results

The results of impact simulation can be validated by using the energy balance principle to ensure that the system yields the correct response. This principle applies assuming no loss of energy in the system. The principle states that the total energy of the model should remain approximately constant during the simulation. Therefore, any unrealistic growth in any energy component will be reflected in the total energy equation. The equation of the total energy of the system can be written as [32, 34]

$$\mathrm{E_{TOT}} = \mathrm{T} + \mathrm{U} + \mathrm{E_{VD}} + \mathrm{E_{FD}} - \mathrm{E_W} = \mathrm{Constant} \tag{1.10}$$

where

$\mathrm{E_{TOT}}$: Total energy of the system,

T : Kinetic energy,

U : Internal energy,

$\mathrm{E_{VD}}$: Viscous dissipation energy,

$\mathrm{E_{FD}}$: Frictional dissipation energy, and

$\mathrm{E_W}$: Work of external forces.

The alternative validation method, in the absence of experimental data, is to compare the maximum acceleration of the fundamental pulse, which is computed by the program, with the

maximum slope of the velocity during the SLG springback [35]. If these values are found approximately the same, then the simulation results are acceptable.

1.5 Motivation and objectives

The reviewed work on the design and numerical analysis of the skid landing gear has revealed that provision of protection to the occupants in the event of hard landing or crash is of paramount significance to the helicopter community. Due to the limited energy dissipation capabilities of the conventional SLG design and impracticality of incorporating passive viscous dampers, this research mainly aims at utilizing the adaptive energy absorption devices to enhance energy absorption capacity of the skid landing gear system. The magnetorheological energy absorber tends to be the most suitable device to accomplish this task. Furthermore, taking space constraint into account, the pertinent conventional multi-coil single-flow path MR damper was found not convenient because it accommodates large volume and may not fit in the designated space between the crosstube and the fuselage. The novelties of the present dissertation are mainly to introduce a bi-fold MREA in the skid landing gear, to establish a new relationship governs the generation of the desired damping force based on the optimum Bingham numbers and the rotor lift factor, and reducing the hassle of conducting numerous drop tests by introducing new design charts in which the required effective mass and the displacement can be rapidly estimated based on the anticipated velocity of impact. These charts have been developed by carrying out a series of simulations using ABAQUS/Explicit software. To fulfill the above goal, the following objectives have been identified:

- Determine the dynamic response of the conventional SLG system under various impact velocities using ABAQUS/Explicit software. The computed response results shall then be used as a reference benchmark for the subsequent phases of the research work.
- Develop a practical design optimization strategy to optimize the size of the baseline SLG in order to maximize its specific energy absorption (SEA) capacity under weight, displacement, load factor, and size constraints.
- Perform a design optimization study on a bi-fold MREA to maximize its dynamic range, minimize the field-off damping force, and to ensure that the device fits in the designated space.

- Integrate the optimized bi-fold MREA with the baseline and geometrically optimized skid landing gear systems and assess the systems' performances through development of an equivalent single degree of freedom model. The system performance is evaluated in terms of the non-dimensional displacement, velocity, acceleration. In the meanwhile, new relationships between the Bingham numbers for the compression and rebound strokes and the rotor lift factor are proposed for a range of sink rates.
- Formulate a suitable semi-active control strategy to provide the required input control current for generating the desired damping force based on the anticipated impact velocity and the rotor lift factor.

1.6 Thesis organization

To accomplish the objectives of the present research, this dissertation has been organized into seven chapters:

Chapter one covers a short introduction on the topics related to human body tolerance to the abrupt acceleration, the crashworthy systems of helicopters, the regulations for testing and certifying the skid landing gears of helicopter, the types of energy absorption systems that can be incorporated with the skid gears, and some aspects of finite element method related to the dynamical analysis and model validation. The motivations, objectives, and thesis organization are summarized at the end of the chapter.

Chapter two deals with the analysis of the adopted skid landing gear to establish a reference for further improvements in term of increasing the energy absorption capabilities. In this context, governing charts that relate the required effective mass and the length of stroke "deflection" with the sink rate are introduced for the first time based on drop test simulation results.

Chapter three presents the methodology of optimizing the size of the crosstubes to improve the energy absorption capacity of the conventional skid landing configuration. The technique, which is based on the statistical methods, avoids the drawback of using the commercial optimization codes and while its results are excellently correlated to the simulation results. In this study, the optimized SLG is assessed in terms of the specific energy absorption, load factor, displacement, and mass when compared to the baseline design.

Chapter four demonstrates the feasibility of the bi-fold energy absorbers for the use with the skid landing gears to increase the systems' energy absorption capabilities at high sink rates. An optimization study is carried out to increase the dynamic range while respecting the constraints on the external volume of the device in order to fit into the allocated space.

In Chapter five, equivalent single degree of freedom analysis is carried out on the helicopter model incorporating three SLG configurations, zero damped, passively damped energy absorber (EA), and magnetorheological (MREA) systems. The objective is to compare the dynamic responses of these systems and to demonstrate the advantages of equipping the conventional SLG with the adaptive MREA over the passive EA. In this chapter, new design charts that are used to determine the optimum Bingham numbers in terms of the varied rotor lift factor are introduced.

To entail the adaptability of the SLG, Chapter six presents the closed feedback semi-active control strategy. The developed strategy is based on varying the generated damping force at different sink rates according to the change in the corresponding Bingham numbers in compression and rebound stroke.

Chapter seven concludes the outcomes of the research comprehensively and provides a list of contributions of the thesis. It finally outlines the proposed future work.

CHAPTER 2

Crashworthiness Analysis of a Conventional Skid Landing Gear

2.1 Introduction

This chapter concerns the nonlinear dynamic analysis of a realistic skid landing gear of a lightweight helicopter. The displacement of the helicopter's center of gravity is first predicted using theoretical analysis and then refined by simulating drop tests in ABAQUS/Explicit. The refined magnitude of the vertical displacement is then utilized to calculate the effective helicopter mass at the C.G. to replicate the effect of the activation of the rotor lift force at the instant of contact between the skids and the ground. To facilitate the selection of the right effective mass based on the deflection and velocity constraints and to eliminate the computation burden associated with FE analysis, new design charts are introduced based on the governing parameters of the drop test simulation, i.e. sink rate, maximum permissible deflection, and the corresponding effective mass for rotor lift factors of 0.67 and 1.0. These charts not only can be used for mimicking the impact scenarios numerically, but can also be used for setting up the experimental drop tests.

The dynamic response of the helicopter model is numerically computed according to the AWM chapter 527 and FAR Part 27 crashworthiness regulations for certifying the SLG of civilian helicopter. Two drop tests are performed: Limit load and reserve energy certification drop tests. Fortunately, the conventional SLG could meet the specifications' requirements in absorbing enormous amount of energy and minimizing the acceleration experienced by helicopter occupants. However, this objective is achieved at the expense of permanent deflection of the crosstubes and rendered the SLG malfunctioned.

2.2 The geometry and material properties of the baseline SLG

The configuration of the baseline SLG is adopted from Ref. [10] and is shown in Figure 2.1. The SLG is composed of two crosstubes of hollow circular cross section and is rigidly mounted to the fuselage with two rigid attachments per crosstube. Two skids are connected to the either end of the crosstubes to provide stability and ease of ground handling. The mass properties of the helicopter and dimensions of the SLG components and it's the elastic properties are provided in Tables 2.1 and 2.2, respectively. Due to the lack of details on material characteristics of the landing gear, aluminum alloy Al 7075-T6 has been considered since it is commonly used in conventional

skid gears in view of its high strength and lightweight. Tables 2.2 and 2.3 provide data extracted from the plastic stress-strain curve of this material [36].

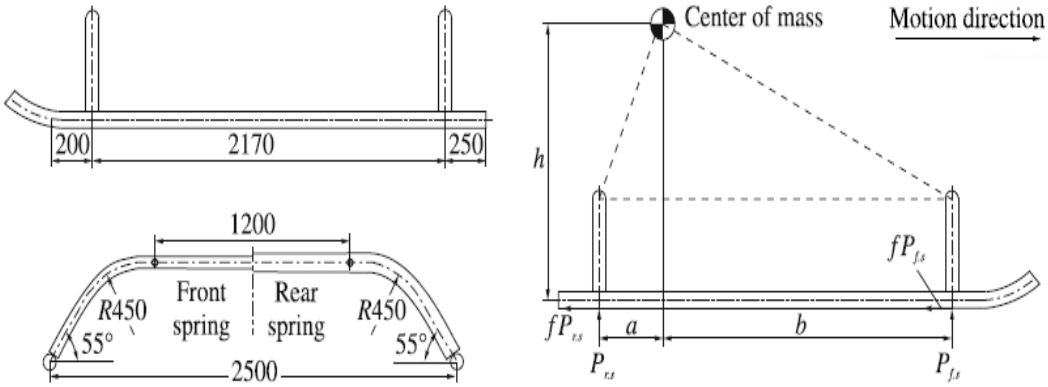

Fig. 2.1. Skid landing gear geometry [10].

Table 2.1. Mass properties of the helicopter [10].

Helicopter gross weight	2260 kg
Density of alloy 7075-T6	2810 kg/m^3
Ixx about C.G.	3271 kg.m^2
Iyy about C.G.	10231 kg.m^2
Izz about C.G.	11655 kg.m^2

Table 2.2. Dimensions and elastic properties of the baseline SLG [10], [36].

Front crosstube cross sectional dimensions	Ø 65×2.5 mm
Aft crosstube cross sectional dimensions	Ø 80×2.5 mm
Skid tube cross sectional dimensions	Ø 75×2.0 mm
h	1602.0 mm
a	483.0 mm
b	1687.0 mm
Modulus of elasticity (E)	72 GPa
Yield stress (σ_y)	533 MPa
Rupture stress (σ_r)	658 MPa
Poisson's ratio (μ)	0.3

Table 2.3. Plastic stress-strain data [36].

Logarithmic true strain	Yield stress, MPa
0	533.0
0.0114	576.15
0.0180	603.08
0.0314	613.85
0.0431	630.0
0.0514	640.77
0.0616	651.54
0.0714	658.0

2.3 Effective mass of the helicopter

In practical situations, the pilot activates the rotor lift at the instant of contact between the skids and the ground in the course of landing. This minimizes the amount of energy to be absorbed by cross-tubes and extends tubes life. In order to certify the SLG system, civil and military crashworthiness regulations [6, 7, 9, 37] mandate that the mass, the inertial characteristics of the helicopter as well as the rotor lift force be represented during the drop test. To calculate the effective mass of the helicopter and to determine the dynamic response of helicopters that incorporate conventional SLGs, the following assumptions are considered:

1- Level vertical impact with no forward velocity [7, 9].
2- Negligible rotatory energy due to helicopter pitching in level landing attitude which means that the vertical displacement is the only relevant parameter [11].
3- The stiffness of the SLG is the same for static and dynamic loading [11].
4- The impact surface (ground) is flat and rigid.
5- The conservation of energy law is assumed valid and the entire impact energy is absorbed by the crosstubes in bending.
6- Frictionless contact is assumed between the skids and the ground.
7- Negligible structural damping.
8- The rotorcraft drops freely under the influence of earth's gravity with negligible air resistance.
9- Lift force generated by the main rotor is activated at the instant of contact between the skids and ground and the line of action of the force passes through the C.G.

2.3.1 Calculation of the effective mass and helicopter dynamic response

In the present research, the method of calculating the effective mass is summarized in the following steps:

1- Model the SLG in ABAQUS with the geometrical and material properties provided in Tables 2.1-2.3 and apply a downward concentrated force at the helicopter C.G.
2- Run static analysis in ABAQUS standard solver to calculate the resultant reaction force and displacement at the center of gravity.
3- Draw force-deflection curve to calculate the stiffness of the conventional SLG by approximating the curve to a bi-linear piecewise elastic-inelastic segments [11].
4- Estimate the displacement (δ) of the structure analytically under the given sink rate and rotor lift factor by substituting the values for the elastic and inelastic stiffness in the related governing equations.
5- Evaluate the effective mass of the helicopter (m_e) using the known values of the helicopter gross mass, C.G. deflection (δ), and *L,*
6- Lump the effective mass at the helicopter C.G. and run the analysis using ABAQUS/Explicit solver to compute the displacement response.
7- Compare the analytically calculated displacement in point 5 with that evaluated numerically in Step 7. If the error margin is unsatisfactorily large, then recalculate the effective mass (step 6) using the displacement computed in step 7.
8- Repeat the process until the error in displacement between two consecutive iterations is reduced to the desired margin.
9- Then, use ABAQUS/Explicit to compute the dynamic responses such as the velocity and the acceleration and related energies.

In real helicopter landing, the activation of the rotor lift at touchdown reduces the deflection and the bending stresses in the crosstubes. Thus, avoid collapsing the SLG and prolonging its life. In this case, the amount of potential impact energy imparted to the landing gear is reduced by ratio equal to (L). The range of L can be set between zero and one. Zero means no rotor lift force is activated and one means that the activated rotor lift force is equal to the helicopter weight, as depicted in Eq. (1.1). Nevertheless, in drop test simulations and field test of the preliminary design

of the SLG it is very costly and impractical to incorporate an engine to generate the desired rotor lift force at the instant of contact. Therefore, the idea of calculating the equivalent mass has been found very practical because it accounts for the contribution of the rotor lift force along with the helicopter weight in achieving the same deflection and producing the same amount of impact energy during the realistic impact event, as expressed by L [11, 38]. For instance, at L = 0.67, 67% of the helicopter weight is counterbalanced by the lift force and hence only one third of potential energy is added, whereas at L = 1.0, the entire weight is counterbalanced. In the later case, the impact energy is the kinetic energy only. In impact simulations and experimental drop tests, it is conventional to assume that the helicopter mass deflects by amount (δ) after touchdown of the freely dropped helicopter with reduced mass (effective mass) after touchdown is the same as that of the air-borne helicopter mass with rotor lift activated at contact with the ground. The effective mass can be evaluated by equating the energies of the freely dropped and the air-borne helicopter at the touchdown [38]. The procedure is described below:

The impact energy of the air-borne helicopter with activated lift at the touch down is calculated as

$$E_{air-borne} = \frac{1}{2} m v_0^2 + mg\delta(1 - L) \tag{2.1}$$

The impact energy of the effective (reduced) mass in the drop test can be determined by

$$E_{drop\ test} = \frac{1}{2} m_e v_0^2 + m_e g\delta \tag{2.2}$$

Now, by equating equations (2.1) and (2.2) the effective mass is calculated as

$$m_e = m[\frac{v_0^2 + 2(1 - L)g\delta}{v_0^2 + 2g\delta}] \tag{2.3}$$

The substitution of the free fall velocity $v_0 = \sqrt{2gh}$ in Eq. (2.3) yields

$$m_e = m\left[\frac{h + (1 - L)\delta}{h + \delta}\right] \tag{2.4}$$

2.3.2 Determination of the skid landing gear deflection

In this section, two methods will be used to predict the deflection of the Helicopter C.G. The first method is purely theoretical based on linearization of the force-displacement curve using

approximate bilinear piecewise curves for the elastic and inelastic regions as explained in Ref. [11]. The second method is a numerical method which utilizes the general purpose finite element software ABAQUS. The calculated deflection of the helicopter C.G. is then used to determine the effective mass as described in Section 2.3.1.

2.3.2.1 Bilinear piecewise approximation

Considering the schematic piecewise force-deflection curve in Figure 2.2, the energy absorbed by the bending of the crosstubes is derived as per Ref. [11]. Let K_e denote the piecewise elastic stiffness of the SLG. Then, the elastic energy absorbed by the SLG can be expressed as

$$E_{b_e} = \frac{1}{2} K_e \delta^2 \ , \qquad \delta \leq \delta_y \tag{2.5}$$

If the impact velocity is low enough so that no plastic deformation is incurred in the crosstubes, i.e. $\delta \leq \delta_y$, the displacement is determined by equating expressions (2.1) and (2.5) so that

$$\frac{1}{2} K_e \delta^2 = \frac{1}{2} m v_0^2 + mg\delta(1 - L) \tag{2.6}$$

By rearranging Eq. (2.6) and solving it for δ we obtain

$$\delta = 2\{ (1 - L)\frac{mg}{K_e} + \sqrt{[(1 - L)\frac{mg}{K_e}]^2 + \frac{mv_0^2}{K_e}} \}, \ \delta \leq \delta_y \tag{2.7}$$

The maximum sink rate that makes the helicopter attaining the prescribed yield deflection can be computed from Eq. (2.6) as

$$v_0 = \sqrt{\frac{K_e}{m}[\ \delta_y^2 - 2(1 - L)\frac{mg\delta_y}{K_e}\ ]} \tag{2.8}$$

At the yield point Eq. (2.5) can also be expressed as

$$E_{b_{e,y}} = \frac{1}{2} F_y \delta_y = \frac{1}{2} K_e \delta_y^2 \tag{2.9}$$

Let us now assume that the sink rate is high enough to incur plastic deformation in the crosstubes. In this case, the displacement of the rotorcraft C.G. can also be estimated using similar procedure. By defining the inelastic stiffness as K_i, the energy dissipated by the SLG in the plastic zone can be calculated from as [11]

$$E_{b_i} = \frac{1}{2}\left(F + F_y\right)\left(\delta - \delta_y\right) \tag{2.10}$$

Expressing the yield and plastic forces in terms of elastic and plastic stiffness gives

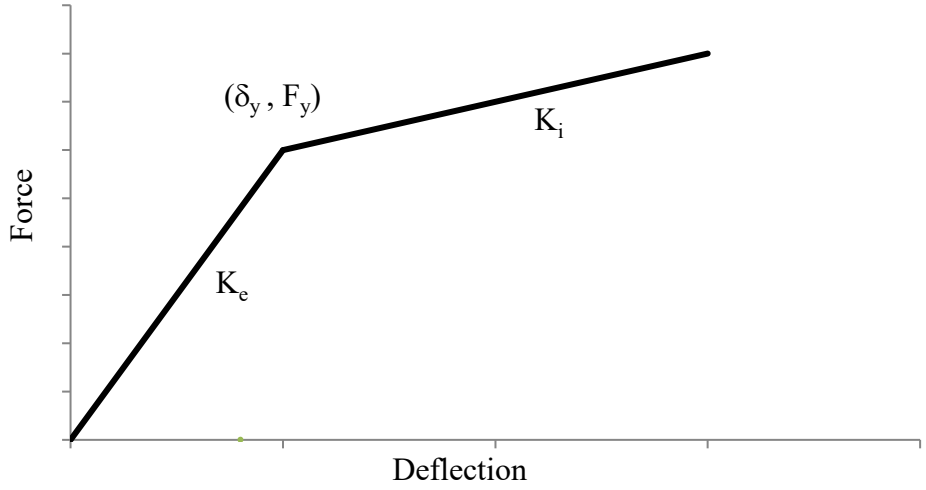

Fig. 2.2. Bi-linear force-deflection curve.

$$E_{b_i} = \left[\frac{1}{2}K_i\left(\delta - \delta_y\right) + K_e\delta_y\right]\left(\delta - \delta_y\right) \tag{2.11}$$

Eq. (2.11) can be rearranged to

$$E_{b_i} = \frac{1}{2}K_i\left(\delta^2 + \delta_y^2\right) + (K_e - K_i)\delta_y\delta - K_e\delta_y^2 \tag{2.12}$$

The total bending energy absorbed by the crosstubes which are subjected to plastic deformation is the summation of elastic (reversible) and plastic (irreversible) energies and can be computed as

$$E_b = E_{b_{e,y}} + E_{b_i} = \frac{1}{2}F_y\,\delta_y + \frac{1}{2}\left(F + F_y\right)\left(\delta - \delta_y\right) \tag{2.13}$$

Substituting expressions (2.9) and (2.12) into (2.13) yields

$$E_b = \frac{1}{2} K_i \delta^2 + (K_e - K_i)\delta_y \delta - \frac{1}{2}(K_e - K_i)\delta_y^2 \quad (2.14)$$

Since no loss of energy is assumed, the displacement of the helicopter C.G. can now be found by equating expressions (2.1) and (2.14). Solving for δ yields

$$\delta = (1 - \bar{K})\,\delta_y + (1 - L)\frac{mg}{K_i} + \sqrt{[(\bar{K} - 1)\delta_y - (1 - L)\frac{mg}{K_i}]^2 + (\bar{K} - 1)\delta_y^2 + \frac{mv_0^2}{K_i}} \quad ,$$

$$\delta > \delta_y \quad (2.15)$$

here $\bar{K}$ $\left(\bar{K} = \frac{K_e}{K_i}\right)$ is the ratio of elastic to the inelastic stiffness of the idealized elasto-plastic piecewise curve shown in Figure 2.2. For *L*=1, equation (2.15) is reduced to

$$\delta = (1 - \bar{K})\,\delta_y + \sqrt{\bar{K}(\bar{K} - 1)\delta_y^2 + \frac{mv_0^2}{K_i}} \quad (2.16)$$

By constraining the displacement to a specific value based on the clearance between the fuselage sub-structure and the ground, the impact velocity can be calculated from Eq. (2.15) as

$$v_0 = \sqrt{\frac{K_i\delta^2 + 2\delta\left[(K_e - K_i)\delta_y - mg(1 - L)\right] - (K_e - K_i)\delta_y^2}{m}} \quad (2.17)$$

2.4 Simulation of helicopter crash using ABAQUS/Explicit

In this section, the dynamic responses and energies evaluated numerically using ABAQUES software will be presented and discussed. The objective is to determine the amount of the energy that can be absorbed by the baseline configuration without sustaining damage. In addition, displacement, velocity, acceleration as well as the impact force will be computed and will be later used as a reference for the sake of compassion with different configurations of the SLG system.

2.5 Finite element model of skid landing gear

ABAQUS software is a powerful FE software tool for simulation of the highly nonlinear and short-duration dynamic phenomena such as in impact analysis. In the current study, the explicit dynamic analysis is carried out to determine the dynamic response of the skid landing gear as per the requirements of the crashworthiness regulations. The mass of the helicopter structure other than the SLG is lumped at the helicopter C.G. The mass moments of inertia (I_{xx}, I_{yy}, I_{zz}) are applied about the three global axes x, y, z which pass through the C.G., respectively. Four rigid elements are used to connect the crossbeams to the helicopter C.G., as shown in Figure 1.1. To reduce the cost of the computation, the landing surface is modeled as a fully constrained two dimensional rigid surface [39]. The rigid surface is associated with a single reference point where the degrees of freedom are applied. These degrees of freedom become only active when the contact interaction between the SLG and the surface is considered. The rigid surface does not contribute to the rigid body mass or inertia properties of the helicopter. To simulate the free falling of the helicopter, a gravity acceleration of 1g is imposed on the model in the downward direction. The energy absorption capability of the SLG is assessed by assuming a frictionless contact between the gear and the ground, yet no penetration is permitted. The FE model of the aircraft is generated in ABAQUS preprocessor. To reduce the computation burden, the skid landing gear is modeled using explicit space beam elements (B31) with linear geometric order [12]. The skid landing gear is modeled using a total number of 452 nodes and 156 elements. The duration of simulation time was set at 1.2 seconds to ensure capturing the response of the model over a relatively prolonged period and to accommodate various impacts at sink rates as well.

2.6 Results and discussion

Defining frictionless contact between the gear and the ground is a very conservative approach because the entire impact energy, in this case, is absorbed by the crosstubes based on the assumptions made earlier. Thus, the performance of the conventional baseline SLG system can be evaluated and used as a reference for the subsequent analyses.

2.6.1 Chart of the drop test governing parameters

The static analysis of the helicopter provides the force-deflection diagram shown in Figure 2.3. The curve is idealized to piecewise linear elastic and inelastic segments. By knowing the elastic and inelastic stiffness, the displacement of the helicopter C.G. can now be calculated analytically

using Eqs. (2.7) and (2.15). By substituting the value of the displacement and the height from which the helicopter is released into Eq. (2.4), the effective mass is estimated and then used in the finite element model as a concentrated mass at the helicopter C.G. To verify the method of calculation of effective mass introduced in section 2.3.1, drop tests of helicopter with three different masses 1000, 1500, and 2000 kg, two drop velocities 3 and 4 m/s, and two rotor lift factors 0.67 and 1.0 are simulated. The displacement results obtained from the analytical and nonlinear dynamic simulation are tabulated and compared in Table 2.4. Examination of results reveals that the difference between the analytical and finite element displacement (ABAQUS-1) is relatively high and could reach up to 13% in some cases. The difference is attributed to the approximation of the non-linear force-displacement curve to the bi-linear force-displacement curve. Using curve fitting, the non-linear equation of force in terms of deflection can be written as

$$F = 934372 \times \delta^3 - 935237 \times \delta^2 + 318616 \times \delta \qquad (2.18)$$

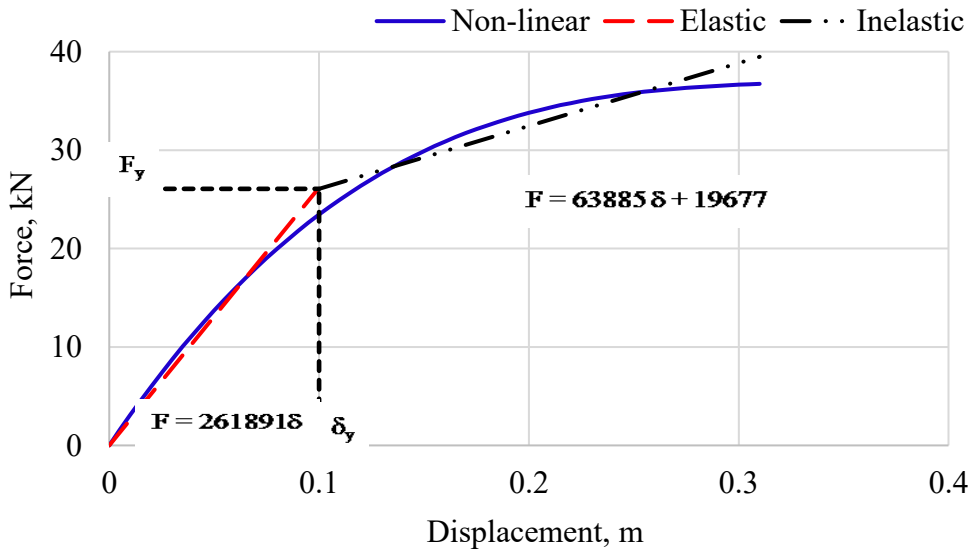

Fig. 2.3. Bi-linear force-displacement curve of baseline SLG.

To attain more accurate representation of the equivalent mass, the equivalent mass is adjusted based on the procedure mentioned in section 2.3.1. The displacement obtained by ABAQUS is substituted back into Eq. (2.4) to identify the updated effective mass. The finite analysis (ABAQUS-2) is conducted using the updated effective mass. The comparison of the displacements which are resulted from two runs conducted in ABAQUS is presented in Table 2.5. The

comparison shows that the error margin is substantially reduced to a maximum of 3.9% down from 13%. By using the tuned displacement, the effective mass is recalculated using Eq. (2.4).

Table 2.4. Comparison of displacement calculated analytically and by ABAQUS.

v_0 (m/s)	m (kg)	L	δ (mm) -Analytical	δ(mm) -ABAQUS-1	Error, %
3.0	1000	0.67	229.70	206.59	10.06
3.0	1500	0.67	311.08	283.41	8.89
3.0	2000	0.67	388.28	369.82	4.76
3.0	1000	1.0	207.68	187.39	9.77
3.0	1500	1.0	271.76	244.81	9.92
3.0	2000	1.0	329.44	302.62	8.14
4.0	1000	0.67	331.21	316.30	4.50
4.0	1500	0.67	445.33	447.06	0.39
4.0	2000	0.67	549.96	478.28	13.03
4.0	1000	1.0	304.48	287.59	5.55
4.0	1500	1.0	399.10	396.59	0.63
4.0	2000	1.0	482.50	465.31	3.56

The above combined theoretical-numerical procedure to estimate the effective mass and displacement has been repeated for impact velocities ranging from 1 to 5 m/s for both lift factors of L = 0.67 and 1.0 and the results are shown in Figures 2.4 and 2.5. It is worth noting that the design curves in Figures 2.4 and 2.5 are produced for the present helicopter model based on the given SLG geometry and material characteristics and on the defined mass properties. The Figures enable quick determination of the required effective mass to attain the desired deflection at a specific sink rate in either numerically simulated or experimentally conducted drop tests bearing in mind that complete damage of the SLG should be avoided. By utilizing these curves, limited number of experimental drop tests are required to validate the numerical models. Thus, the test setup time and cost are substantially reduced. For the present helicopter, the feasible area of the drop testing parameters, i.e. velocity, effective mass, and allowable displacement, is the upper left box which is bounded by horizontal and vertical dashed lines. In these charts, the maximum allowed displacement is restricted to 350 mm. Figures 2.4 and 2.5 demonstrate that the effective mass is considerably reduced with the increase in the rotor lift force because increasing L reduces the potential energy of the system. To use the proper formula in the calculation of the theoretical deflection, the threshold impact velocity is determined first using expression (2.8). If the impact velocity is less than the threshold, then Eq. (2.7) is used, otherwise Eq. (2.15) is the correct formula. The threshold velocity can be identified as the velocity corresponding to the yielding of the

crosstubes, by substituting $\delta = \delta_y$ in (2.8), the threshold velocities are found to be 0.91 and 1.076 m/s for limit load and reserve energy drop tests, respectively.

Table 2.5. Displacement response with tuned effective mass.

v_0 (m/s)	m (kg)	L	δ (mm) (ABAQUS-1)	$\delta(mm)$ (ABAQUS-2)	Error, %	m_e (kg)
3.0	1000	0.67	206.59	210.0	1.64	789.6
3.0	1500	0.67	283.41	289.34	2.09	1111.3
3.0	2000	0.67	369.82	375.20	1.46	1397.1
3.0	1000	1.0	187.39	192.14	2.53	704.8
3.0	1500	1.0	244.81	253.65	3.61	966.0
3.0	2000	1.0	302.62	314.29	3.86	1186.8
4.0	1000	0.67	316.30	318.75	0.77	811.7
4.0	1500	0.67	447.06	446.86	0.04	1144.2
4.0	2000	0.67	478.28	480.37	0.44	1505.0
4.0	1000	1.0	287.59	291.48	1.35	736.7
4.0	1500	1.0	396.59	397.47	0.22	1009.2
4.0	2000	1.0	465.31	467.14	0.39	1271.6

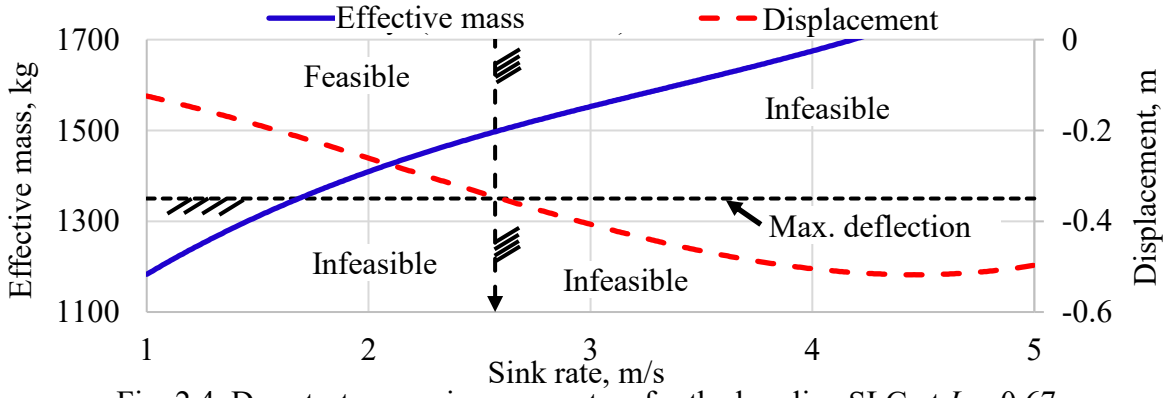

Fig. 2.4. Drop test governing parameters for the baseline SLG at L = 0.67

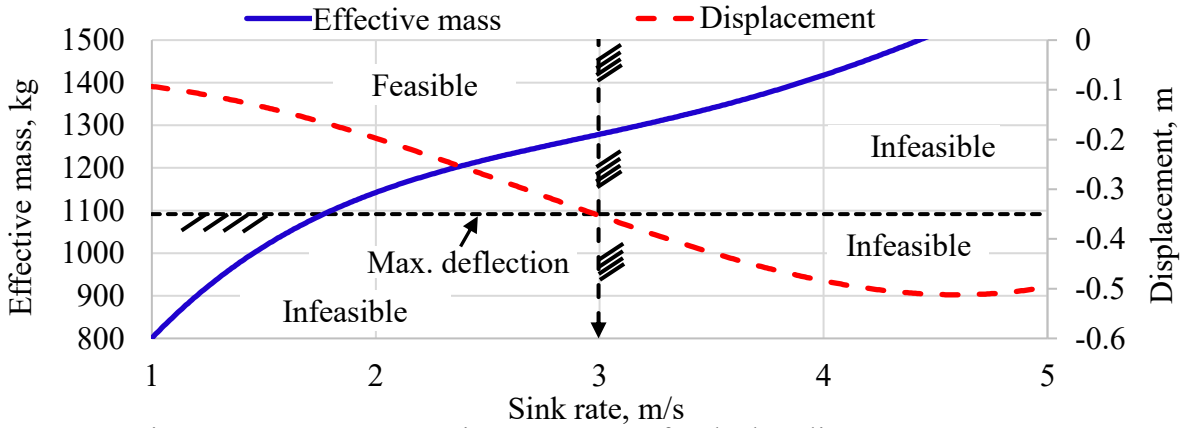

Fig. 2.5. Drop test governing parameters for the baseline SLG at L = 1.0.

2.6.2 Dynamic response of the helicopter

To ensure that the skid landing gear meets the requirements of the crashworthiness regulations AWM chapter 527 and FAR part 27 [6], two impact scenarios were simulated, limit load and reserve energy drop tests. The maximum deflection of helicopter C.G. is limited to 350 mm to avoid damaging the crosstubes severely. Tables 2.6 tabulates the parameters utilized in the simulation. These parameters are obtained from Figures 2.4 and 2.5.

Table 2.6. Impact parameters for limit load and reserve energy drop tests.

Drop test type	Max. permissible displacement (δ_{max})	Rotor lift factor (L)	Test sink rate (v_0)	Effective mass (m_e)
Limit load	250.0 mm	0.67	2.0 m/s	1427.0 kg
Reserve energy	262.0 mm	1.0	2.44 m/s	1220.0 kg

The displacement, velocity, and acceleration responses of the rotorcraft are compared in Figures 2.6-2.8 for the two drop tests. Axes zeros represent the reference time and position at the start of the free fall. The helicopter is released and fall freely from heights 203.9 and 303.5 mm under the influence of gravity to attain the desired sink rates for limit load and reserve energy drop tests, respectively. The gravitational effect dominates the fall until the skids hit the ground at instants 0.20387 and 0.24873 seconds for limit load and reserve energy drops. During the impact stroke, the crossbeams bend to absorb impact energy. In the limit load drop test, the helicopter C.G. attains maximum vertical deflection of $\delta_{max,0.67}$ = 248.5 mm, whereas in the reserve energy test the maximum attained deflection is $\delta_{max,1.0}$ = 257 mm, as depicted in Figure 2.6. These values deviate by 0.6% and 1.9% from the corresponding displacements in Table 2.6. The differences between the estimated displacements in Figures 2.4 and 2.5 and those computed by ABAQUS in Fig. 2.6 are very small confirming the feasibility of using graphs 2.4 and 2.5 to estimate the displacement and the required effective mass of the helicopter. Upon completion of first rebound stroke, residual deflections of 37.3 and 8.5 mm for the limit load and reserve energy drop tests are denoted, respectively. The residual deflections at the end of the second cycles increased to 105 mm for limit load drop test and 90 mm for reserve energy drop test as shown in Figure 2.6.

Figure 2.7 illustrates the velocity time history of the rotorcraft for the two impact scenarios. As the rotorcraft is freely falling down from rest it accelerates linearly under the effect of gravity until hitting the impact surface. When the impact stroke concludes, the system reaches its first

instantaneous rest position. At this position, the helicopter settles momentarily for a very short duration before springing back. From the figure, it is observed that the helicopter recovers adequate velocity in the rebound stroke (about 60%) to depart the ground for short distance before striking back.

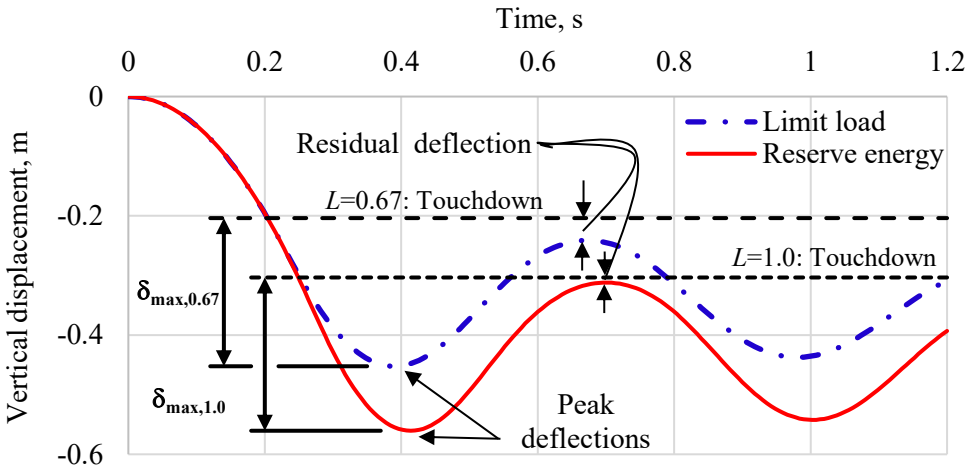

Fig. 2.6. Time history of helicopter C.G. displacement.

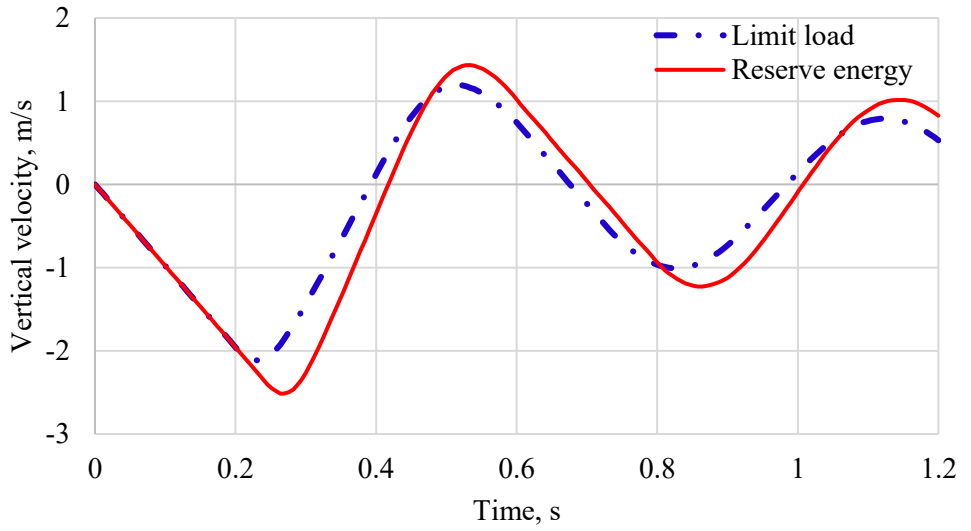

Fig. 2.7. Time history of helicopter C.G. velocity.

The acceleration response is extremely noisy and contains all the high frequency and low frequency (fundamental) components of the signal. The high frequency component is usually suppressed by the structure. To extract the correct shape and the amplitude of the low acceleration pulse, the noisy response is filtered using ABAQUS internal low pass Butterworth filter of 2nd

degree. The cut-off frequency is set by ABAQUS as one-third of the sampling frequency. For the used sampling interval of 0.00444 seconds, the cut-off frequency is calculated by the code as 75 Hz for both drop tests. Figure 2.8 shows both raw and filtered acceleration data for the reserve energy drop test. The coarse ripples in the filtered curve, especially in the acceleration curve of the reserve energy drop test, are due the slight inward-outward movement of the skids.

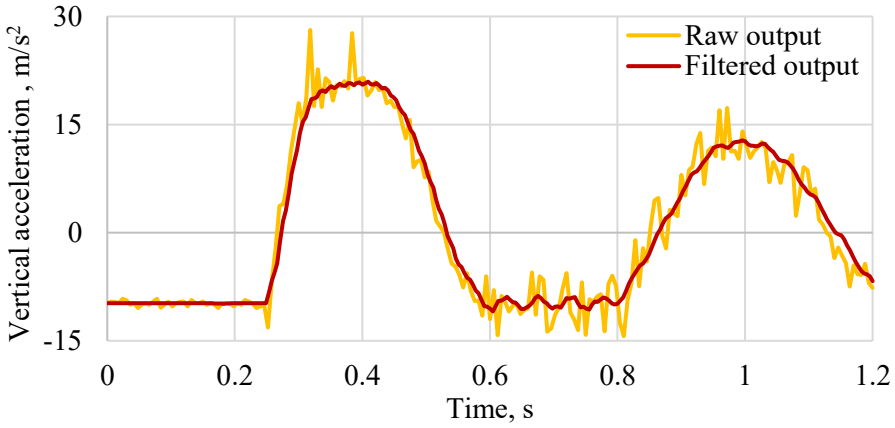

Fig. 2.8. Aliased and anti-aliased vertical acceleration response for reserve energy drop test.

Figure 2.9 shows the acceleration response of the limit load and reserve energy drop test versus the impact time where the increase in the peak acceleration in the reserve energy test is due to the high impact energy of the helicopter. To validate the finite element results based on method presented in section 1.4.2, the slopes of the velocity in Figure 2.7 (maximum acceleration) in the springback stroke are calculated as

$$For\ L = 0.67: \quad A_{y_{0.67}} = \frac{0.81 - (-1.77)}{0.456 - 0.276} = 14.3\ {}^{m}/_{s^2}$$

$$For\ L = 1.0: \quad A_{y_{1.0}} = \frac{0.709 - (-2.253)}{0.450 - 0.300} = 19.75\ {}^{m}/_{s^2}$$

The above peak acceleration magnitudes are pretty close to peak acceleration values obtained directly from ABAQUS as shown in Figure 2.9. In this Figure, the peak accelerations are computed as $A_{y_{0.67}} = 15.85$ and $A_{y_{1.0}} = 20.5$ m/s^2 with reasonable errors of 9.8% and 3.7% between the simulation and the theoretical values for limit load and reserve energy drop tests, respectively.

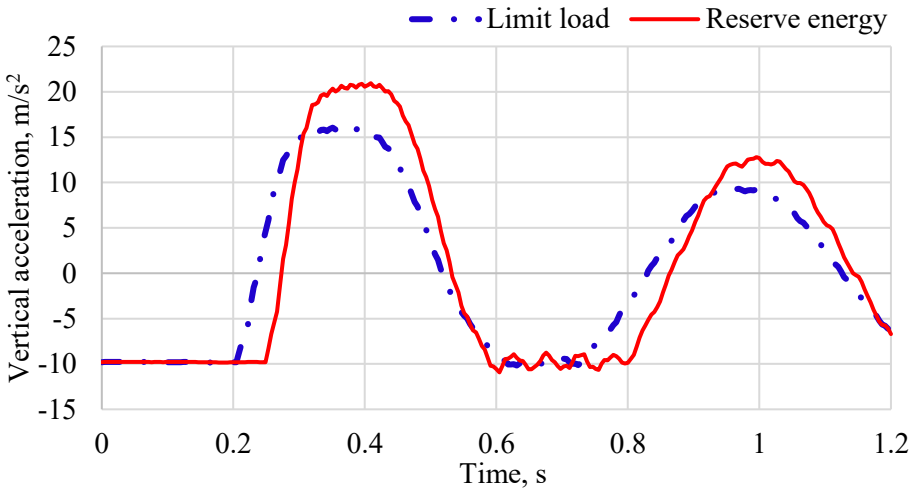

Fig. 2.9. Time history of helicopter C.G. acceleration.

To assess the integrity of the SLG structure from the strength perspective, load factor (n) is calculated. By substituting the values of A_y, m_e, m, g, and L for each drop test condition into Eq. (1.2), values of (n) are determined and tabulated in Table 2.7. It is observed that the load factors have adequate margin below the ultimate value of 3.5 g's [9]. However, the magnitude of the load factor does not quantify the stress in the crosstubes which is computed in FE analysis as will be shown later.

Table 2.7. Load factors for limit load and reserve energy drop tests.

Drop test type	v_0, m/s	A_y , m/s^2	n
Limit load	2.00	15.85	2.32 g's
Reserve energy	2.44	20.5	2.68 g's

The impact forces exerted by the ground on the four fittings at the junction between the skids and the crosstubes are shown in Figures 2.10 through 2.13. Again, the noisy forces are filtered using low pass Butterworth filter of 2nd degree with cut-off frequency of 24.5 Hz. The Figures show that the rear fittings are subjected to high impact forces compared to the forward crosstubes due to their relative closeness to the center of gravity of the helicopter.

2.6.3 Specific energy absorption and total energy balance

The Specific Energy Absorption (SEA) measure is of paramount importance because it determines the amount of energy absorbed per kilogram mass of the component or structure. The skid landing gear should therefore, be designed to retain high level of specific energy absorption

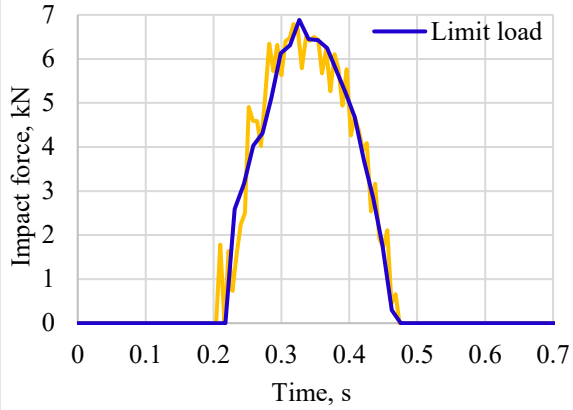

Fig. 2.10. Time history of impact force on the skid-forward crosstube fitting.

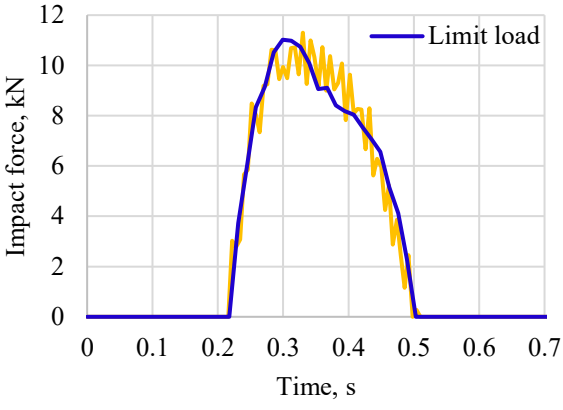

Fig. 2.11. Time history of impact force on the skid-aft crosstube fitting.

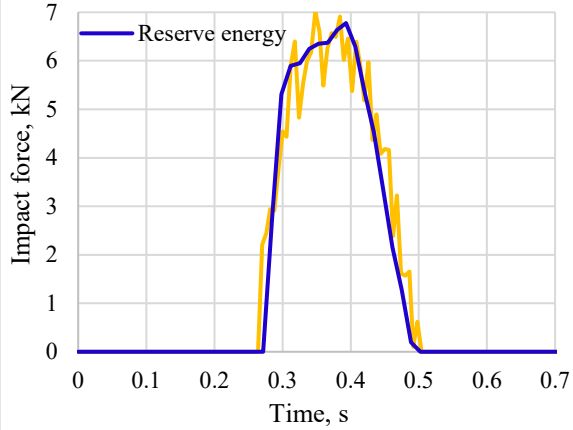

Fig. 2.12. Time history of impact force on the skid-forward crosstube fitting.

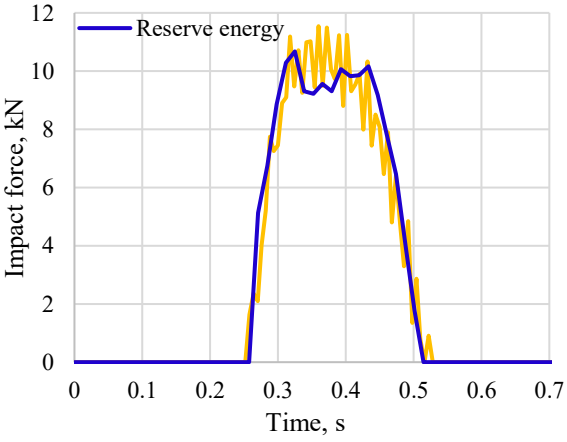

Fig. 2.13. Time history of impact force on the skid-aft crosstube fitting.

to minimize the acceleration transmitted to the payload. On the other hand, the structure should satisfy the requirements of the airworthiness related to the strength and weight. In the present study, the baseline skid landing gear design is assessed in terms of specific energy absorption while subjected to the limit load and reserve energy impact scenarios. The SEA can be described as [40]

$$SEA = \frac{Internal\ energy\ (I.E.)}{m_{ct}} \tag{2.19}$$

where m_{ct} is the mass of crosstubes. In the above equation, the mass of crosstubes is considered rather than the mass of the whole SLG since the impact energy is solely absorbed and dissipated by the bending of the cross members. The results of the SEA under reserve energy drop test condition (Ultimate drop test condition) is depicted in Figure 2.14. The time history of SEA shows

that the crosstubes absorb maximum of 702 J of internal energy per kg mass. The corresponding peak vertical acceleration is 20.5 m/s^2, as given in Table 2.7. The straight horizontal line segment between the first and second impacts in Figure 2.14 represents the plastic energy dissipation when the SLG departs the ground. In other words, out of 702 J/kg, about 300 J/kg is recovered and the remainder is plastically dissipated through the plastic bending of the cross members. As a result, the permanently distorted crosstubes cannot be used any more in the SLG and need to be replaced before setting new takeoff.

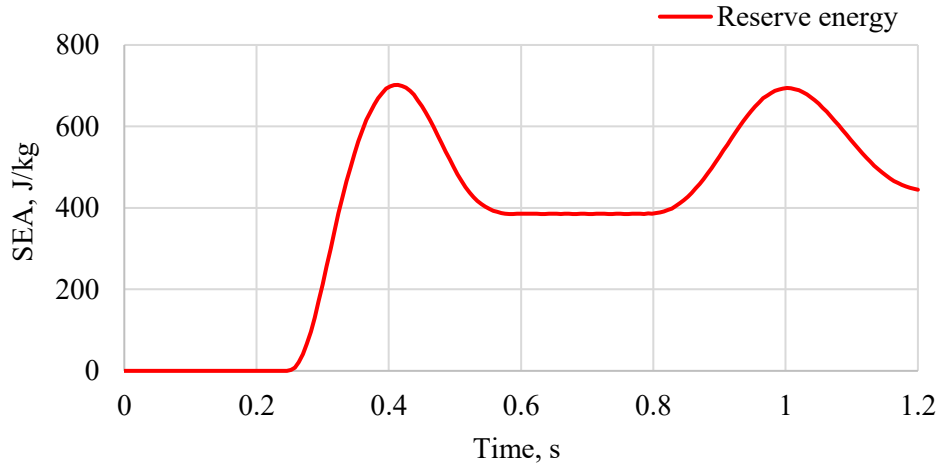

Fig. 2.14. Time history of SEA for the crosstubes.

Figure 2.15 illustrates the strain energy versus the vertical displacement of the helicopter C.G. for the first two loading-unloading cycles. The first cycle is designated by path A-B-C-D while the second is defined by path D-E-F. In the Figure, it can be seen that the elastic strain energy increases dramatically with the increase in the elastic deformation of the helicopter C.G. (path A-B). Then, it grows with a slower pace along path B-C as more energy is plastically dissipated. The rebound stroke is designated by curved segment C-D. As the system rebounds, the elastic energy is released until the residual energy decreases to 100 J at point D. Up to this point, the crosstubes dissipate about 3400 J by the plastic deformation, as shown in Figure 2.16. In the second loading process (Compression), the impact energy is further dissipated and led to a significantly large residual deformation of about 90 mm (point F) due to stiffness degradation, as shown in Figure 2.6. In the figure, zero plastic deformation occurs along the straight segment A-A′ since the energy absorbed is due to the elastic deformation of the SLG, as shown in Figure 2.15. Beyond A′, the deformation

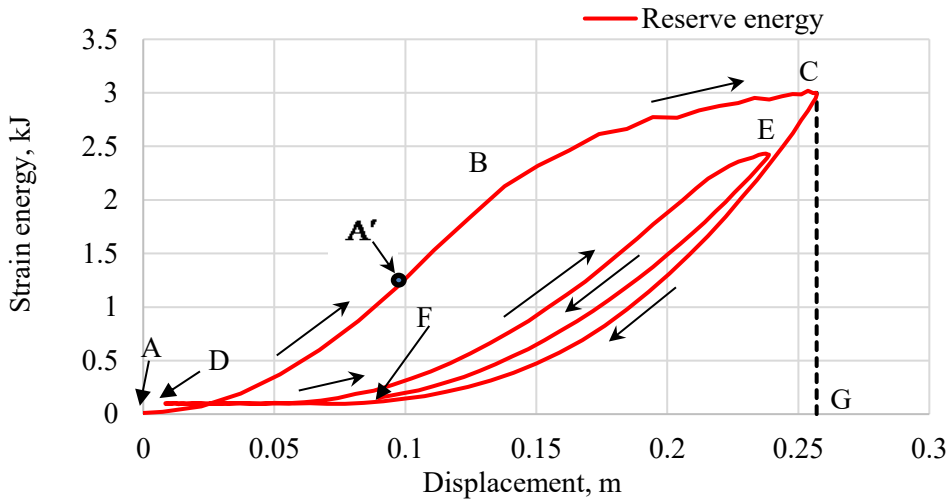

Fig. 2.15. Strain energy vs. C.G. vertical displacement.

ramps up rapidly to C with total energy of 3400 J dissipated plastically. Figure 2.15 shows that 3000 J of strain energy available at C is recovered during the unloading process so that the helicopter elastically retains the most of its travel up to 8.5 mm below the original equilibrium position (A), as explained in the previous paragraph. In the second impact (path D-E-F), additional energy of 476 J is plastically dissipated. Despite the plastically dissipated is relatively small in the second impact, the C.G. attained 90 mm at the end of the second unloading process. This is attributed to the substantial degradation in the inelastic stiffness of the SLG, which is approximated in Figure 2.3 to 63855 down from 261891 N/m (75.6% drop). From Figure 2.16 it can also be concluded that about 61% of internal energy is plastically dissipated in the first two loading-unloading cycles. This infers that the cross sections of the crosstubes have undergone high plastic deformation.

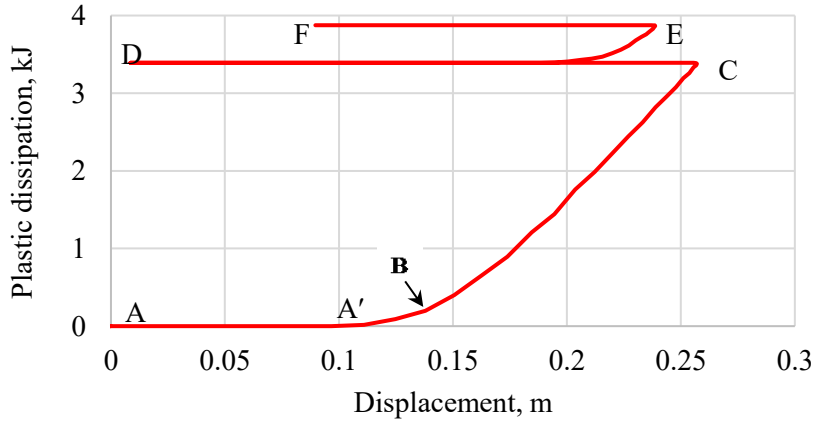

Fig. 2.16. Plastic dissipation vs. C.G. displacement.

The second method of validating the FE model and the simulation results is to ensure that the total energy of the system is zero or close to zero throughout the simulation time, as explained in section 1.4.2. This objective is successfully achieved for both drop test simulations as shown in Figure 2.17. The total energy of the model is found to be less than 6 J.

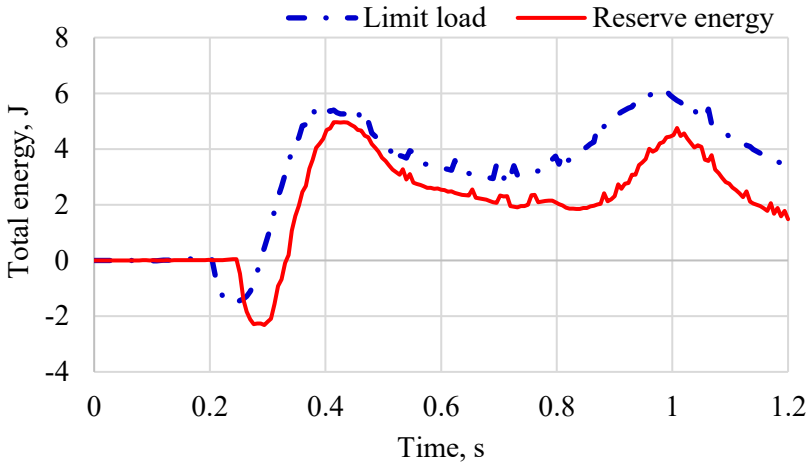

Fig. 2.17. Time history of total energy.

2.6.4 Failure modes of the skid landing gear

Although the evaluated load factors (provided in Table 2.7) confirmed that the SLG structure did not fall apart, it did not quantify the stresses in the crosstubes. To accomplish this task, the SLG structure is analyzed in ABAQUS to determine the distribution of stress and strain in the critical areas around the fittings between the crosstubes and the fuselage to identify the possible failure. This entails adopting of the following two material failure criteria:

- Von Mises yielding criterion, and
- Maximum equivalent plastic strain.

From the perspective of material strength, Ref. [36] indicated that the ultimate true strain at the maximum load on aluminum alloy 7075-T6 is 0.095 assuming no residual plastic strain exists in the cross members prior to the impact. Therefore, the maximum allowable plastic strain of 0.095 is the ultimate true strain at which the cross section becomes entirely plastic. Moreover, the effect of strain rate is neglected as aluminum alloys are found not sensitive to strain rates up to 10^3 s^{-1} [41]. The fittings between the fuselage and the crosstubes are modeled in ABAQUS as rigid beam elements by considering their strength as multi-fold of the strength of SLG flexible crosstube

components. Thus, the focus is concentrated on analyzing the behavior of the crosstubes under impact. The load factors in Table 2.7 indicated that the SLG survived the two standard impacts. However, the calculated load factors do not quantify the stresses and strains in the crosstubes. Here, von Mises stress and the equivalent plastic strain in the crosstubes are computed using ABAQUS to verify whether they exceed their respective maximum allowable values, as required by the above failure criteria.

2.6.4.1 Von Mises yielding criterion

For the general three dimensional stress state, the von Mises yielding criterion for ductile material can be expressed in terms of the three principal stresses as [42]:

$$\sigma_v^2 = \frac{1}{2}[(\sigma_1 - \sigma_2)^2 + (\sigma_2 - \sigma_3)^2 + (\sigma_3 - \sigma_1)^2] \tag{2.20}$$

The component yields if the following condition is satisfied

$$\sigma_v > \sigma_y \tag{2.21}$$

where σ_1, , σ_2, and σ_3 are the principal stresses and σ_y is the yield stress of the SLG material. Eq. (2.20) indicates that ductile materials such as aluminum alloys start to yield when the equivalent von Mises stress exceeds the yield stress of the material. As provided in Table 2.3, the yield and ultimate stresses of the selected material are 531 and 658 MPa, respectively. Figures 2.18 and 2.19

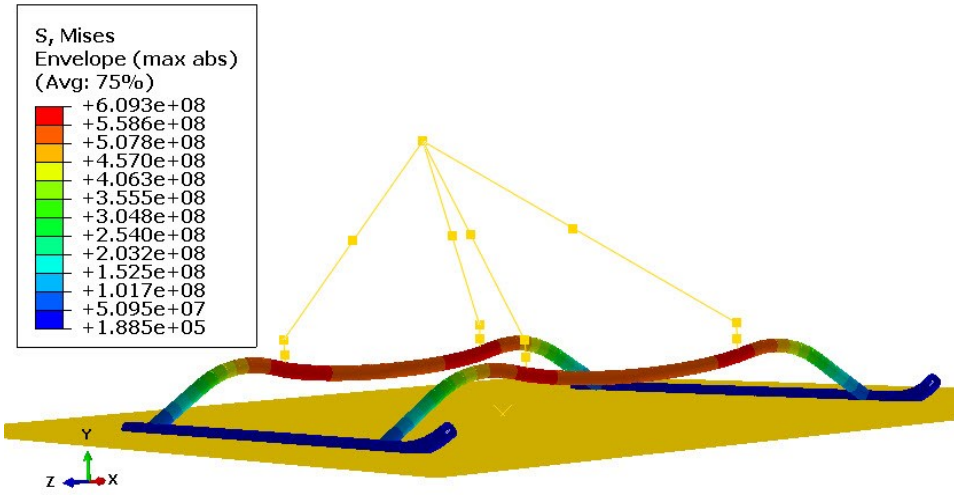

Fig. 2.18. Von Mises stress distribution for limit load drop test.

illustrate the distribution of von Mises stress in the SLG in the limit load and reserve energy drop test, respectively. The maximum von Mises stress is found to be 609 and 612 MPa for limit load and reserve energy drop tests. These stresses are beyond the yield stress and caused permanent plastic deformation in the cross members.

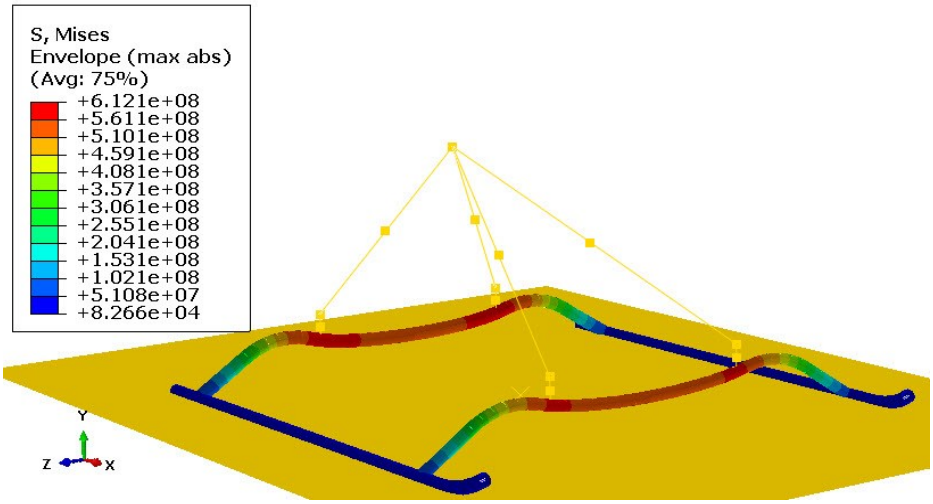

Fig. 2.19. Von Mises stress distribution for reserve energy drop test.

2.6.4.2 Maximum equivalent plastic strain (PEEQ)

For ductile materials subjected to impact loads, the yield point is often exceeded and strain-hardening occurs. For multiaxial stress state, the equivalent plastic strain (PEEQ) is a scalar quantity which measures the amount of permanent strain. The plastic work can be described as [43]

$$W = \int \sigma_v d\varepsilon_p \tag{2.22}$$

where ε_p is the equivalent plastic strain. The energy distortion theory expects that the failure to occur when the plastic work, W, in the multiaxial stress state exceeds that associated with uniaxial tensile test. It means

$$\int \sigma_v \, d\varepsilon_p \geq \int \sigma_1 \, d\varepsilon_1 \tag{2.23}$$

where $\sigma_1$is the uniaxial stress and ε_1 is the uniaxial strain. Obviously, in the uniaxial test, the stress occurs in one direction so that

$$\sigma_v \rightarrow \sigma_1 \quad \text{and} \quad d\varepsilon_p \rightarrow d\varepsilon_1 \tag{2.24}$$

Ref. [43] assumes that the individual stress components increase or decrease at the same rate as the loading is applied. Hence

$$\varepsilon_p \geq \varepsilon_1 \tag{2.25}$$

In other words, the failure of the part occurs when the value of maximum PEEQ exceeds the uniaxial design/ultimate true strain. The later can be calculated by integrating the true stress-strain curve obtained from uniaxial test data. Figures 2.20 and 2.21 illustrate the distribution of the equivalent plastic strain in the crossbeams. In these Figures, it is noticed that the maximum PEEQ are 0.0333 and 0.035 for limit load and reserve energy test, respectively. These values are 65%

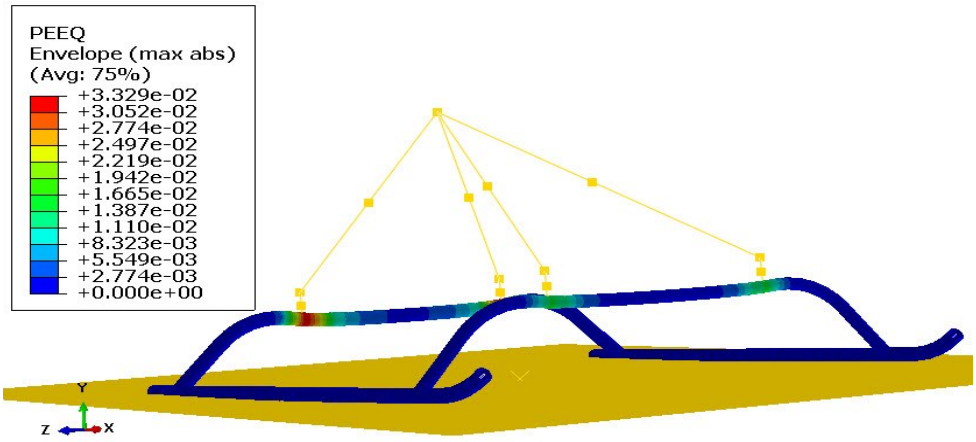

Fig. 2.20. PEEQ distribution for limit load drop test.

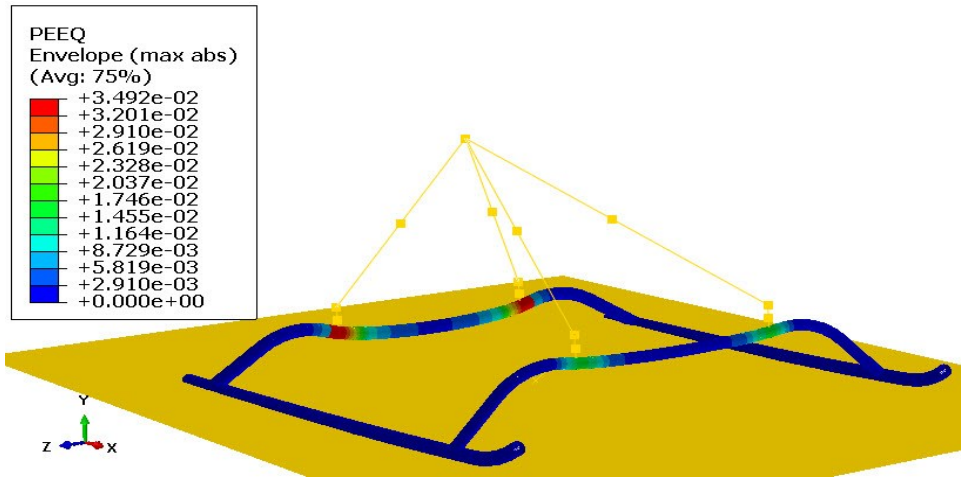

Fig. 2.21. PEEQ distribution for reserve energy drop test.

and 63.2% below the maximum PEEQ and are attained in the vicinity of the fitting between the aft crosstube and the fuselage. The maximum PEEQ in the forward crosstube is the lowest due to its relative remoteness from the C.G. compared to the backward tube. Based on this criterion none of crosstubes failed. However, the crosstubes incur permanent deformation which renders them malfunctioned.

2.7 Summary

In this chapter, the dynamic response of the baseline skid landing gear system is studied under limit load and reserve energy drop tests. These drop tests were simulated in finite element software ABAQUS. In both test, the reference SLG could successfully attenuate impact loads through the plastic deformation of the crosstubes. However, the plastic deformation rendered the SLG non-useable and must be replaced before the next flight. To facilitate the selection of the right effective mass of the helicopter based on the anticipated vertical impact speed and the permissible maximum deflection of the helicopter C.G., two charts were introduced. One is for $L = 0.67$ and the other is for $L = 1.0$. These charts, reduces the computational time at preliminary stages of the SLG design.

CHAPTER 3

Design Optimization of the Conventional SLG System

3.1 Introduction

SLGs exhibit high geometrical and material nonlinearity in hard landing and crashes. Therefore, obtaining a lightweight SLG designs while enhancing the energy absorption capacity is a very challenging task. The skid landing gears are mandated, to the greatest possible extent, to simultaneously comply with the requirements of both airworthiness and crashworthiness regulations. Therefore, the crosstubes should be carefully designed to reach an appreciable weight reduction while maximizing their energy absorption capabilities within the prescribed design constraints such as the permissible stroking distance, the load factor, and the size.

In this chapter, the first objective is to reduce the mass of the SLG to provide a sufficient room for incorporating the MREA into the conventional SLG. The MREA will be first optimized in Chapter four and then incorporated in the SLG in Chapter five. The reduction in the mass of the conventional SLG complies with the general airworthiness requirements of aircrafts in terms of minimizing their structural weight. Simultaneously, the SLG mass reduction is associated with the increasing the SLG's specific energy absorption to decrease the sudden vertical acceleration to which the occupants are subjected. To fulfil these goals, the cross sectional dimensions of the crosstubes, i.e. radius and thickness, are optimized to maximize the specific energy absorption, SEA. The design optimization is performed based on the reserve energy drop test condition which represents the ultimate crashworthiness design condition for the civil helicopter. Approximate functions for SEA, crosstubes mass, C.G. displacement, and load factor are developed using the response surface method and design of experiment technique to mimic the behavior of the FE model over the entire design space. Using response surface function, the design optimization problem is formally formulated and then solved using nonlinear mathematical programing technique based on the sequential quadratic programming (SQP) method. Using ABAQUS, the dynamic response of the SLG with optimum configuration is obtained and compared to the baseline design. It is concluded that the optimum SLG could increase the SEA by 35% and minimize the crosstubes mass by 24.5%. In addition, the optimum design utilizes 97.4% of the design impact stroke of 350 mm in comparison to 73.4% for the baseline SLG. This led to a drop

in the acceleration that would be experienced by the occupants by about 25%. To facilitate conducting drop test and reducing the test setup time, the new charts for the governing parameters, similar to those in chapter two, are introduced for the optimum SLG configuration.

3.2 Literature review

For the crosstubes, the challenge of increasing the impact energy absorption in the event of impact can be tackled either by optimizing the cross sectional dimensions, selecting alternative materials, or adopting circular or non-circular cross section to meet crashworthiness requirements. Tho *et al.* [12] employed LS-DYNA to simulate a dynamic drop of helicopter skid landing gear. Using this tool, the computational cost was eventually reduced from 1-2 days to 12 minutes. Airoldi and Lanzi [44] optimized a SLG to minimize the load factor while trading-off between the strength and landing performance of the SLG. In order to perform the study, they linked the Genetic Algorithm (GA) to Musiac software. Musiac software is a multibody optimization code developed at Politecnico di Milano to solve the dynamic and nonlinear model of the skid landing gear system. The study considered impacts on both soft and hard terrain at maximum vertical landing velocity of 2 m/s. In their subsequent study, the authors optimized SLG of two helicopters with different masses [45]. They utilized Musiac to fulfill the objective of minimizing the load factor to attain the best landing performance. The numerical results were validated using experimental results of drop tests. In this study, the distribution of bending moment along the crosstubes was successfully predicted with acceptable accuracy at lower computation costs. Tho and Wang [46] proposed an optimization algorithm called the Sequential Regularized Multi-Quadric regression with Output Space Mapping (SRMQ/OSM). The method improved the efficiency of energy absorption under the given design constraints. The authors demonstrated that the results could quickly converge to the feasible design solution without violating the problem constraints. In this study, the mass of the skid landing gear system was reduced by 7.2 kg and the total computational cost was reduced by 70%. Moreover, the specific energy (SEA) absorption was increased by 13.1%. The designed SLG exhibited better impact performance with a mass reduction which is considered as a valuable progress in aerospace industry. Another SLG optimization alternate was proposed by Shrotri [47]. A metallic aluminum alloy 7075 skid gear was replaced by composite material (Ke49/PEEK skids, 48 ply IM7/8552) to reduce the weight of the skid gear. The study results revealed a reduction in weight by 49% compared to the metallic

skid gear. Also, it demonstrated that the composite skid gears could be worthy from the prospective of crashworthiness as they complied with the requirements of kinetic energy dissipation as per MIL-STD-1290A (AV).

3.3 Response surface method and design of experiment technique

Conducting a design optimization using the full nonlinear finite element (FE) model is hampering and computationally very expensive. The reason is that at each optimization iteration, the FE model may be run several times. Moreover, since the dynamic responses obtained using FE model are typically noisy (especially under impact load), the gradient based optimization algorithms may not be used since the accurate evaluation of the gradient of responses is not always possible. In such circumstances, the response surface method (RSM) and the design of experiment (DoE) technique can be effectively utilized to develop approximate smooth and explicit objective and constraint response functions.

The response surface method basically attempts to formulate an approximate surrogate model of the real structure. It is composed of collection of mathematical and statistical techniques. In the optimization of complicated problems, such as the crashworthiness problems, the RSM combined with DoE can be effectively used to derive polynomial response surface functions of the desired outputs with respect to the identified design parameters. These response functions explicitly depend on identified design variables which can then be conveniently used in the design optimization problems instead of using computationally expensive full FE models. A quadratic or cubic polynomial functions are generally found sufficient to emulate the desired response.

To formulate the RSM, let us assume a complete polynomial of 2nd order so that the approximate response function can be represented as [48]

$$\hat{y} = \beta_0 + \sum_{j=1}^{n} \beta_j x_j + \sum_{j=1}^{n} \beta_{jj} x_j^2 + \sum_{i \neq j} \sum_{j=2}^{n} \beta_{ij} x_i x_j \tag{3.1}$$

where $\hat{y}$ is the approximated response functions determined by the RSM at specified design points identified by DoE in the design space; β_0, β_j, β_{ij}, β_{jj}, are the unknown regression coefficients to be identified, x_i and x_j are the design variables. Considering k as the number of sample design points identified in design space, we may write Eq. (3.1) in matrix notation as

$$\hat{y} = X\,\beta \tag{3.2}$$

here X is the $k \times p$ design matrix and p is the number of regression coefficients (β's). The error (residue) in the approximation process, ε, can be written as

$$\varepsilon = y - \hat{y} \tag{3.3}$$

where y is the true response. The optimum approximate meta-model is the model which minimizes the residue between responses of the approximate and true models. The technique of least squares is utilized for this purpose. By substituting Eq. (3.2) into (3.3), the square of the error can be expressed in the matrix form as

$$\varepsilon^T \varepsilon = (y - X\,\beta)^T\ (y - X\,\beta) \tag{3.4}$$

In this equation, the superscript, T, denotes the vector or matrix transpose. The minimization of the square of the error in Eq. (3.4) yields coefficients, β. This can be achieved by differentiating Eq. (3.4) with respect to the elements of β and then equating the resultant equations to zero as

$$\beta = (X^T X)^{-1}\ X^T y \tag{3.5}$$

It is noted that qualities y, $\hat{y}$, ε and β are expressed in vector form.

3.4 Accuracy of the approximate response function

To ensure that the developed regression meta-model, is an accurate and reliable estimator and can generate the desired output without executing the full FE model, it is necessary to utilize the method of coefficient of multiple determination, R^2 [40, 48]. R^2 verifies the accuracy of the derived approximate functions in predicting the response of the real system and can be expressed as [40]

$$R^2 = 1 - \frac{SS_E}{SS_T} \tag{3.6}$$

where

$$SSE = \sum_{i=1}^{k} (y_i - \hat{y}_i)^2 \tag{3.7}$$

and

$$\text{SST} = \sum_{i=1}^{k} (y_i - \bar{y})^2 \tag{3.8}$$

here y_i is the true output responses calculated from experiment or finite element analysis, $\hat{y}_i$ is the approximate response determined using the developed RSM functions, $\bar{y}$ is the average scalar value of the true response, and *i* denotes the design point. R^2 varies from zero to one in which the values of R^2 closer to one means the approximate function is able to predict the response more accurately. The drawback of using R^2 alone is that its value always increases by adding additional variables, which may sometimes not be statistically significant to the model's approximate nature. To overcome the deficiency of this accuracy measure, an additional statistical measure called adjusted R^2, or R^2-adj, is considered because it does not increase with the addition of the unnecessary variables to the approximate function [40, 48]. R^2-adj can be expressed as:

$$R^2 - \text{adj} = 1 - \frac{s-1}{s-p}(1 - R^2) \tag{3.9}$$

Several statistical programs such as Minitab provides these measures based on a hypothetical testing of the regression model derived using RSM [51].

3.5 Design of experiment techniques

Design of experiment (DoE) is a strategy that has primarily been developed to fit the models of physical experiments. Then, the approach has been extended for the use with the finite element simulations. The DoE are statistical techniques which rely on the analysis of variance to choose as fewer as possible points where the response should be evaluated to fulfill the following two objectives: i) Minimize the computational cost by selecting the optimum number of experiments to be conducted; and ii) Maximize the amount of information gained from the conducted experiments to develop a satisfactory surrogate model using the RSM. To accomplish the above objectives, several DoE methods have been developed. The Factorial, Central composite, Box-

Behnken, and D-optimality are examples of these methods. Brief descriptions of these DoE approaches are provided in the following sub-sections.

3.5.1 Factorial design method

In this category two factorial design methods are used to design experiments. Namely, the full and the fractional factorial experiments. In the full factorial experiment design, all possible combinations of levels for all design variables are studied. If the number of design variables is denoted by n, then the number of experiments at 2 levels is calculated as 2^n. At 3 levels it becomes 3^n, etc. The full factorial approach is found useful in the preliminary stage of design when the number of design variables is less than or equal to 4. However, when there is no adequate time, resources and budget, this method becomes prohibitively expensive and not attractive [52]. On the other hand, the fractional factorial designs are found more beneficial when the interaction terms of the 3rd order or higher are assumed having negligible influence on the accuracy of the approximate response function [52]. In this method, the number of experiments at 2 levels is determined as $2^{(n-l)}$, where l represents the size of the fraction and $(\frac{1}{2})^l$ is the fraction of the full factorial. For example, by assuming $n = 5$ and $l = 2$, the number of full factorial experiments is 32 whereas the number of fractional factorial experiments is one-fourth of the full factorial which is 8 experiments in total.

3.5.2 Central composite design (CCD)

The CCD is one of the most commonly used experiment methods that uses the 2-level factorial designs. Structurally, it uses full factorial design (2^n) plus $2n$ axial points and one center point ($2^n + 2n + 1$).

3.5.3 Box-Behnken design (BBD)

The BBD requires only three levels to run an experiment. In this method, each design parameter, n, is placed at one of three equally spaced values, as shown in the example of the three design variables experiment in Figure 3.1. Furthermore, it does not contain any points at the corners (vertices) of the cube or experiment region which turns BBD to a special 3-level design method. Thus, the BBD requires fewer treatment combinations than the CCD [53]. In addition,

BBD can fit full quadratic model. In BBD criterion, for p regression coefficients, the number of design points (s) is bounded by $1.5p$ and $2.6p$.

3.5.4 D-Optimality

The D-optimality experimental design technique is based on maximizing the determinant $|X^T X|$ in Eq. (3.5) which corresponds to minimizing the variance of the vector of the unknown regression coefficients, β's, within the estimated response of the surrogate model [54].

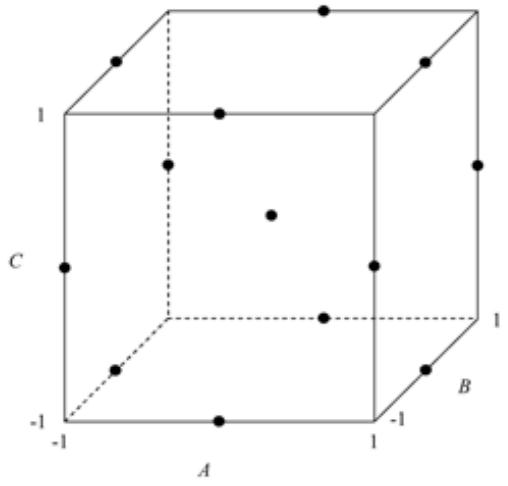

Fig. 3.1. Three design variables for BBD [53].

3.6 Sequential Quadratic Programming optimization method (SQP)

The approximate objective and constraint functions obtained using RSM can be effectively used to optimize the cross sectional dimensions of the crosstubes, i.e. radius and thickness. In this chapter, the formulated nonlinear optimization problem is solved using Sequential Quadratic Programming (SQP) method which is a powerful gradient based technique to solve nonlinear programming problems. A brief overview on the SQP is given below.

The SQP algorithm is a quite popular derivative-based optimization method used in solving the nonlinear programming problems. The algorithm incorporates information about the second order problem functions. Mainly, the SQP algorithms involves the following two steps [55]

- Define, use and solve a quadratic programming (QP) subproblem to calculate the search direction (d) in the design space. This step utilizes the values and the gradients of problem functions. The QP subproblem is strictly convex and it guarantees capturing the global optimum (if one exists).
- Define and solve a step size subproblem to minimize the descent function and calculate the step size along the search direction.

Mathematically, the QP subproblem can be expressed as [55]

Minimize

$$\bar{f} = c^T + \frac{1}{2} d^T d \tag{3.10}$$

Subject to linear constraints:

$$N^T d = e \tag{3.11}$$

$$A^T d \leq b \tag{3.12}$$

The QP subproblem is to be solved at each iteration. The solution gives the search direction d and the values of Lagrange multipliers for the constraints which are needed to compute the descent function. This function is then minimized to determine the values of the step size along d.

3.7 Design optimization of the skid landing gear

Here, four design variables, namely the outer radii and thicknesses of the aft and forward crosstubes are the subject of size design optimization. RSM and DoE have been utilized to obtain the approximate objective and constraint functions of the desired responses (SEA, mass, maximum C.G. displacement, and maximum load factor) with respect to the identified design variables. The developed meta-models are capable of approximating the response of the SLG system with high accuracy. The objective of the present design optimization study is to maximize the SEA while maintaining the constraints within the prescribed bounds. These constraints involve crosstubes mass, C.G. displacement, load factor, and outer radii and the thicknesses of the tubular cross members. The formulated optimization problems have been solved using SQP algorithm in MATLAB platform. SQP is a local optimizer which may trap in a local optimum without any mechanism to climb up. Therefore, to ensure catching the global optimum solution, different initial

design points are selected randomly. If all these initial points converge to the same solution and the same optimum values of the design variables, then the global optimum solution is the most probably captured.

To derive the approximate meta-models, the response of the helicopter is initially calculated using FE ABAQUS for random design points generated by the DoE method within the design space. Box-Behnken experiment design criteria is used to generate 27 sets of design variables within the design space. In all these simulations the helicopter impacts the ground at 2.44 m/s with level attitude and rotor lift factor of one. Sample of the computed responses are presented in Table 3.1.

Table 3.1. Sample of FE model responses on DoE design points.

Design Points				FE Model Responses			
x_1 *mm*	x_2 *mm*	x_3 *mm*	x_4 *mm*	m_{ct} *kg*	δ_{max} *mm*	n_{max} *g's*	*SEA J/kg*
44	5	44	5	21.5	129.7	5.06	288.9
37	8	37	2	17.4	180.5	3.84	373.3
37	8	44	5	24.42	134.6	4.93	249.7
30	5	37	8	20.8	178.2	3.90	266.3
37	5	44	2	13.39	185.8	3.49	482.5
37	2	30	5	10.85	281.9	2.67	594.5
37	5	30	8	19.71	189.8	3.71	320.9
30	2	37	5	11.94	237.9	2.96	459.7
44	5	37	8	24.42	136.3	4.90	258.8
30	5	44	5	17.87	166.5	3.97	305.4

3.7.1 Approximate response functions obtained by RSM and DoE

To capture the response of the SLG more accurately, full quadratic representation of the approximate response functions is obtained using the RSM. For the four design variables, the expanded form of the approximate function can be expressed as

$$\hat{y} = \beta_0 + \beta_1 x_1 + \beta_2 x_2 + \beta_3 x_3 + \beta_4 x_4 + \beta_{11} x_1^2 + \beta_{22} x_2^2 + \beta_{33} x_3^2 + \beta_{44} x_4^2 + \beta_{12} x_1 x_2 + \beta_{13} x_1 x_3 + \beta_{14} x_1 x_4 + \beta_{23} x_2 x_3 + \beta_{24} x_2 x_4 + \beta_{34} x_3 x_4 \quad (3.13)$$

In Minitab software, D-Optimality is also used to perform a hypothetical testing of the regression model derived using RSM for the given design space. In this case the determinant $|X^T X|$ equals

to 3.305×10^{12}. This value is found sufficiently large to decrease the variance of the vector of the unknown regression coefficients.

Considering Eq. (3.13) and Table 3.1, matrix X for different response outputs can be evaluated from which one can evaluate the coefficient vector, β, from Eq. (3.5). The developed approximate response functions are outlined in the following sub-sections.

3.7.1.1 Approximate response function of the SEA

Using RSM, the SEA response of the crosstubes can be approximated using the following quadratic function

$$SEA = 2622 - 13776\,x_1 - 228245\,x_2 - 17783\,x_3 - 268818\,x_4 + 4795979\,x_2^2 + 7501627\,x_4^2 + 1953247\,x_1x_4 + 1911686\,x_2x_3 + 13962504\,x_2x_4 \quad (3.14)$$

The values of R^2 and R^2-adj are calculated as 94.86% and 88.86%, respectively.

3.7.1.2 Approximate response function of the crosstubes mass

The approximate function of the crosstubes mass can be represented as:

$$m_{ct} = -0.0478 + 0.714\,(x_1 + x_3) + 3.94\,(x_2 + x_4) - 25949.1\,(x_2^2 + x_4^2) + 51785.7\,(x_1x_2 + x_3x_4) - 119\,(x_1x_4 + x_2x_3) + 277.8\,x_2x_4 \quad (3.15)$$

The values of R^2 and R^2-adj are almost equal to 100%.

3.7.1.3 Approximate response function of maximum C.G. displacement

The maximum C.G. displacement response function is found to be:

$$\delta_{max} = 1.483 - 19.01\,x_1 - 75.1\,x_2 - 19.05\,x_3 - 73.7\,x_4 + 1720\,x_2^2 + 1634\,x_4^2 + 277\,x_1x_3 + 839\,x_1x_4 + 834\,x_2x_3 + 2963\,x_2x_4 \quad (3.16)$$

The values of R^2 and R^2-adj are calculated as 96.67% and 92.78%, respectively.

3.7.1.4 Approximate response function of maximum load factor

The maximum load factor response is also approximated using the following quadratic function:

$$n_{max} = 0.761 - 41.1\,x_1 + 25.4\,x_2 - 7.4\,x_3 + 112.3\,x_4 + 928\,x_1^2 - 11335\,x_2^2 + 581\,x_3^2 - 15123\,x_4^2 + 12168\,x_1x_2 - 2322\,x_1x_4 - 2770\,x_2x_3 - 9814\,x_2x_4 + 9746\,x_3x_4 \quad (3.17)$$

The values of R^2 and R^2-adj are calculated as 99.88% and 99.74%, respectively.

3.8 Formulation of the optimization problem

The above approximate response objective and constraint functions of the model which are given in Eqs. (3.14) to (3.17) along with the size constraint functions can now be used to formally formulate the optimization problem. Here, the design objective is to maximize the *SEA* of the crosstubes by increasing the amount of internal energy the tubes can absorb. The applicable constraints in the optimization problem include:

1) The total mass of the crosstubes should not exceed the mass of the original crosstubes, i.e. $m_{ct} \leq 9.06$ kg;
2) Displacement of the helicopter C.G. should not exceed a prescribed deflection of 350 mm to maintain the SLG intact, though allowing some degree of plastic deformation;
3) Flight load factor should not exceed 3.5 to preserve the durability of the helicopter structure against the ultimate impact loads during landing;
4) External radii (x_1 and x_3) of aft and forward crosstubes should be in the range of 30-44 mm and tubes thicknesses (x_2 and x_4) are from 2 to 8 mm.

The design optimization problem can now be formally formulated as:

Find Design variable vector X^*:

To maximize SEA (of the crosstubes)

Subject to: $Mass - Mass_{\text{(baseline)}} \leq 0$

$\delta_{max} - \delta_{max(baseline)} \leq 0$

$n_{max} - n_{max\ (standard)} \leq 0$

$x_L \leq x_i \leq x_U$

Now, considering the developed response functions in Eqs. (3.14) to (3.17), one can write:

Find Design variable vector X^* in m

to maximize

$$SEA = 2622 - 13776\,x_1 - 228245\,x_2 - 17783\,x_3 - 268818\,x_4 + 4795979\,x_2^2 + 7501627\,x_4^2 + 1953247\,x_1x_4 + 1911686\,x_2x_3 + 13962504\,x_2x_4 \quad (3.18)$$

Subject to the following inequality constraints:

$$g_1(x) = -9.1078 + 0.714\,(x_1 + x_3) + 3.94\,(x_2 + x_4) - 25949.1\,(x_2^2 + x_4^2) + 51785.7\,(x_1x_2 + x_3x_4) - 119\,(x_1x_4 + x_2x_3) + 277.8\,x_2x_4 - 9.06 \le 0 \quad (3.19)$$

$$g_2(x) = 1.133 - 19.01\,x_1 - 75.1\,x_2 - 19.05\,x_3 - 73.7\,x_4 + 1720\,x_2^2 + 1634\,x_4^2 + 277\,x_1x_3 + 839\,x_1x_4 + 834\,x_2x_3 + 2963\,x_2x_4 - 0.350 \le 0 \quad (3.20)$$

$$g_3(x) = -2.739 - 41.1\,x_1 + 25.4\,x_2 - 7.4\,x_3 + 112.3\,x_4 + 928\,x_1^2 - 11335\,x_2^2 + 581\,x_3^2 - 15123\,x_4^2 + 12168\,x_1x_2 - 2322\,x_1x_4 - 2770\,x_2x_3 - 9814\,x_2x_4 + 9746\,x_3x_4 - 3.5 \le 0 \quad (3.21)$$

$$g_4(x) = -x_1 + 0.03 \le 0 \quad (3.22)$$

$$g_5(x) = x_1 - 0.044 \le 0 \quad (3.23)$$

$$g_6(x) = -x_2 + 0.002 \le 0 \quad (3.24)$$

$$g_7(x) = x_2 - 0.008 \le 0 \quad (3.25)$$

$$g_8(x) = -x_3 + 0.03 \le 0 \quad (3.26)$$

$$g_9(x) = x_3 - 0.044 \le 0 \quad (3.27)$$

$$g_{10}(x) = -x_4 + 0.002 \le 0 \quad (3.28)$$

$$g_{11}(x) = x_4 - 0.008 \le 0 \quad (3.29)$$

As mentioned earlier, the optimization problem has been solved using SQP algorithm implemented in MATLAB environment. The results are presented and discussed in the next section.

3.9 Results and discussion

Sample of the calculated optimum design parameters (x_1, x_2, x_3, x_4) and their corresponding optimal SEA values for different initial points is provided in Table 3.2. Sample iteration history is also shown in Figure 3.2. From the Table, it can be realized that different initial points yield the same optimum solution which confirms capturing the global solution. In addition, the optimization problem converges to the global optimum solution in almost four iterations as shown in Figure 3.2

The effect of varying the thickness of the aft crosstube (x_2) on the objective function, while maintaining the other design parameters at their optimum values, is presented in Figure 3.3 for

Table 3.2. Convergence of the SQP to the maximum global solution.

Initial Point (X_0), mm	*SEA*, J/kg	Optimum *X*, mm
(44.0, 5.0, 44.0, 5.0)	943.1	(37.6, 2.0, 30.0, 2.0)
(37.0, 8.0, 37.0, 2.0)	943.1	(37.6, 2.0, 30.0, 2.0)
(30.0, 5.0, 37.0, 2.0)	943.1	(37.6, 2.0, 30.0, 2.0)
(30.0, 5.0, 30.0, 5.0)	943.1	(37.6, 2.0, 30.0, 2.0)
(44.0, 5.0, 37.0, 8.0)	943.1	(37.6, 2.0, 30.0, 2.0)

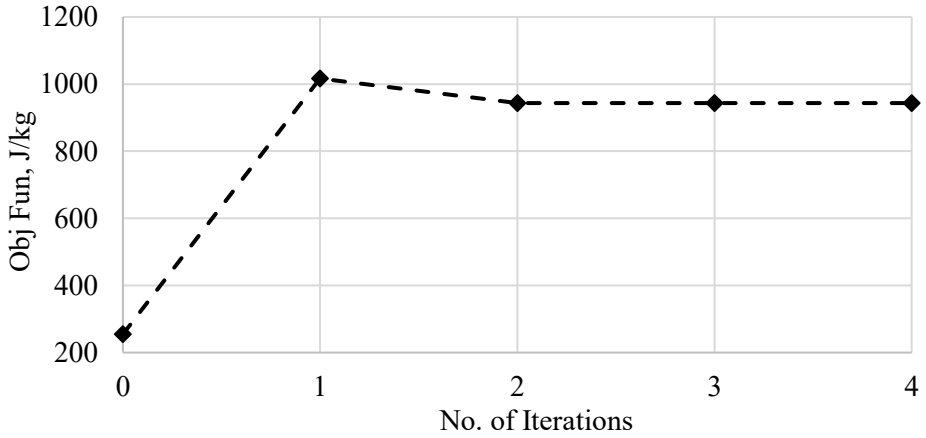

Fig. 3.2. Iteration history of the optimized SLG.

both the surrogate meta-model (RSM) and FE model (ABAQUS). The models show that the SEA decreases as the aft crosstube becomes thicker which is attributed to the increase in the stiffness. Generally speaking, good agreement exits between results obtained using developed RSM response function and those obtained using ABAQUS. The error varies from 2.5% to 13%. The

variation in the SEA results was taken into consideration by the adjusted coefficient of determination as maximum as 11.14%. Considering that the R^2-adj for mass approximation is almost 100%, the accuracy of the approximate displacement function (R^2-adj = 92.78%) appears to be the main contributing source to the estimated SEA error.

Fig. 3.4 compares the specific energy absorption of the SLG with optimum and baseline crosstubes. Both models are simulated in ABAQUS for 1.2 seconds. Similar to the baseline SLG, the axes zeros are the time and the height from where the helicopter is released. In regard to the

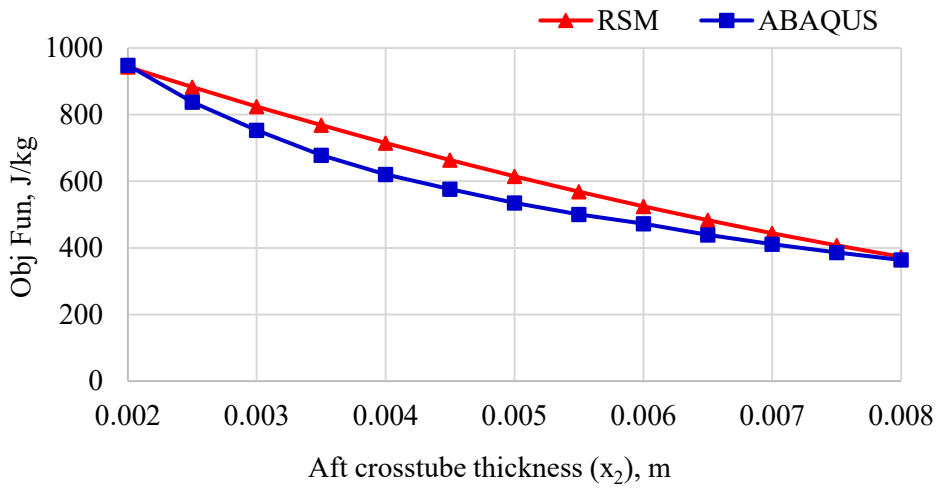

Fig. 3.3. Variation of SEA versus x_2.

optimum SLG, ABAQUS calculated peak SEA as 948 J/kg while the approximate RSM function computed the peak SEA as 943 J/kg. This is an excellent agreement with error less than 0.5%. Examination of results reveal that the optimize SLG could achieve maximum SEA of 948 J/kg compared to 702 J/kg for the baseline SLG. This shows almost 35% increase in SEA. The considerable improvement in SEA results in more displacement of the C.G. which is about 84 mm (32.7%) more than that of the baseline configuration, as shown in Figure 3.5. The extended travel of the optimum SLG indicates that almost 97.4% of the design stroke has been utilized (341 out of 350 mm). Consequently, the acceleration experienced by the payload has substantially decreased which is manifested in low load factor, as presented by graph 3.6. Considerable reduction of 18% in the load factor is attained with the optimum SLG design compared to baseline

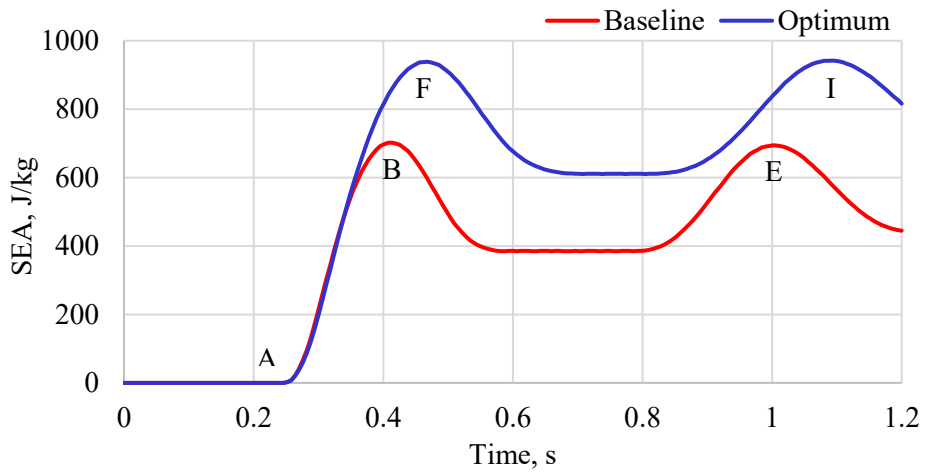

Fig. 3.4. Time history of SEA for the optimum SLG.

configuration. In terms of acceleration, the peak acceleration has reduced by 27.6% from 21 to 15.2 m/s^2. Figure 3.6 shows that the rate of onset of the load factor (acceleration) is lower in optimized SLG compared with the baseline design which means more tolerance to abrupt acceleration. Table. 3.3 compares maximum values of SEA, C.G. peak displacement, and load factor responses of the two rotorcraft models. It can be realized that the difference between responses of the helicopter equipped with the optimum SLG which are evaluated using the developed meta-models and FE model is insignificant. This demonstrates that the surrogate models can be efficiently used to optimize the highly nonlinear SLG system under impact loading instead of utilizing the computationally expensive full FE models.

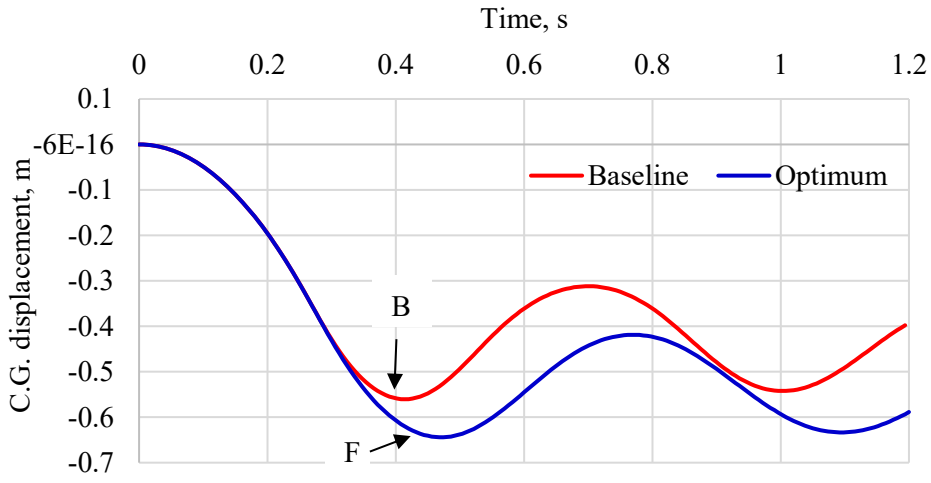

Fig. 3.5. Comparison of time history of C.G. displacements.

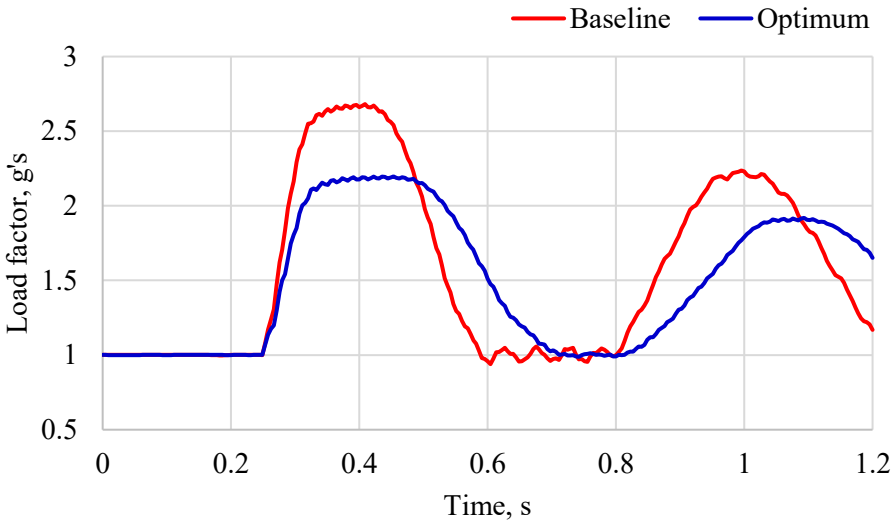

Fig. 3.6. Comparison of time history of load factors.

Table 3.3. Comparison of responses of the helicopter subjected to reserve energy drop test.

Parameter	Baseline design	Optimum meta-model	Optimum FE model
SEA, J/kg	702.0	943.0	948.0
Crosstube mass, kg	9.06	6.84	6.84
Peak displacement, mm	257.0	350.0	341.0
Peak load factor, g's	2.68	2.12	2.20

Similar to the helicopter equipped with the original SLG system, the charts of the three drop test governing parameters, i.e. sink rate, effective mass, and C.G. displacement, are produced for the optimum SLG, as presented in Figures 3.7 and 3.8 for limit load and reserve energy drop tests, respectively. It is observed that the feasible ranges of sink rate for the optimum design are narrower than those for the original SLG due to the degradation in the crosstubes stiffness, though the model still meets the crashworthiness requirements. Figure 3.7 shows that when the helicopter impacts the ground at 2.0 m/s with L = 2/3, the deflection increases only by 5 mm above the preset maximum displacement of 350 mm. The result is confirmed by ABAQUS and the effective mass is set equal to 1298 kg. However, impacting at speeds higher than 2.0 m/s would result in undesirable high deflection and lead to complete failure of the aft crosstube due to high von Mises stress, as shown in Figure 3.9. Figure 3.10 shows that maximum von Mises stress of about 640

MPa is developed in the optimum SLG when the helicopter drop impacted against the rigid surface based on the reserve energy drop test condition.

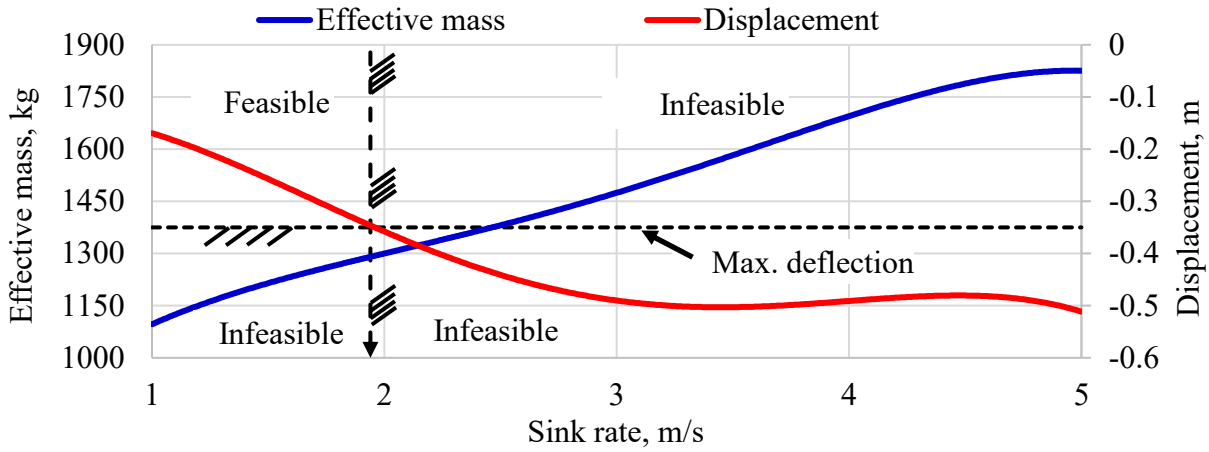

Fig. 3.7. Drop test governing parameters of the optimum SLG at L = 0.67.

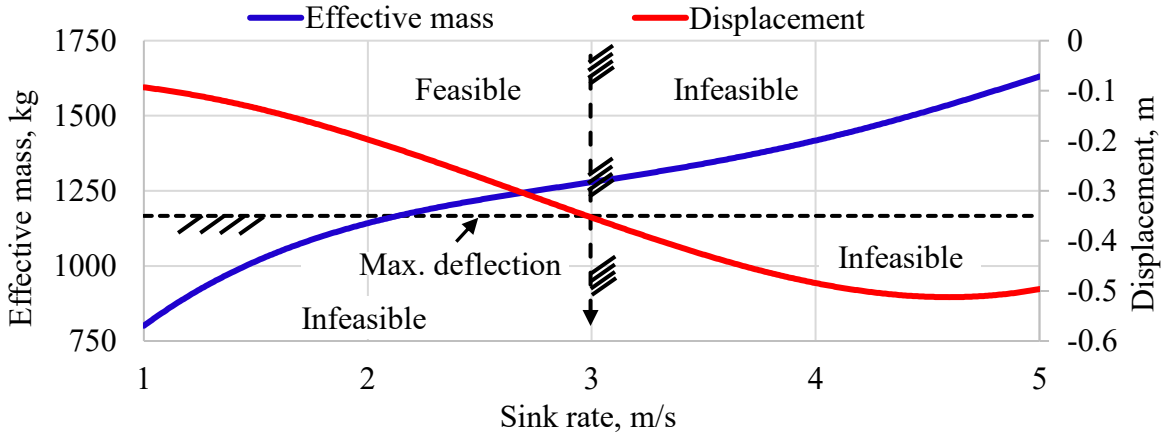

Fig. 3.8. Drop test governing parameters for the optimum SLG at L = 1.0.

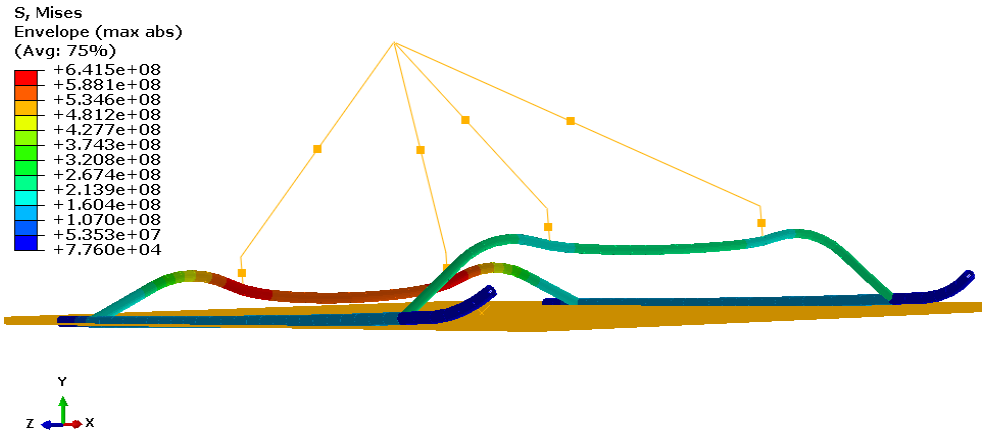

Fig. 3.9. Von Mises stress distribution in the optimum SLG for L = 0.67.

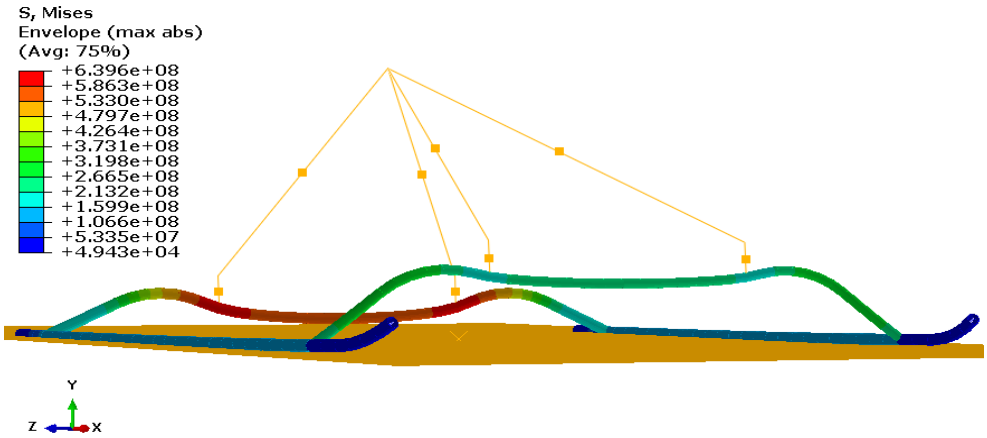

Fig. 3.10. Von Mises stress distribution in the optimum SLG for L = 1.0.

In regard to PEEQ and for the reserve drop test, moderate increase is noticed from 0.035 for the baseline design (Figure 2.21) to 0.052 for the optimum SLG, as predicted in Figure 3.11. This represents 48.6% increase in PEEQ and means that more energy could be dissipated through by utilization almost the entire impact stroke compared to the baseline SLG. Nevertheless, according to the maximum PEEQ failure criterion, there is sufficient margin of safety of about 45%. According to the maximum PEEQ failure criterion, this means that the complete failure is far from occurring and the SLG is still intact.

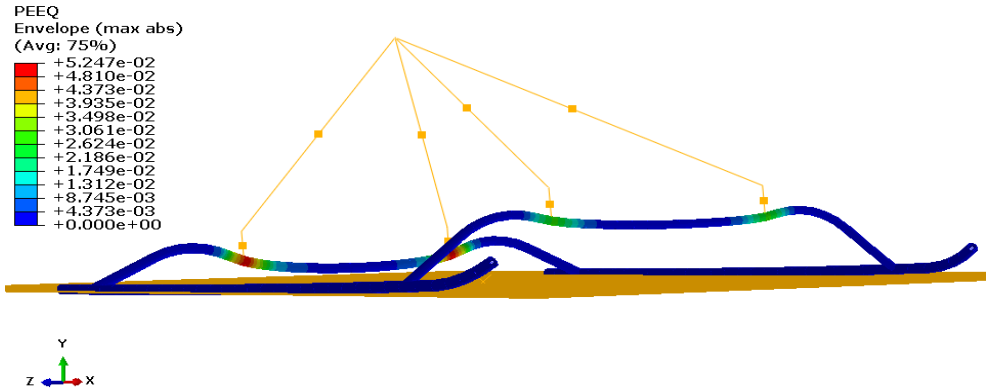

Fig. 3.11. PEEQ distribution in the optimum SLG for L = 0.67.

The objectives of design optimization of the SLG are fulfilled as compared with baseline configuration, the SEA increases by 34% from 702 J to 943 J while the mass of the SLG decreases by 24.5% and subsequently the load factor reduces 18%. The reduction in the SLG mass is beneficial from the airworthiness perspective. Although the optimum SLG increases the SEA, it

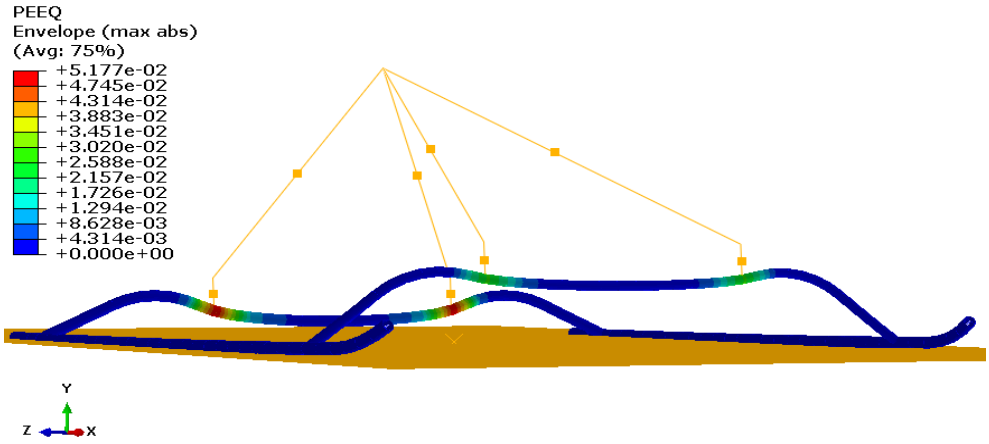

Fig. 3.12. PEEQ distribution in the optimum SLG for L = 1.0.

cannot sustain any excessive load which may incur during higher velocity impacts. Therefore, externally energy absorption devices are required to protect the occupants in these events and to extend the life of the conventional SLG as well. The later is achieved by limiting the stroke of the impact.

The bilinear force-displacement curve of the optimized SLG is obtained by conducting a static test using ABAQUS, similar to the original design. The curve is shown in Figure 3.13. The relation between the nonlinear force and deflection is extracted using curve fitting method as

$$F = 691093 \times \delta^3 - 663521 \times \delta^2 + 229377 \times \delta \qquad (3.30)$$

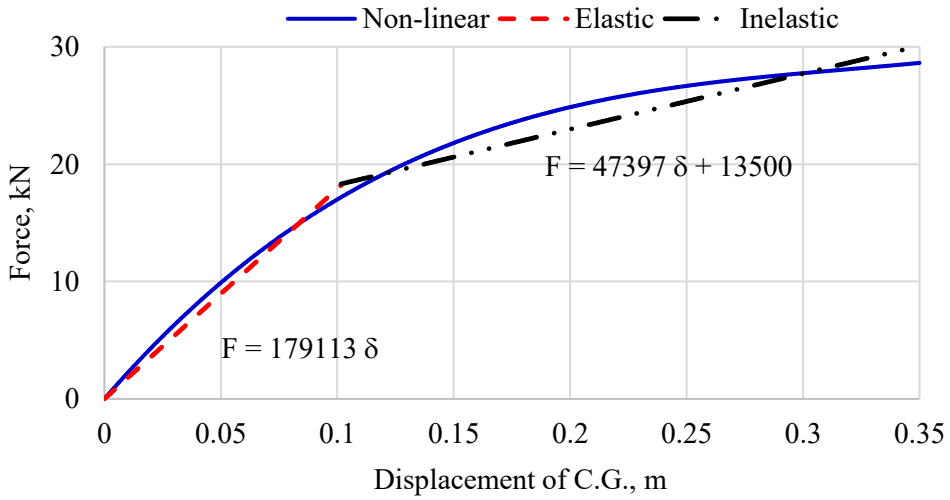

Fig. 3.13. Bi-linear force-displacement curve of optimum SLG.

By comparing Eqs. (2.18) and (3.30), one can observe that there is a considerable reduction in the elastic and inelastic stiffness of the optimized SLG. The significant reduction in stiffness has positive influence on the energy absorption capacity of the crosstubes by allowing utilization of the almost total impact stroke (97.4%). Table 3.4 compares the stiffness of both SLG configurations.

Table 3.4. Comparison of the baseline and optimum SLG stiffness.

SLG configuration	Baseline	Optimum	% Reduction
Elastic stiffness (k_e), N/m	261891	179113	31.6
Inelastic stiffness (k_i), N/m	63885	47397	25.8

3.10 Summary

In this chapter, the size (radius and the thickness) of the forward and aft crosstubes are optimized to increase their energy absorption capacity per kilogram mass. To avoid inevitable computation burden associated with full FE model, the mathematical-statistical methods based on the RSM and DoE are implemented to generate an approximate response functions that can emulate the behavior of the FE model under the impact conditions prescribed in reserve energy drop testing procedure for civil helicopters. The FE model of the optimum SLG was simulated using ABAQUS to verify the results of the meta-models. It is found that there is an excellent agreement between the results of the surrogate and the FE model. The comparison of the optimum and baseline SLG designs in terms of SEA reveals a substantial improvement in the energy absorption in favor of the optimum design with no violation of the constraints imposed on the mass, maximum C.G. deflection, and maximum acceleration. Though the energy absorption capability of the SLG was significantly increased, crashes at velocities greater than those in the limit load and reserve energy drop tests would certainly result in a drastic failure of both SLG configurations. Thereupon, in the next chapters, a bi-fold magnetorheological damper will be designed, optimized, and incorporated in the SLG system to dissipate the impact energy at higher sink rates.

CHAPTER 4

Design Optimization of the Bi-Fold MREA

4.1 Introduction

This chapter addresses the design optimization of a bi-fold MREA to increase its dynamic range (D). It starts with an introductory section on the magnetorheological fluids (MRFs). In this section, the topics related to the fluid properties, modes of operation, the mathematical models of the MR devices, and the analysis of the magnetic circuit are briefly discussed. The advantages of using the bi-fold magnetorheological energy absorber (MREA) in high speed applications over the single-flow path MR devices are highlighted. Then, the analytical fluidic and magnetic relations for describing the behavior of the bi-fold MREAs are derived. The derived formulas are then used to formulate an optimize optimization problem to maximize the dynamic range of the MR damper. Genetic algorithm and sequential quadratic programming methodologies are used to obtain the global solution of the optimization problem while assuring that the problem constraints are respected. In the following step, the analytical approach of analyzing the magnetic circuit is verified with the open source finite element magnetic method code "FEMM". At the end, the controllable damping force equation is expressed in terms of the applied current to facilitate the development of semi-active control system as well as to develop a single degree of freedom helicopter model that mimic the behavior of the rotorcraft model in chapter five.

4.2 Magnetorheological devices

MR damper is a kind of smart devices that is capable of continuously modifying its damping properties by adjusting the applied magnetic field in accordance to a control scheme. MR dampers have proven their successfulness in the mitigation of vibration loads in a broad range of applications such as biomedical, automotive, aeronautical, ship, and agricultural industries. Different configurations of MR damper are available in the market to fit the requirements of various applications. These devices are reviewed in Chapter 1, section 1.3.3 for their specific use in landing gears in the event of high impact. In the subsequent sections a brief explanation on the MR fluids properties, mode of operations, models, and the magnetic circuit design will be provided.

4.2.1 MR fluids

The initial discovery and development of magnetorheological fluid (MRF) can be credited to Jacob Rabinow in the late 1940s [19]. The ferromagnetic fine particles and the carrier (base) fluid are the main constituents of the MRF. The soft ferromagnetic particles are mainly made of iron (carbonyl iron due to its high magnetic saturation limit) with a typical size ranging from one to 10 micrometers in diameter [56, 57]. In the absence of magnetic field, the particles disperse randomly in the carrier fluid and the MRF behaves like a Newtonian fluid in the MR gap. In this case, the generation of the damping force is dominated by the linear proportion of the shear stress with respect to the shear strain rate. The stress-strain constitutive relationship can be expressed as [19]

$$\tau = \eta \dot{\gamma} \tag{4.1}$$

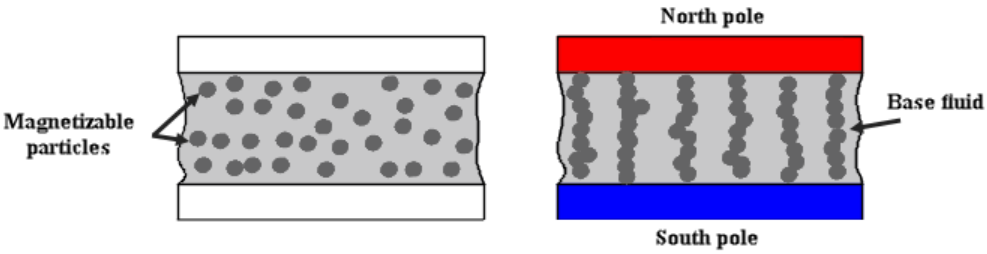

a) Field-off b) Field-on

Fig. 4.1. Phenomenological behavior of the MR fluid.

where τ is the shear stress, η is the fluid viscosity independent of the magnetic field, and $\dot{\gamma}$ is the shear strain rate. Within only a few milliseconds of setting up the external magnetic field to on-state, the magnetic particles stack together to form a chain-like structure along the lines of the magnetic flux. This non-Newtonian fluid state restricts the flow of the fluid and results in an increase in the shear stress. Therefore, Eq. (4.1) can be modified to accommodate the change in the shear stress as [19]:

$$\tau = \tau_y + \eta \dot{\gamma} \tag{4.2}$$

here τ_y is the field dependents yield shear stress generated by the application of the magnetic field. Since the MR effect is reversible, the fluid returns to its free flow condition upon removing the magnetic field. MRFs are characterized by their high dynamic range, low power requirement, fast

time response, wide working temperature range, and insensitivity to contaminants. The typical properties of commercial MRFs are provided in Table 4.1 [57-59].

Table 4.1. Typical properties of commercial MR fluids.

Property	Range	Unit
Density	2000 to 4000	kg/m^3
Field-independent viscosity	0.05 to 0.3	Pa.s
Yield stress at 100 kA/m	10 to 55	kPa
Yield stress at 200 kA/m	20 to 80	kPa
Yield stress at saturation	25 to 100	kPa
Temperature range	-40 to 150	°C
Response time	< 0.001	Seconds
Power supply	2 to 25	Volt
Relative magnetic permeability at low field	3.5 to 10	--
Stability	Unaffected by most impurities	

4.2.2 MR modes

The MR modes can be classified into three types depending on the fluid flow [19, 57], namely, flow (valve) mode, direct shear mode, and squeeze mode, as illustrated in Figure 4.2. The flow mode is usually used to develop the controllable damping force in linear dampers. In this mode, the pressurized MRF flows between two stationary plates or concentric cylinders and the direction of the magnetic field is perpendicular to the motion of the fluid inside the gap. In low velocity vibrations, the pressure drop consists of viscous and magnetic field dependent components. However, in high speed impacts, the minor losses have a substantial contribution to the field-off damping force and thus cannot be ignored [24, 26, 29].

The shear mode is common mode in the rotary MR dampers such as the brakes and clutches. Here, the damping force is generated as a result of the resistance to the rotational motion. The direction of the magnetic field is perpendicular to the plate or disc thickness, i.e. or direction of MR fluid flow. In this mode, either one plate is moving or both are moving against each other causing the MRF to shear. The squeeze mode is used in linear MR dampers when high damping

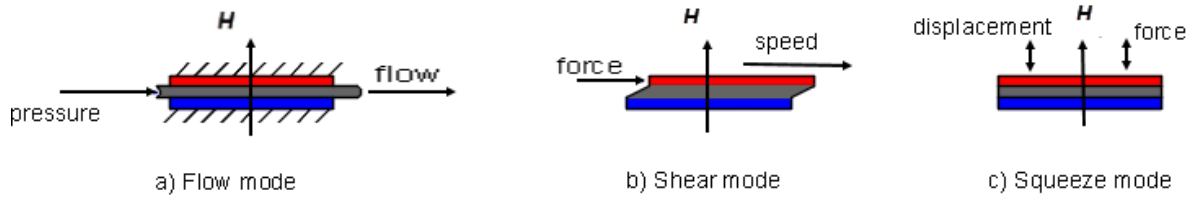

Fig. 4.2. Operational modes of the MR fluid.

force is required for small-amplitude vibrations. In this mode, the direction of the magnetic field is parallel to the relative motion of the plate.

4.2.3 MR models

In order to develop practical MR devices, the nonlinear behavior of the MRF in the pre- and post-yield regions should be accurately predicted. Several mathematical models have been developed to simulate the behavior of the MR device under the influence of external excitations in a broad velocity range. The next sub-sections briefly describe these models.

4.2.3.1 Bingham plastic model

The Bingham plastic (BP) model is considered as the simplest mathematical model that characterizes the flow of MR fluid. This model assumes that the MRF is behaving like a rigid body in the pre-yield zone, as shown in Figure 4.3. However, the behavior is turned to Newtonian-like one with a constant viscosity when the shear stress of the flowing MRF becomes equal to or exceeds the yield stress of the MRF, as shown in Figure 4.3. The analytical expression can be expressed as [19]:

$$\tau = \begin{cases} \tau_y(H)\, sgn(\dot{\gamma}) + \eta\, \dot{\gamma} & \tau \geq \tau_y \\ 0 & \tau < \tau_y \end{cases} \tag{4.3}$$

where H represents the applied magnetic field strength.

4.2.3.2 Bingham plastic model with minor loss factors

Wereley et al. [23-26, 29] recognized that the BP model is accurate when the vibrations are induced by low piston velocities (< 1.0 m/s). However, at higher piston velocities, which are predominant at shocks and impacts, the BP model shows poor performance in the estimation of

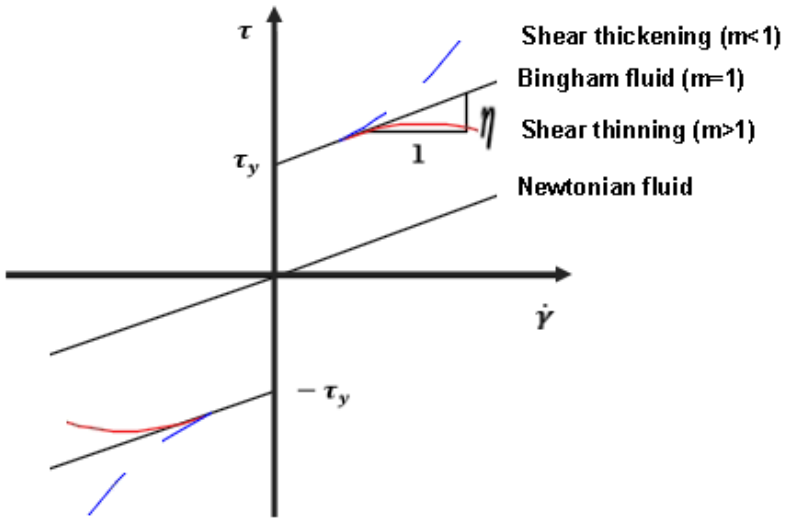

Fig. 4.3. Visco-plastic models of the MR fluid.

the MR damper behavior. The reason is due to the fact that the standard BP model does not take into account contribution of the off-state pressure drop due to minor loss factors. The minor loss factors are semi-empirical coefficients that take into account the pressure drop due to the entrance, exit, sudden expansion, sudden contraction and bends inside the MR gap, etc. These losses are taken into consideration by introducing the relevant factors in the pressure drop formulation of the BP model. The modified model is known as the Bingham plastic model with minor losses or simply "BPM" model. For BPM model, the damping force can be calculated using [23] as

$$F = (\Delta P_{\eta} + \Delta P_{ml})\, A_p + \Delta P_{\tau} A_p\, sgn(V_p) \tag{4.4}$$

where ΔP_{η} is the pressure drop due to the fluid viscous effect, ΔP_{ml} is the pressure drop due to the minor loss factors, ΔP_{τ} represents the pressure drop due to the MR effect, and A_p is the effective area of the piston.

4.2.3.3 Biviscous model

The biviscous model is the generalized form of the standard BP analytical model and is used where the behavior of the fluid in the pre-yield region is assumed to be linear viscoelastic. The stress-strain constitutive relationship for viscous model can be expressed as [19]

$$\tau = \begin{cases} \tau_y(H) + \eta\, \dot{\gamma} & |\tau| \geq \tau_y \\ \eta_e\, \dot{\gamma} & |\tau| < \tau_y \end{cases} \tag{4.5}$$

where, η_e is referred to the elastic viscosity of the fluid.

4.2.3.4 Herschel-Bulkley model

The assumption of constant post-yield viscosity in the BP model may not address the real behavior of the MRF under high shear strain rates. Under high shear strain rates, the MRF exhibits either shear thickening or shear thinning effect. Such behaviors are accommodated by Herschel-Bulkley visco-plastic model, as illustrated in Figure 4.3. The mathematical model of the Herschel-Bulkley model can be expressed as [19]

$$\tau = (\tau_y(H) + K\,|\dot{\gamma}|^{\frac{1}{m}})\, sgn(\dot{\gamma}) \tag{4.6}$$

here K and m denote the fluid coefficients. The shear thickening (m<1) and shear thinning (m > 1) are attributed to the resepective increase and decrease in the MRF's apparent viscosity[60].

4.2.4 Magnetic circuit analysis

The exposure of the MR fluid flowing in the annular gap to a magnetic field increases the yield stress of the MRF. The magnitude of the yield stress does not depend only on the strength of the field but also on the properties of the magnetizable material particles. In the post-yield region, the yield stress increases nonlinearly with the increase in the applied magnetic field due to the magnet-like behavior of the particles in the MR fluid valve [61]. In this case, the particles form chains along the direction of the magnetic flux lines and obstruct the flow. Therefore, the careful analysis of the magnetic circuit is very crucial in the design of the MR damper as it serves two purposes: a) to ensure that the maximum magnetic field intensity is applied to MRF in the gap so that the performance of the device is maximized; b) to avoid magnetic lockoff in the bobbin by assuring that the MR fluid in the valve saturates before the remaining links of the magnetic circuit. Conventionally, the magnetic circuit is analyzed first using the theoritical approach which assumes a linear relationship between the magnetic flux density, B, and the magnetic field intensity, H. In the subsequent step, the solution can verified using FE method [62] to confirm the analytical analysis results. According to the Kirchoff law, the magnetomotive force of a magnetic circuit can be expressed as

$$N\,I = \sum H_j l_j\,; \qquad j = 1, 2, \ldots, n \tag{4.7}$$

where N is the number of wire turns per coil, I is the current passing through the coil, H is the magnetic field intensity, l is the link length, and n is the total number of links in the circuit. The magnetic flux ($\emptyset$) passing through the cross sectional areas of the links is the same, thus

$$\emptyset = B_\tau A_\tau = B_j A_j \; ; \quad j = 1, 2, \dots, n \tag{4.8}$$

where B_τ denotes the magnetic flux density in the MR fluid in the gap, B_j is the magnetic density of the j-th link of the magnetized metallic material, and A_τ and A_j are the areas normal to the path of the magnetic field lines of the MR valve and the j-th linkage, respectively. Let μ denotes the permeability of the magnetic linkage, then the magnetic flux density can be expressed in terms of magnetic field intensity as

$$B = \mu H \tag{4.9}$$

4.3 Genetic algorithm method

Genetic Algorithm (GA) is a stochastic evolutionary based numerical algorithm inspired by the process of natural selection. The algorithm requires only function evaluation without requiring gradient information and has been demonstrated to be very effective in finding near global optimum solution in various discrete and continuous optimization problems. The important features of GA are their randomness, robustness, and the initial population of design variables (rather single initial point). The shortcoming of the GA techniques is that the global optimum solution cannot be guaranteed. Rather, an acceptable good solution can be achieved. The second disadvantage is that enormous amount of calculations is required to reach the optimum solution. Briefly, the elements of GA optimization can be described as

1- Selection: Random selection of the initial design variables for reproduction with probability depending on the relative fitness of these variables.
2- Reproduction: New generation of design variables is created from those which have successfully passed the above selection process. The newly generated design variables are hopefully able to produce fitter points.
3- Evaluation: Evaluate the fitness of the newly generated variables.
4- Replacement: In this step, the old population of design points are omitted and replaced by the new ones.

Over the successive generations, the optimization terminates when the population converges toward or near the optimum solution. High fitness function or the objective function implies a better solution. The fitness function may be described as [55]

$$F = (1 + \varepsilon) f_{max} - f_i \tag{4.10}$$

where f_i is the individual cost function, f_{max} is the value of the highest performing individual, and ε is a scaling factor of small value to terminate the algorithm and prevent endless run of the program. The stopping criteria of GA can either be based on the number of iterations or the returned best value of the objective function.

In the present chapter, the design optimization study of the MREA is performed in two stages. First, using GA, the near global optimum solutions is obtained. Second, using optimal solution from GA as initial design point for the SQP, the true global optimum solution is captured. This combined GA and SQP approaches and ensures catching the global optimum solution accurately and reduces the computation time. Here, we call this combined approach as "GA+SQP" technique. The GSA+SQP algorithm has been implemented in MATLAB (R2015b) to solve the optimization problem.

4.4 Configurations of linear MREA

The current research addresses the ways to maximize the energy absorption capabilities of the conventional skid landing gear. In chapters two and three, it was demonstrated that the original and the optimum versions of the conventional SLG have limited energy absorption capacity although they met the requirements of the standarized crashworthiness drop tests for SLGs of civil helicopter. To maximize the energy dissipation at higher sink rates, the reviewed literature on linear MR damper estblished concrete mathematical foundation and presented diverse applications of the single-flow path MR damper including those used in the landing gear systems. However, based on the geometrical, volume, and damping force constraints provided in the present research, the bi-fold MR damper is found the most suitable energy absorbing device that can fulfill the objective of attenuating impact loads at high sink rates within the imposed design constraints. The MR dampers that are mainly used in absorbing energy in high velocity impacts are known as MR Energy Absorbers, or MREAs [24]. When helicopter are equipped with conventional skid gear and MREAs, each MREA is integrated to the rotorcraft at two points. The first point is on the crosstube

and the second one is on the fuselage sub-floor structure, as schematically shown in Figure 4.4. Different configurations of the well-known MREAs have often been quoted in literature as the most successful adaptive MREAs. They can be either of single-flow path [20, 22, 23] or bi-fold type [27-29]. A brief descrption of the both MR devices is given below.

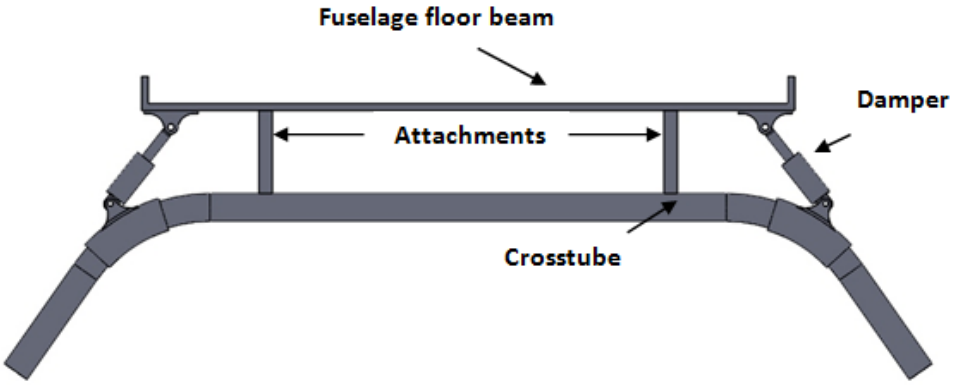

Fig. 4.4. Integration of the MREA into the conventional SLG.

4.4.1 Single-flow path MREA

The single-flow path MREA is known as the conventional or monotube MREA. Its configuration is similar to the conventional passive shock absorber but with added coils housed by the piston head, as shown in Figure 4.5. The single coiled monotube MREA has limited capability of generating the required damping force. Nevertheless, the performance can be enhanced by using extended piston head with multi-coil configuration, as shown in Figure 4.6. However, for helicopter impacting at high speed, the size of the MREA which incorporates the multi-coil configuration may not fit in the allocated space. Therfore, there is need to implement the compacted bi-fold MREA which produces high controllable damping force.

4.4.2 Bi-fold MREA

The schematic drawing of the bi-fold MREA is shown in Figure 4.7. Based on the available space between the crosstubes and the fuselage sub-floor structure it is found that the device can fit properly in the allocated space similar to what is shown in Figure 4.4. The bi-fold MREA is of flow mode type in which the active gaps form the shape of the regular and inverted letter “U”, as shown in Figure 4.7. The device consists of two tubes, the outer tube which serves as a protection shell and the inner tube which forms the bi-fold MR valve geometry between the ends of the tube

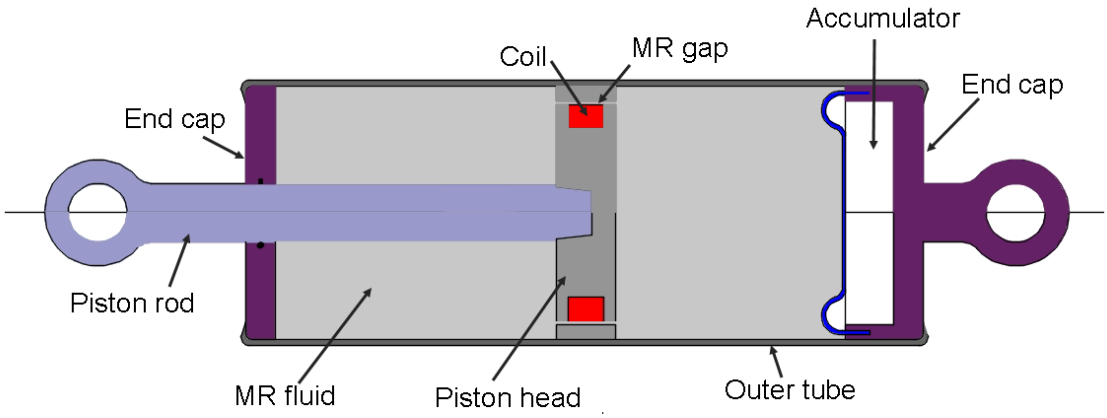

Fig. 4.5. Single-coil Monotube MREA.

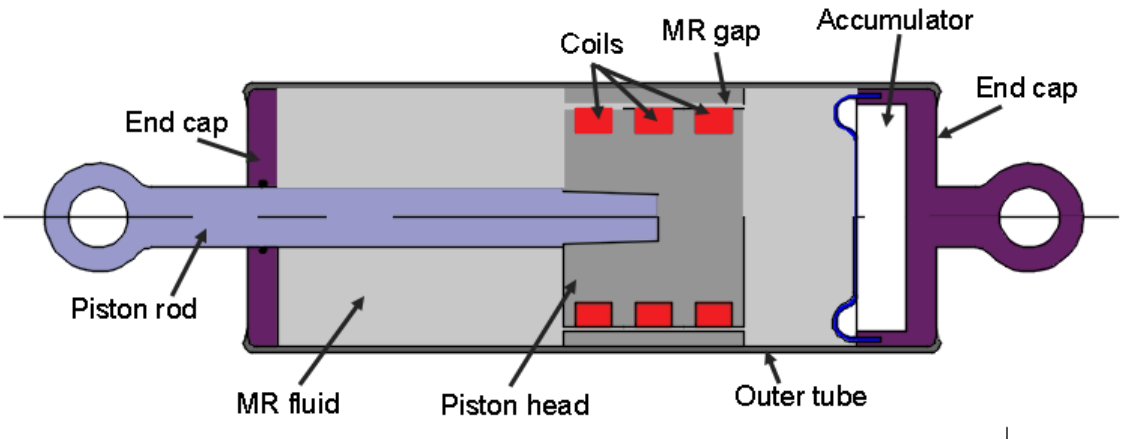

Fig. 4.6. Multi-coil Monotube MREA.

and the bobbin. In addition, the inner tube serves as a guide to the back and forth motion of the piston. The electromagnetic coils are imbedded in the bobbins next to the bi-fold valve on either side of the damper. Under high velocity impacts (> 1 m/s), the bi-fold MREAs may suffer considerable drop in performance. This is attributed to the substantial increase in the off-state stroking load in proportion to the increase in the non-linear velocity squared of the piston [29]. In high velocity impact, the MREA prompts counteracting impact force by generating and rapidly adjusting the stroking load in very short duration to protect helicopter occupants in the event of impact which may last up to 200 milliseconds [23, 26]. Therefore, caution should be exercised so that the generated stroking load does not exceed the human body tolerance to abrupt acceleration. The human body can tolerate an impact force in the range of 12 to 18 kN based on its strength [26]

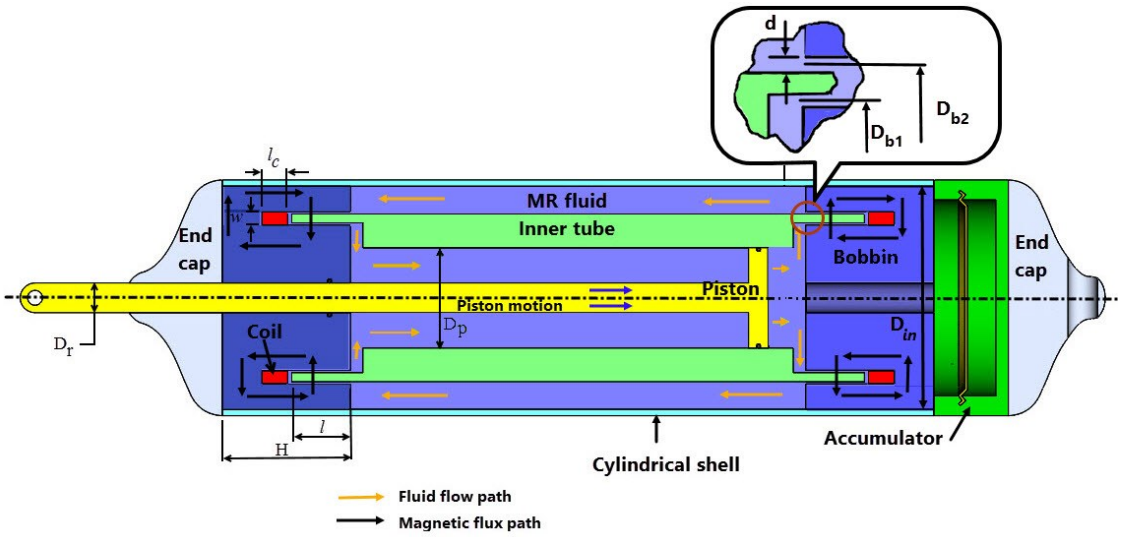

Fig. 4.7. Schematic of the bi-fold MREA.

In high velocity impact loading, the flow inside the MR valve, which is characterized by Reynolds number, may no longer be laminar if the MR valve is small. In this case, it may fall in the transition or turbulent regime when Reynolds number exceeds 2000 [25]. Thus, generates high off-state damping force under the influence of the velocity squared pressure drop, which in turn, reduces the performance of the MREA device [26]. Another factor contributes to the reduction in the MREA device performance in high speed impacts is the pressure losses due to the changes in geometry at the entrance to, exit from and within the MR valve length. These losses are collectively known as the minor loss factors and cannot be neglected at higher piston speed [29]. As the field-off damping force increases with the increase in impact speed, the controllability of the MREA drops significantly until it diminishes at D ≈ 1. On the other hand, maintaining laminar flow inside the MR valve requires having larger MR valve thickness. However, this adversely affects device controllability which requires smaller gap thicknesses since larger thickness weakens the intensity of the magnetic flux in the MR valve. Therefore, the thickness of the MR valve should be optimized to achieve maximum dynamic range. To accurately capture the behavior of the bi-fold MREA in impact event, the Bingham plastic model with minor loss coefficients (BPM) is used in this research to formulate the design optimization problem.

4.5 Formulations of the Bingham plastic model with minor losses (BPM)

As demonstrated above, the analytical BPM model is more accurate than the standard BP model in describing the behavior of the MREAs in high piston speeds. Therefore, it will be utilized in the optimization and evaluation of the device performance. During the impact and because of the rapid motion of the piston, the flow of the MR fluid inside the MR valve results into three components of damping force, namely, the viscous pressure drop (Darcy friction), minor losses, and the controllable pressure drop under the actuation of magnetic field. Among the above components, the minor losses are calculated using semi-empirical relations in [29]. The damping force in the BPM model is expressed as

$$F = (\Delta P_\eta + \Delta P_{ml})\, A_p + \left(\Delta P_\tau A_p + F_f\right) sgn(V_p) \tag{4.11}$$

where the Darcy friction (viscous) pressure drop is given by

$$\Delta P_\eta = f \frac{\rho L V_d^2}{2 D_h} \tag{4.12}$$

here the hydraulic diameter $D_h = 2\ d$, and d is the MR valve thickness. The total active length of the annular MR gaps (L) is equal to $4l$ (Figure 4.8), and the Darcy friction factor (f) is a piecewise function of Reynolds number, Re, of the flow in the MR gap, d, and the surface roughness, ε, of the MR valve [29]. For laminar flow, f is calculated using

$$f = \frac{96}{Re} \quad , \quad \text{Re} \le 2000 \tag{4.13}$$

for transition flow

$$f = (1-\alpha)\,\frac{96}{2000} + \alpha\, \frac{1}{\left\{1.8\, log_{10}\left[\left(\frac{\varepsilon/D_h}{3.7}\right)^{1.11} + \frac{6.9}{4000}\right]\right\}^2} \quad , \quad 2000 < \text{Re} \le 4000 \tag{4.14}$$

and for turbulent flow condition

$$\frac{1}{f^{1/2}} \approx 1.8\, log_{10}\left[\left(\frac{\varepsilon/D_h}{3.7}\right)^{1.11} + \frac{6.9}{Re}\right] \quad , \quad \text{Re} > 4000 \tag{4.15}$$

where

$$Re = \frac{2\,\rho\, d\, V_d}{\eta} \text{ and } \quad \alpha = \frac{Re - 2000}{4000 - 2000} \tag{4.16}$$

The total pressure drop from minor losses is given by

$$\Delta P_{ml} = \rho \sum K_{ml\_i} \frac{V_d^2}{2} \tag{4.17}$$

The pressure drop due to MR yield stress is expressed as

$$\Delta P_{\tau} = \frac{4L\tau_y}{D_h} \tag{4.18}$$

and the signum function is defined as

$$sgn(V_p) = \begin{cases} 1 & for\ V_p > 0 \\ 0 & for\ V_p = 0 \\ -1 & for\ V_p < 0 \end{cases} \tag{4.19}$$

Applying the continuity equation between the flow in the inner tube bore and the flow inside the bi-fold MR valve, the velocity of the fluid flowing in the valve (V_d) can be written as

$$V_d = \frac{A_p}{A_d} V_p \tag{4.20}$$

where

$$A_p = \frac{\pi}{4}(D_p^2 - D_r^2) \tag{4.21}$$

and

$$A_d = \pi D_b d \tag{4.22}$$

To calculate the effective area of MR valve, the bi-fold valve is transformed to a mathematically equivalent conventional MR single-flow valve, as shown in Figure 4.8. Then, the effective valve diameter can be computed as [27]

$$D_b = \frac{2D_{b1}D_{b2}}{D_{b1} + D_{b2}} \tag{4.23}$$

The friction force, F_f, is usually produced from the contact between the seals in the piston rod and the piston head with the bobbin and the inner tube, respectively. In the preliminary design stage, however, these friction forces can be neglected. Therefore, expression (4.11) can now be separated to the following off-field and yield force components

$$F_{off} = (\Delta P_{\eta} + \Delta P_{ml})\, A_p \tag{4.24}$$

and the MR yield force can be expressed as:

$$F_{\tau} = \Delta P_{\tau}\ A_p \tag{4.25}$$

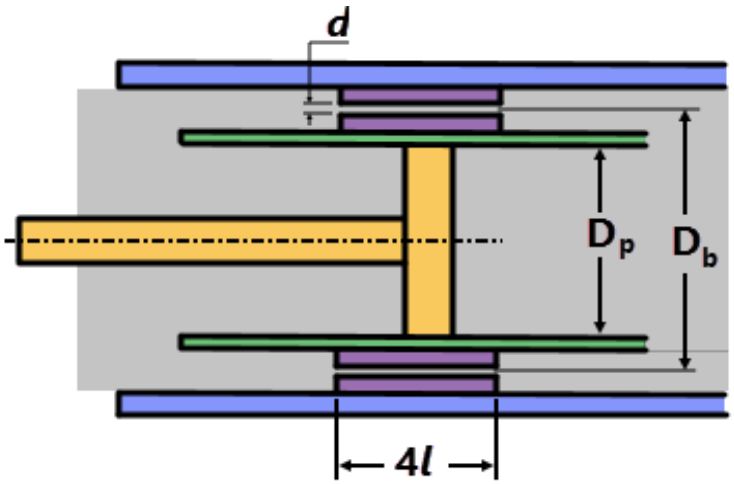

Fig. 4.8. Equivalent Single-flow path MREA [27].

Adding Eqs. (4.25) to (4.24) yields the field-on damping force (F_{on}) as

$$F_{on} = (\Delta P_{\eta} + \Delta P_{ml} + \Delta P_{\tau})\ A_p \tag{4.26}$$

The dynamic range (D) is expressed as the ratio of the field-on force at maximum applied current to the field-off force. Thus,

$$D = \frac{F_{on}}{F_{off}} \tag{4.27}$$

The accurate prediction of the damping force in the high velocity impact events requires considering the minor loss factors [25, 26, 29]. The regions of such losses are shown on a quarter MREA in Figure 4.9. Based on Refs. [63] and [64], the coefficients of the minor losses are assumed as

$K_{entrance} = 0.1$, $K_{exit} = 0.6$, and $K_{bend} = 0.18$

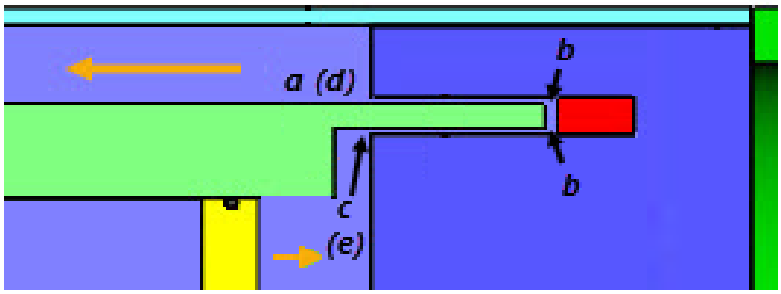

Fig. 4.9. Coefficients of minor losses: (a): Exit, (b): Bend, and (c): Entrance, on the other side: (d): Entrance, and (e): Exit. (piston moving to the right).

4.6 Magnetic circuit analysis of the bi-fold MREA

Using expression (4.7), the magnetomotive force of the magnetic circuit shown in Figure 4.10 can be calculated as

$$N\,I = H_1 l_1 + H_2 l_2 + H_3 l_3 + H_4 l_4 + H_5 l_5 + H_6 l_6 + 2\,d\,H_\tau \tag{4.28}$$

Substituting expression (4.9) into (4.28) yields

$$N\,I = \frac{B_1 l_1}{\mu_s} + \frac{B_2 l_2}{\mu_s} + \frac{B_3 l_3}{\mu_s} + \frac{B_4 l_4}{\mu_s} + \frac{B_5 l_5}{\mu_s} + \frac{B_6 l_6}{\mu_s} + 2\,\mathrm{d}\frac{B_\tau}{\mu_\tau} \tag{4.29}$$

The substitution of (4.8) into (4.29) gives

$$N\,I = \frac{B_\tau A_\tau l_1}{\mu_s A_1} + \frac{B_\tau A_\tau l_2}{\mu_s A_2} + \frac{B_\tau A_\tau l_3}{\mu_s A_3} + \frac{B_\tau A_\tau l_4}{\mu_s A_4} + \frac{B_\tau A_\tau l_5}{\mu_s A_5} + \frac{B_\tau A_\tau l_6}{\mu_s A_6} + 2\,\mathrm{d}\frac{B_\tau}{\mu_\tau} \tag{4.30}$$

Equation (4.30) can be rearranged to obtain

$$N\,I = B_\tau\,[2\frac{d}{\mu_\tau} + A_\tau(\frac{l_1}{\mu_s A_1} + \frac{l_2}{\mu_s A_2} + \frac{l_3}{\mu_s A_3} + \frac{l_4}{\mu_s A_4} + \frac{l_5}{\mu_s A_5} + \frac{l_6}{\mu_s A_6})] \tag{4.31}$$

Using Eq. (4.31), B_τ is computed as

$$B_\tau = \frac{N\,I}{\frac{2d}{\mu_\tau} + A_\tau R_t} \tag{4.32}$$

where R_t is the total reluctance of the bobbin links expressed as:

$$R_t = \sum_{1}^{6} \frac{l_j}{\mu_s A_j} \tag{4.33}$$

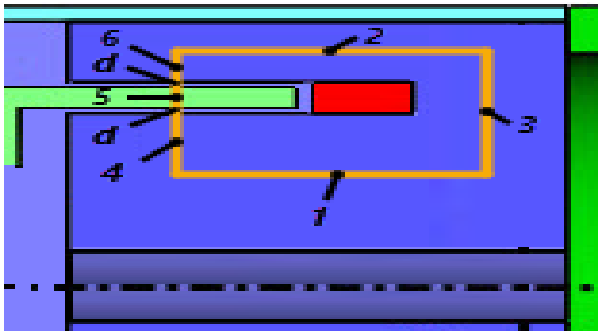

Fig. 4.10. Magnetic circuit of the bi-fold MREA.

For the magnetic circuit in Figure 4.10, the reluctances of different links are summarized in Table 4.2. To numerically confirm and validate the results of the analytical approach, an open finite element magnetic method (FEMM) software is used to solve the electromagnetic problems. The active region of the MREA and the surrounding bobbin are modeled in FEMM. Here, the axisymmetric domain is meshed automatically using triangular elements, and the magnetic flux density is calculated in the active MR gap and the bobbin.

In order to calculate the MR yield force, the field-dependent yield stress (τ_y) is expressed in terms of the magnetic flux density of the MR fluid. The commercial MR fluid type MRF-132DG from Lord Corporation [65] is used in the current study to generate the required damping force. The function of the induced yield stress as a function of the applied magnetic field intensity is adopted from Ref. [66]. The relation between the induced yield strength and applied magnetic field intensity is shown in Figure 4.11. The function of τ_y in terms of B_τ is expressed in kPa as

$$\tau_y = 52.962\, B_\tau^4 - 176.51\, B_\tau^3 + 158.79\, B_\tau^2 + 13.708\, B_\tau + 0.1442 \tag{4.34}$$

Table 4.2. Parameters of the bi-fold MREA's magnetic circuit.

Link	Length (l_j)	Area (A_j)	Reluctance
1	$0.5(l + l_3) + l_c$	$\frac{\pi}{4}(D_i^2 - D_r^2)$	$R_1 = \frac{l_1}{\mu_s A_1}$
2	$0.5(l + l_3) + l_c$	$\frac{\pi}{4}(D_{in}^2 - D_o^2)$	$R_2 = \frac{l_2}{\mu_s A_2}$
3	$\frac{D_{in} + D_o - D_i - D_r}{4}$	$\frac{\pi(D_{in} + D_o + D_i + D_r)l_3}{4}$	$R_3 = \frac{l_3}{\mu_s A_3}$
4	$\frac{D_i - D_r}{4}$	$\frac{\pi(3D_i + D_r)l}{4}$	$R_4 = \frac{l_4}{\mu_s A_4}$
5	*w-2d*	$\frac{\pi(D_i + w)l}{4}$	$R_5 = \frac{l_5}{\mu_s A_5}$
6	$\frac{D_{in} - D_o}{4}$	$\frac{\pi(D_{in} + 3D_o)l}{4}$	$R_6 = \frac{l_6}{\mu_s A_6}$

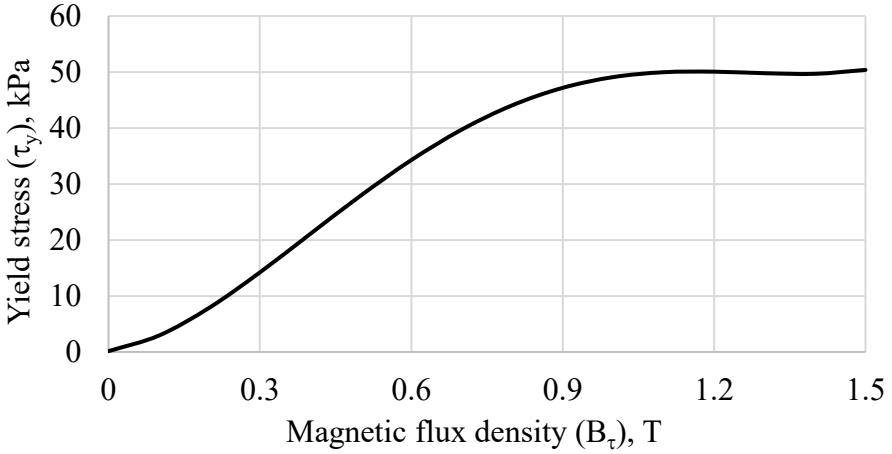

Fig. 4.11. Yield stress curve of MRF-132DG [66].

4.7 Design optimization of the bi-fold MREA

To ensure that the bi-fold MREA can generate the required damping force, its dynamic range (D), which equals to the field-on force generated at maximum input current divided by the field-off force, should be adequately high to assure gaining good controllability over a broader range of sink rates. In the present design optimization study, the objective is to maintain dynamic range around 2 at impact velocity 5 m/s. The problem is solved using combined GA and SQP algorithms.

4.7.1 Design variables

The design parameters for the bi-fold MREA are shown in Figure 4.12. Six design variables are selected for the design optimization study. These variables and their lower and upper bounds are given in Table 4.3. In the Table design variables γ and β are calculated from

$$\gamma = \frac{B_{s,sat}A_1}{B_{\tau,sat}A_\tau} \tag{4.35}$$

$$\beta = \frac{D_i}{D_p} \tag{4.36}$$

Factor γ is defined as the ratio of flux in the bobbin core to the flux in the MR gap both at their saturation state, while factor β is the ratio of the external diameter of bobbin core to the diameter of the piston head. Tight bounds on β are set to reduce the expansion of lateral dimension of the MREA which may violate the volume constraints. The values of other input parameters are

tabulated in Table 4.4. B-H curve of the bobbin material (alloy steel 1006) is plotted in Figure 4.13 [67]. The low and upper bounds of the MR gap are 0.5 and 2.0 mm, as per Ref. [68].

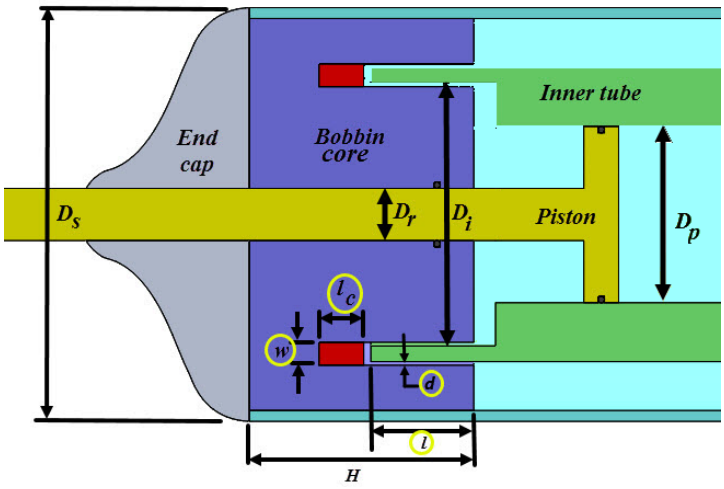

Fig. 4.12. The bi-fold MREA demonstrating related design parameters.

Table 4.3. The upper and lower bounds of design variables.

Variable	Description	Bounds
$x_1 = d$	MR valve	0.5-2.0 mm
$x_2 = w$	Coil width	3.5-8.0 mm
$x_3 = l$	Active length of MR valve	8.0-35.0 mm
$x_4 = l_c$	Coil length	5.0-20.0 mm
$x_5 = \gamma$	Scale factor	1.02-1.07
$x_6 = \beta$	Scale factor	1.43-1.45

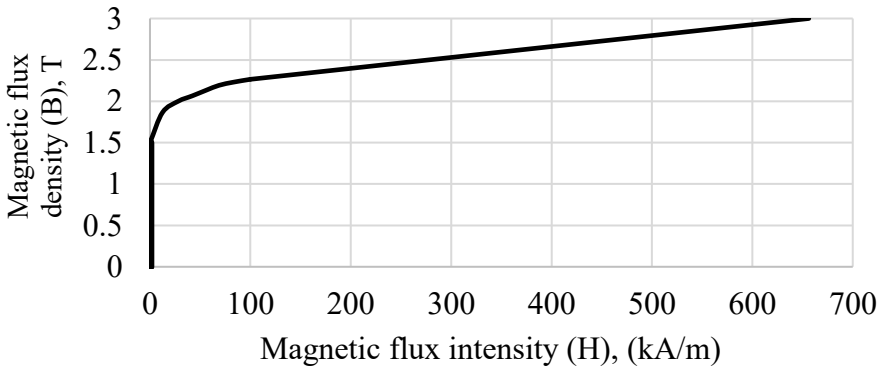

Fig. 4.13. B-H curve for Steel 1006 [67].

Table 4.4. Required input parameters of the MREA.

Parameter	Value	Unit
Average MR fluid density	3050	Kg/m^3
MR fluid viscosity	0.112	Pa-s
Relative permeability of MR fluid	6.0	–
Relative permeability of steel 1006	1404	–
Saturation flux density of MR fluid ($B_{\tau,sat}$)	1.6	Tesla
Saturation flux density of Steel 1006 ($B_{s,sat}$)	3.0	Tesla
Maximum permissible MR yield stress (τ_y)	48.0	kPa
Piston rod diameter (D_r)	12.0	*mm*
Maximum permissible bobbin diameter (D_{in})	95.0	*mm*
Design impact velocity (V_p)	5.0	*m/s*
Input current (I)	3.0	Amperes

4.7.2 Design constraints

The constraints on the bi-fold MREA are related to geometrical, field-off stroking load, and magnetic circuit. These constraints will be described briefly in the following sections.

4.7.2.1 Constraints on the geometrical parameters

The bi-fold MREA will be integrated within the candidate baseline/optimum conventional SLG system in the manner represented in Figure 4.4. Therefore, the MREA with its exterior dimensions (diameter and full extendable length) should be constrained to fit in the designated space. Moreover, the variation in the thickness of the MR active annular channels (d) has significant impact on the flow type and on the production of the damping force as explained in section 4.4.2. In addition, β is an important design variable in the maximization of the generated yield force simultaneously with the minimization of the diameter of piston guiding part of the inner tube. Thus, β effects the generated amount of damping force because it has direct relation to the cross sectional area of the cylinder inner bore, A_p, as Eq. (4.11) depicts. Another constraint is set on the volume of the bobbin to limit its expansion along the device's longitudinal axis.

4.7.2.2 Constraints on the field-off damping force

For the bi-fold MREA to be incorporated in a skid landing gear, it should be capable of generating a stroking load of about 15 kN at the peak impact velocity of 5.0 m/s in the filed-off operating mode. This force is corresponding to the average impact load that an occupant/payload can sustain with minimum or no injury and is approximately equivalent to sudden acceleration of 15 g's [1, 26]. At high-end impact speed of 5 m/s, the MREA can generate the required damping force passively (magnetic field-off) due to its squared relationship with the piston velocity [69].

4.7.2.3 Constraints based on the magnetic circuit

The rheology of the fluid is controlled by alternating the magnetic field. The latter is controlled by adjusting the current supply to the electromagnet coils housed by the bobbins. Therefore, it is of paramount importance to analyze the magnetic circuit carefully to ensure that the bobbin's core saturates after the MR fluid in the gap does. However, achieving this objective might result in a relatively massive damper. To satisfy the above condition at minimum bobbin volume, design variable (γ) was introduced. Parameter γ relates the magnetic flux passing through the effective area of the MR link ($B_\tau.A_\tau$) to the magnetic flux through the bobbin's core ($B_1.A_1$) at saturation. In this study, a coil made of copper wire of size 22 AWG is used. The wire diameter measures 0.64262 mm and can transmit current of up to 7 amperes. To avoid overheating the embedded coil, a maximum current limit of 3.0 A is set to pass in the magnetic circuit.

4.8 Formulation of the optimization problem

The optimization problem can now be formally formulated in the standard form as

Find Design Variables X*:

To maximize $D = \frac{F_{on}}{F_{off}}$ (4.37)

Subject to the following inequality constraints:

$$g_1(x) = -F_{off} + 15.0 \leq 0 \quad \text{(kN)} \tag{4.38-a}$$

$$g_2(x) = F_{off} - 15.25 \leq 0 \quad \text{(kN)} \tag{4.38-b}$$

$$g_3(x) = -F_\tau + 14.0 \leq 0 \quad \text{(kN)} \tag{4.38-c}$$

$$g_4(x) = B_\tau - 1.6 \leq 0 \quad \text{(Tesla)} \quad \text{(4.38-d)}$$

$$g_5(x) = Re - 1600 \leq 0 \quad \text{(Dimensionless)} \quad \text{(4.38-e)}$$

$$g_6(x) = D_{in} - 0.095 \leq 0 \quad \text{(meter)} \quad \text{(4.38-f)}$$

$$g_7(x) = V_b - 3.7 \times 10^{-4} \leq 0 \quad (m^3) \quad \text{(4.38-g)}$$

$$g_8(x) = -x_1 + 0.0005 \leq 0 \quad \text{(meter)} \quad \text{(4.38-h)}$$

$$g_9(x) = x_1 - 0.002 \leq 0 \quad \text{(meter)} \quad \text{(4.38-i)}$$

$$g_{10}(x) = -x_2 + 0.0035 \leq 0 \quad \text{(meter)} \quad \text{(4.38-j)}$$

$$g_{11}(x) = x_2 - 0.008 \leq 0 \quad \text{(meter)} \quad \text{(4.38-k)}$$

$$g_{12}(x) = -x_3 + 0.008 \leq 0 \quad \text{(meter)} \quad \text{(4.38-l)}$$

$$g_{13}(x) = x_3 - 0.035 \leq 0 \quad \text{(meter)} \quad \text{(4.38-m)}$$

$$g_{14}(x) = -x_4 + 0.005 \leq 0 \quad \text{(meter)} \quad \text{(4.38-n)}$$

$$g_{15}(x) = x_4 - 0.02 \leq 0 \quad \text{(meter)} \quad \text{(4.38-o)}$$

$$g_{16}(x) = -x_5 + 1.02 \leq 0 \quad \text{(Dimensionless)} \quad \text{(4.38-p)}$$

$$g_{17}(x) = x_5 - 1.07 \leq 0 \quad \text{(Dimensionless)} \quad \text{(4.38-q)}$$

$$g_{18}(x) = -x_6 + 1.43 \leq 0 \quad \text{(Dimensionless)} \quad \text{(4.38-r)}$$

$$g_{19}(x) = x_6 - 1.45 \leq 0 \quad \text{(Dimensionless)} \quad \text{(4.38-s)}$$

The inequality constraints g_1 and g_2 represent the constraints on the field-off stroking load which should be varied between 15 and 15.25 kN to ensure that the MREA can passively generate the required damping force at the high end impact velocity of 5 m/s. This limits the undesirable increase in the damping force due to the piston velocity squared as it sharply decreases the dynamic range at the design speed. The constraint g_3 sets the minimum controllable damping force that should be generated by the optimized device to ensure attaining satisfactory performance by

having dynamic range of around two at 5 m/s. Moreover, the inequality constraint g_4 is introduced to ensure that the magnetic flux density of the MR fluid in the gap does not exceed the saturation limit. This, in turn, will assure achieving maximum performance and avoid locking off the magnetic circuit. By using inequality constraint g_5, the flow is maintained laminar at a sufficient margin of 400 below the threshold value of 2000. This enables avoiding rapid increase in the field independent damping force at high impact velocities due to the velocity squared effect. Thus, maximizes the dynamic range. The inequality constraints g_6 to g_{19} are the geometrical ones which are introduced to assure that the optimized MREA will fit in the allocated space between the fuselage's sub-floor structure and the crosstubes as shown in Figure 4.4.

4.9 Results and discussion

The formulated optimization problem in Eqs. (4.37) and (4.38) has been solved using the genetic algorithm (GA) and the SQP techniques. GA method was first executed to identify the near global optimum. Then the true global optimum solution was captured using SQP by using the GA optimum design variables as initial design points to the SQP algorithm, as explained in section 4.3. In all SQP simulations, the different initial points from GA yielded the same optimum solution of the dynamic range. This guaranteed that the global solution was successfully attained. The sample of the calculations in Table 4.5 presents the convergence of the SQP to the global optimum solution for different initial design points. The optimum dimensions of the bi-fold MREA and the other relevant performance parameters are provided in Tables 4.6 and 4.7, respectively. The iterations history of the SQP solution is presented in Figure 4.14 to show that the objective function was converged to the global optimum solution in only four iterations.

Table 4.5. Convergence of SQP to the maximum global solution.

Initial design variables (X_0)* (GA optimum solution after several runs)	Optimum design variables (X)*	D
(0.80, 8.0, 24.8, 5.7, 1.02, 1.45)	(0.80, 7.3, 24.9, 7.2, 1.02, 1.45)	2.0
(0.80, 8.0, 24.4, 5.6, 1.03, 1.45)		
(0.80, 7.9, 24.1, 5.6, 1.05, 1.448)		
(0.80, 7.9, 24.8, 5.7, 1.02, 1.45)		
(0.80, 8.0, 24.6, 5.6, 1.028, 1.45)		

Table 4.6. Dimensions of the optimized MREA.

Parameter	Value
MREA Shell diameter (D_s), mm	100.0
Bobbin length (H), mm	48.0
MR Valve thickness (d), mm	0.80
Coil width (w), mm	7.3
MR valve diameter (D_b), mm	66.672
Piston head diameter (D_p), mm	41.4
MR valve active length (l), mm	24.9
Coil length (l_c), mm	7.2

Using the optimized parameters, Figure 4.15 compares the maximum stroking load generated at the on-state condition by BP and BPM models. It can be seen from the figure that when the minor losses are neglected, the damping force is linearly proportional with the impact velocity. On the other hand, when the minor loss coefficients are taken into account, the curve is non-linear and is more accurate [29]. The BP underestimates the damping force, and the estimated error between the results of the BP and BPM rises quadratically with the increase in the piston velocity. At piston velocity of 5 m/s, the error reaches 18%. This means that the damping force generated due to the minor losses at high impact velocity is significant and should not be neglected.

Table 4.7. Relevant output parameters of the optimum MREA.

Parameter	Value	Unit
Re	1600	–
N	164	Turn
B_τ	0.939	Tesla
$\tau_{y,\,max}$	48.0	kPa
F_τ	14.82	kN
F_{off} (BPM model)	15.0	kN

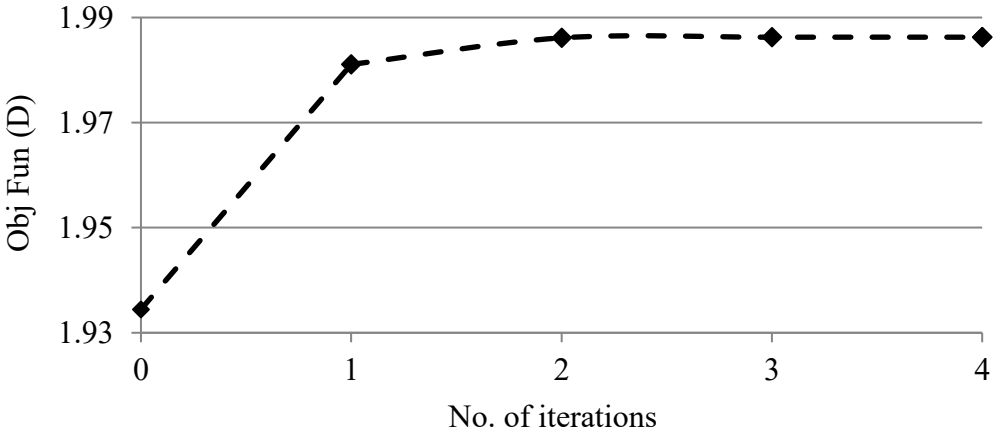

Fig. 4.14. SQP Iteration history of the optimized bi-fold MREA.

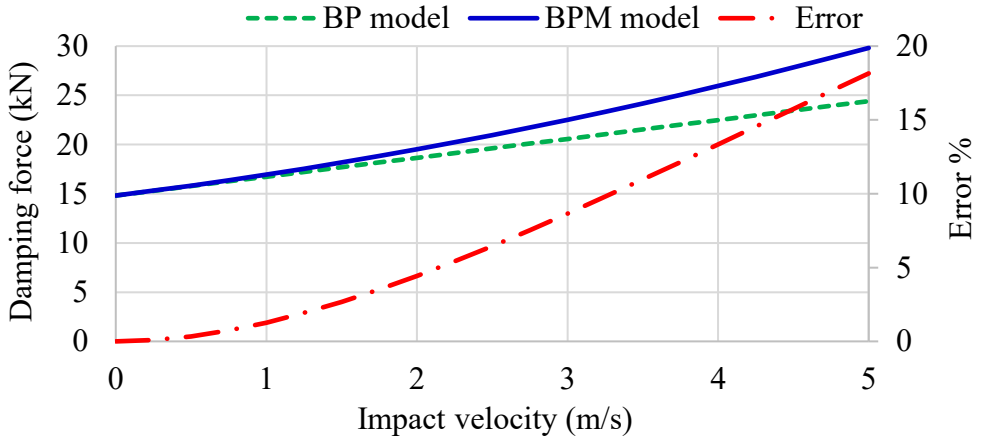

Fig. 4.15. Comparion of the on-state damping force prediction of the BP and BPM models.

The dynamic range (D) for the optimized bi-fold MREA is shown in Figure 4.16. In contrast to the damping force, the BP model overestimates the dynamic range because of the absence of the minor loss force component. The device attained dynamic ranges of 9 and 8 at impact velocity of 1 m/s for BP and BPM models, respectively. As the velocity increases, D decreases non-linearly with a quadratic increase in the error. Maximum error of 28% is computed at 5 m/s impact velocity.

Figure 4.17 plots the field-on damping force at different current inputs for the impact velocity range from zero to 5 m/s. Here, it is observed that the curves at different current inputs have similar identical shapes even though they are scaled by MR yield force which is controlled by the input current.

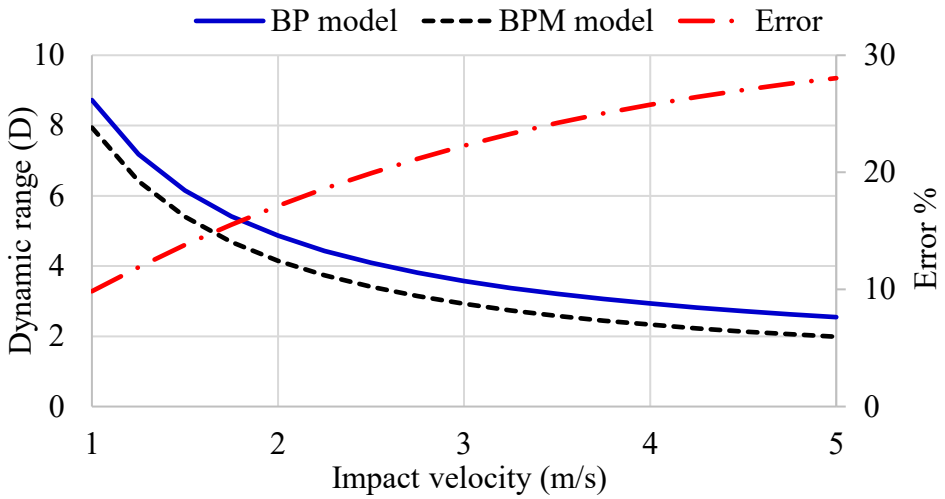

Fig. 4.16. Dynamic range vs. impact velocity.

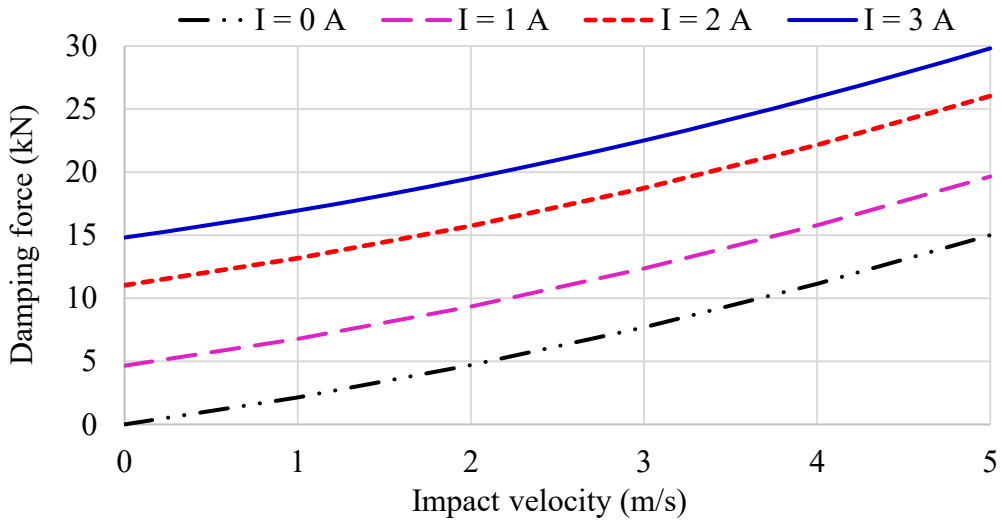

Fig. 4.17. Damping force generated at different input currents.

To confirm the results of the analytical magnetic solution, FEMM software was used to analyze one-half of the axisymmetric bobbin geometry. The magnetic flux density distribution in the MR gap and the bobbin is plotted in Figure 4.18 at current input of 3 A. The average magnetic density in the MR gap was computed by FEMM by integrating the nodal magnetic flux (B) densities along specified contour line (path) passing through the MR passage using the following relation [70]:

$$B_{avg} = \frac{1}{l}\int_0^l B(s)\, ds \tag{4.39}$$

Using magnetic FE analysis, average magnetic flux density in the inner and outer gap is found to be 0.904 and 0.749 T, respectively. The average magnetic flux density crossing the active gaps is then computed as 0.827 T [28]. Using analytical magnetic circuit analysis, average magnetic flux density in the equivalent single MREA active gap is found to be 0.939 T which agrees well with that of FE result. The difference of 0.112 T is attributed to the assumption of uniform magnetic flux density in analytical magnetic circuit analysis and also to the assumed linear relationship between magnetic flux density and magnetic field intensity [66]. In analytical approach, the magnetic flux lines are assumed crossing the MR valve normal to the MREA longitudinal axis which means that there is no loss due to the tangent component. The vector plot of the magnetic

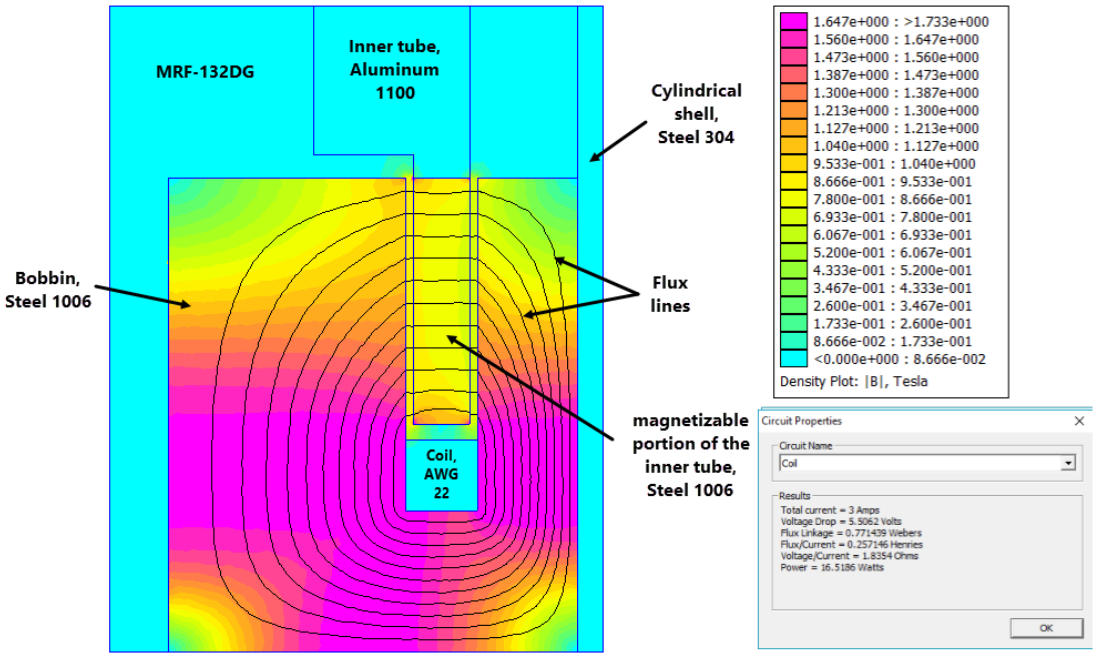

Fig. 4.18. Magnetic flux density distribution in the active region for current 3.0.

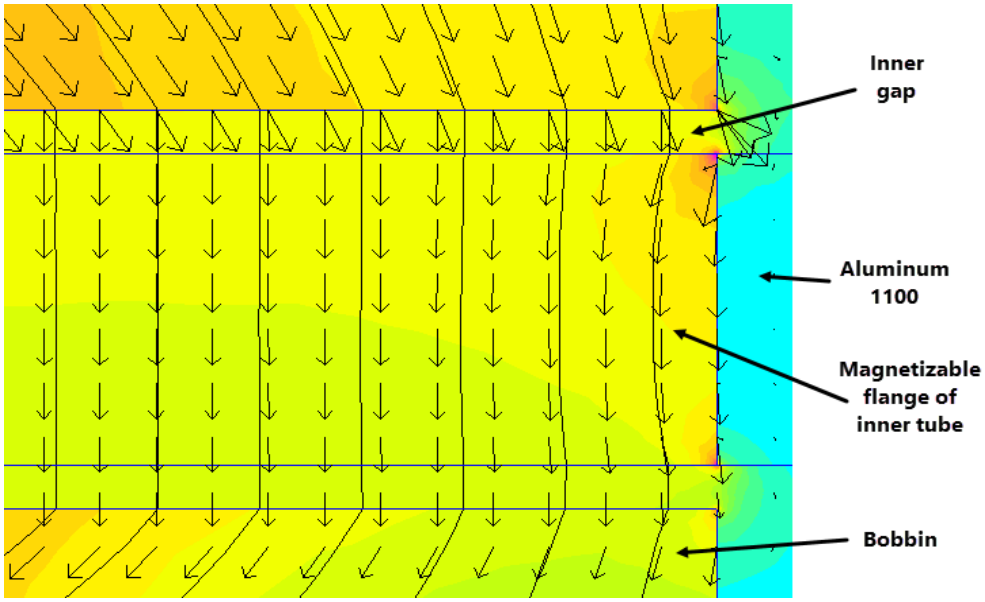

Fig. 4.19. Vector plot of magnetic flux density in portion of the active region.

flux lines in portion of the bobbin-MR gap region, shown in Figure 4.19, demonstrates that not all the flux lines align normal to the MR passage centerline, especially at the inner gap. Figure 4.20 also confirms that the analytical simplification results in a linear relationship between the magnetic flux density and the applied current, while in the magnetic analysis using FEMM, the relationship is nonlinear and more realistic.

Figure 4.21 depicts the relationship between the yield stress and the input current. Results show that the analytical model underestimated the yield stress at low current inputs. In the case of the FEMM analysis, the Figure shows that the curve becomes almost plateau at around 44 kPa starting from current I = 2.6 A. The reason of the curve flatness is the deviation of the flux vectors from the normal to the gap centerline where some flux escapes in the tangential direction. On contrary, the analytically calculated yield stress continues increasing beyond I = 2.6 A until it reaches the saturation value of 48 kPa at I = 3.0.

To employ the optimized bi-fold MREA in semi-active control systems, the relations between the MR yield force and the input current is extracted from Fig. 4.22 using the curve fitting technique The analytical and FEMM curve patterns are identical to their corresponding yield stress curves in Figure 4.21 due to the domination of the yield stress as expressed in Eq. (4.18). For the FEMM curve, it is noticeable that the maximum controllable damping force generated at I = 2.6 A is

13.742 kN, down from 14.8 kN for the analytical model. Therefore, the dynamics range is calculated as D = 1.92 based on the more accurate FEMM results compared to D = 1.99 based on the simplified magnetic circuit model. Nevertheless, the 3.5% drop in the D is acceptable and does not affect the performance of the device.

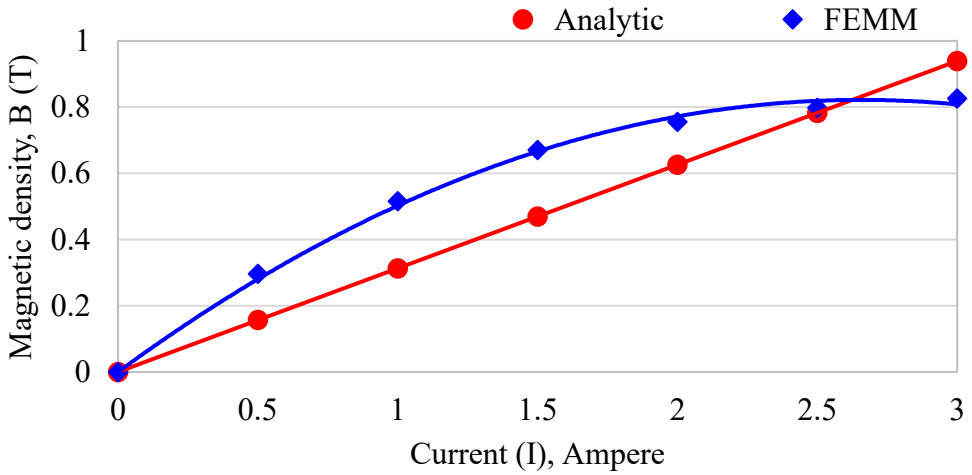

Fig. 4.20. Magnetic flux density vs. applied current.

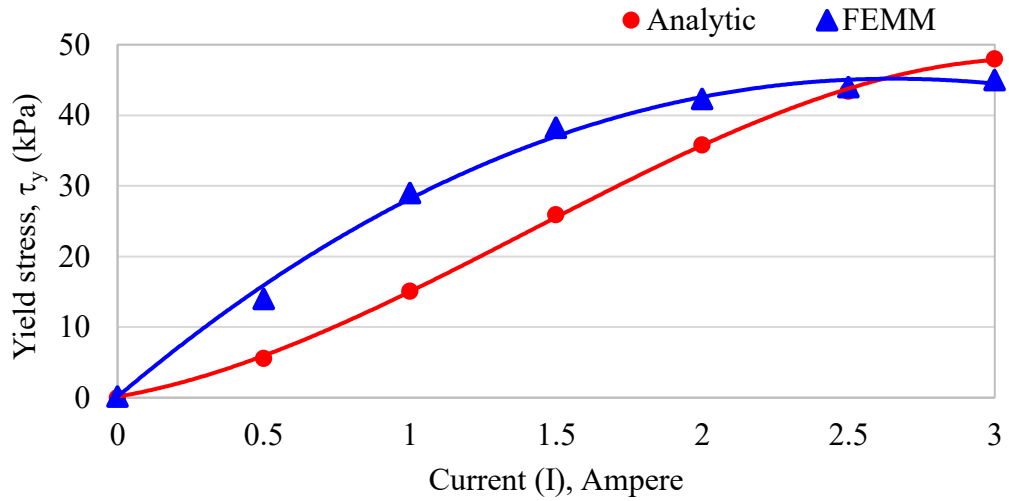

Fig. 4.21. Yield stress vs. input current.

The functions of MR yield force in kN in terms of the input current is extracted from Fig. 4.22 for the analytical and FEMM models as

$$\text{Analytical model: } F_\tau = -0.7408\, I^3 + 3.1233\, I^2 + 2.2031\, I + 0.0443 \quad (4.40)$$

$$\text{FEMM model: } F_\tau = 0.0543\, I^3 - 2.2634\, I^2 + 10.864\, I + 0.0443 \quad (4.41)$$

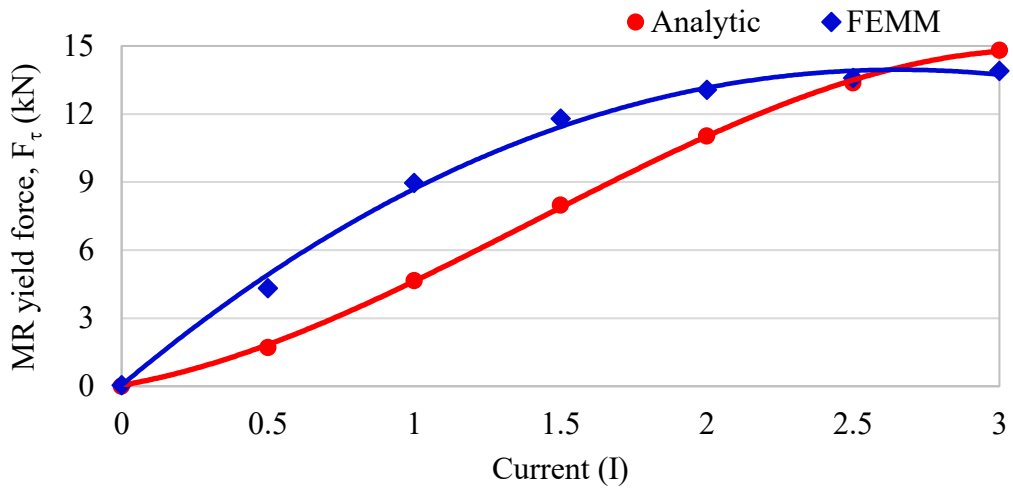

Fig 4.22. Controllable damping force vs. input current.

The preceding discussion demonstrated that the contribution of the minor losses in the total field-off damping force can no longer be neglected for the bi-fold MREA device to be implemented as a potential energy absorption device in the SLG system. Moreover, the MREA can be used as a representative device in the analysis of the single degree of freedom mass-damper-spring helicopter system. The more accurate behavior of the MREA and the helicopter in the event of impact is predicted by using the realistic non-linear viscous damping force which accounts for the minor losses in addition to the Darcy friction loss, as depicted in Figure 4.23. However, to simplify the analysis and predict the performance with good accuracy, the quadratic component of the passive damping force is to be approximated to linear component in the next chapter. In addition, the linearization is very beneficial in the design of the semi-active control algorithm for the SLG

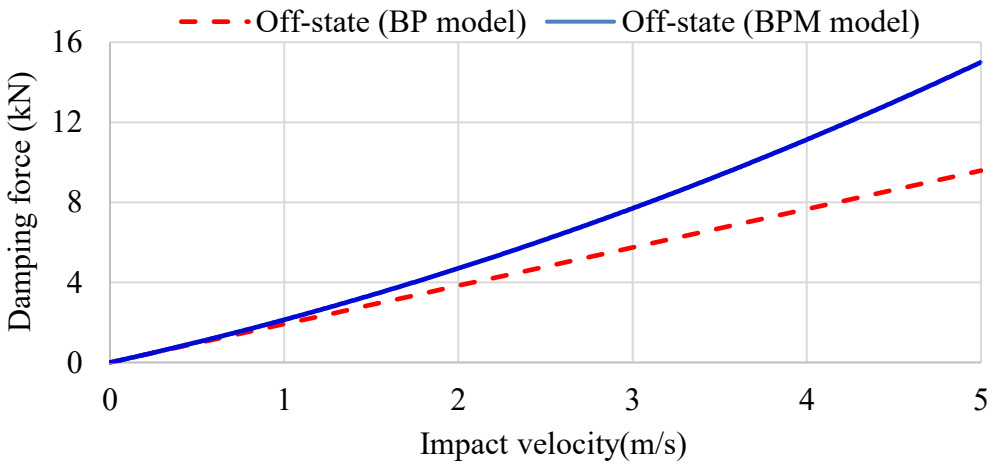

Fig. 4.23. Field-off damping force vs. impact velocity.

system when it is equipped with the MREA devices. This point will be discussed in the next chapter when the helicopter model is treated as a SDOF system. From Figure 4.23, the non-linear force-velocity relationship in the field-off mode is found using curve fitting method as

$$F_{off} = 0.2165\, V_p^2 + 1.9179\, V_p \tag{4.42}$$

4.10 Summary

The optimization study was conducted to maximize the dynamic range of the bi-fold MREA at a peak impact velocity of 5 m/s. The constraints were applied based on the practical fabrication and space requirements of the conventional SLG configurations adopted in the present research dissertation. Combined GA and SQP algorithms has been utilized to capture the true global optimum solution. The relations of the Bingham plastic model with minor loss factors and the magnetic circuit were utilized to formulate the design optimization problem. Fortunately, a unique maximum global solution could be obtained by achieving dynamic range of about 2 while all the problem constraints were not violated. The MREA was optimized to generate a peak off-state stroking load of 15 kN to meet the crashworthiness specifications for vertical rotorcraft impacts. In addition, a controllable yield force of 14.8 kN could be analytically produced when the magnetic field activated with 3.0 A current. This ensures good controllability over a wide range of the impact speed when the device is employed in the semi-active system. The MREA results using BPM model are also compared against the basic BP model. The study suggests that the use of BPM model is more accurate than the BP model under high velocity impacts. This is because the pressure drop estimated by the BP model led to overly erroneous performance. The error in dynamic range increases with the increase in the piston speed and reached 28% at 5 m/s. To confirm the results of the analytical magnetic analysis, the FEMM software was used. The analytically calculated magnetic flux density was found higher than that computed by the FEMM software by about 0.11 T. The difference is attributed to the simplification assumption made in the analytical solution. Finally, the non-linear passive damping force based on BPM model is expressed as a quadratic function with respect to impact velocity.

CHAPTER 5

Crashworthiness Analysis of a SDOF Helicopter Model

5.1 Introduction

The present chapter addresses the prediction of the helicopter response implementing the widely used single degree of freedom model. The conventional SLG configurations, in chapters two and three, are equipped with an optimized passive energy absorbers (EA) and also optimized bi-fold MREAs in an attempt to further enhance the energy absorption capacity of SLGs. The purpose is to adjust the energy absorption capabilities of the SLG system adaptively to accommodate different impact speeds beyond 2.44 m/s. This objective exceeds the requirement of the civilian crashworthiness specifications AWM chapter 527 and FAR part 27 and provides more protection to the occupants in high velocity impact events.

Herein, the performances of eight different configurations of the SLG system are assessed in terms of the non-dimensional displacement, velocity, and acceleration responses. For the passive EA, two distinct and different optimum damping ratios for minimum acceleration and for full utilization of the EA stroke are calculated. On the other hand, the optimum Bingham numbers for the compression and rebound strokes are determined for SLG equipped with the MREA device. A new chart called Bi^o-L chart is introduced. The purpose is to rapidly estimate the required optimum Bingham numbers at different values of sink rates and rotor lift factors. This chart is also beneficial in the design of the semi-active controllers because it accommodates the variations of the loading on the helicopter due to activation of the rotor lift load at the instant of contact with the ground.

5.2 Single degree of freedom representation of the helicopter model

The representation of the helicopter as a single degree of freedom (SDOF) model is found very useful in studying the response of the helicopter under different impact conditions. In this research dissertation, three SDOF helicopter models are formulated based on the absence or presence of the external energy dissipation mechanism: 1) Undamped SDOF helicopter model, mass-spring; 2) Passively damped SDOF helicopter model, mass-passive viscous damper-spring; and 3) SDOF helicopter model equipped with magnetorheological energy absorber, mass-MREA-spring. The simplified models of the above three configurations are provided in the subsequent

section in this chapter. The measurement of the EA size and the allocated space, based on the candidate SLG model in chapter two, results in a maximum vertical stroke of 200 mm to avoid end-stop impact. The equivalent linear stiffness of the SLG (spring) will be calculated using the least square fit method for the curve of the force-displacement of the SLG for up to 200 mm deflection. In addition, the energy absorber (EA) can either be passive or of MR type, as mentioned above. In the impact event, such contact would most likely increase the acceleration abruptly beyond the human's tolerance. To assess the performance of the helicopter under impact loads, the non-dimensional relations for displacement, velocity, and acceleration are obtained. It is worth noting that the MREA considered in this study is of bi-fold type, which was optimized in the preceding chapter.

The datum references for the evaluation are the baseline and optimized conventional SLGs. Earlier, these SLGs demonstrated their effectiveness in dissipating impact energy to meet the limit load and reserve energy drop tests. However, they require a stroke of up to 350 mm to accomplish the task successfully. In impacts of sink rate higher than 2.44 m/s, the efforts have been devoted toward incorporating supplemental energy dissipation devices such as dampers to maintain the suddenly transmitted acceleration within the tolerable level and to simultaneously maintain the fuselage intact by ensuring that the crosstubes do not collapse. However, the viscous passive dampers are found not suitable because of their lack of real-time adaptability to the impact environment. The damping coefficient of the passive damper is usually designed to attenuate impact loads at maximum gross weight and maximum design impact velocity. If the helicopter impacts the ground at the design condition, which cannot be always guaranteed, the energy would be maximally dissipated and the acceleration experienced by the occupants is minimized. However, when the impact velocity is lower than the design velocity, then the damper turns very stiff with lesser opportunity to dissipate the entire impact energy. Therefore, the initial acceleration of the impact might become higher than the peak acceleration when the helicopter is equipped with the conventional SLG alone. In contrast, i.e. when the helicopter hits the ground at sink rate higher than the design speed, then the damper suffers end-stop impact and high impact load is transmitted to the occupants.

5.3 Non-dimensional analysis of the single degree of freedom helicopter models

The governing equations of motion and the corresponding non-dimensional solutions of the aforementioned three single degree of freedom helicopter models will be derived in this section. In addition to the assumptions in chapters two and three, which are also valid in this study, two more assumptions related to the incorporation of the EA devices are considered:

1- The dampers have the same damping coefficient. Therefore, they can be represented as one damper having an equivalent damping coefficient.
2- In level impact, the horizontal components of the damping force cancel each other so that the only pertinent impact force component is the vertical component.

5.3.1 Helicopter equipped with conventional SLG

The equation of motion of the undamped SDOF helicopter model representing a rotorcraft with conventional SLG system as shown in Figure 5.1, can be written as:

$$m\,\ddot{x}(t) + k\,x(t) = -mg\,(1 - L) \tag{5.1}$$

where m is the rotorcraft mass, k is the equivalent linear stiffness of the conventional SLG, and L is the rotor lift factor.

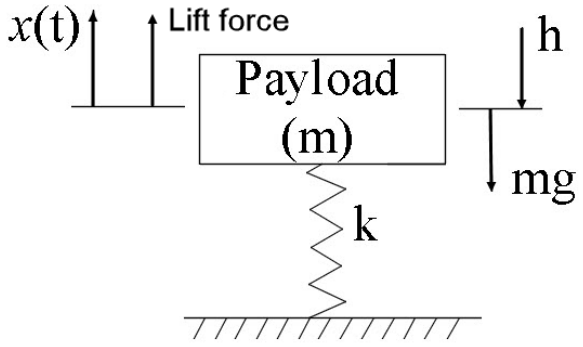

Fig. 5.1. SDOF representation of a helicopter model equipped with conventional SLG system.

The above equation can be rearranged to the following form:

$$\ddot{x}(t) + \omega_n^2 \left[x(t) + \frac{mg}{k}\,(1 - L)\right] = 0 \tag{5.2}$$

Solution of Eq. (5.2) has the following form

$$x(t) = C_1\,sin\,\omega_n t + C_2\,cos\,\omega_n t - \delta_{st}(1 - L) \tag{5.3}$$

where C_1 and C_2 are constants and δ_{st} is the static deflection of the spring. Assuming that the reference initial conditions at the instant of touchdown, the vertical velocity of the free falling helicopter at the touchdown, v_0, can be calculated from:

$$v_0 = \sqrt{2gh} \tag{5.4}$$

where h is the height from which the payload is released. Differentiating Eq. (5.3) twice gives the acceleration response of the payload as:

$$\ddot{x}(t) = -\omega_n^2 \left[C_1 \sin \omega_n t + C_2 \cos \omega_n t\right] \tag{5.5}$$

Eq. (5.3) can be converted into the non-dimensional form by using the following non-dimensional parameters:

$$\bar{t} = \omega_n t \; ; \; \bar{x}(\bar{t}) = \frac{x(t)}{S} \; ; \; \bar{v}_0 = \frac{v_0}{\omega_n S} \tag{5.6}$$

where S is the maximum permissible travel of the piston (stroke). The solution of the problem can now be expressed in the non-dimensional form as:

$$\bar{x}(\bar{t}) = C_{1n} \sin \bar{t} + C_{2n} \cos \bar{t} - \bar{\delta}_{st}(1 - L) \tag{5.7}$$

where

$$C_{1n} = \frac{C_1}{S} \; ; \; C_{2n} = \frac{C_2}{S} \; ; \; \bar{\delta}_{st} = \frac{\delta_{st}}{S} \tag{5.8}$$

Expression (5.7) is then differentiated to obtain the non-dimensional velocity and acceleration equations as:

$$\dot{\bar{x}}(\bar{t}) = C_{1n} \cos \bar{t} - C_{2n} \sin \bar{t} \tag{5.9}$$

$$\ddot{\bar{x}}(\bar{t}) = -(C_{1n} \sin \bar{t} + C_{2n} \cos \bar{t}) \tag{5.10}$$

To calculate the constants in Eq. (5.7), the following initial conditions are considered:

$$\bar{x}(0) = 0 \, , \; \dot{\bar{x}}(0) = -\bar{v}_0 \tag{5.11}$$

Solving Eqs. (5.7) and (5.8) for the initial conditions in (5.11) yields:

$$C_{1n} = -\bar{v}_0 \; , \; C_{2n} = \bar{\delta}_{st}(1 - L) \tag{5.12}$$

5.3.2 Helicopter equipped with conventional SLG and passive EA

By adding the passive EA element to the conventional SLG system, as illustrated in Figure 5.2, Eq. (5.1) is modified to:

$$m\,\ddot{x}(t) + c\,\dot{x}(t) + k\,x(t) = -mg\,(1 - L) \tag{5.13}$$

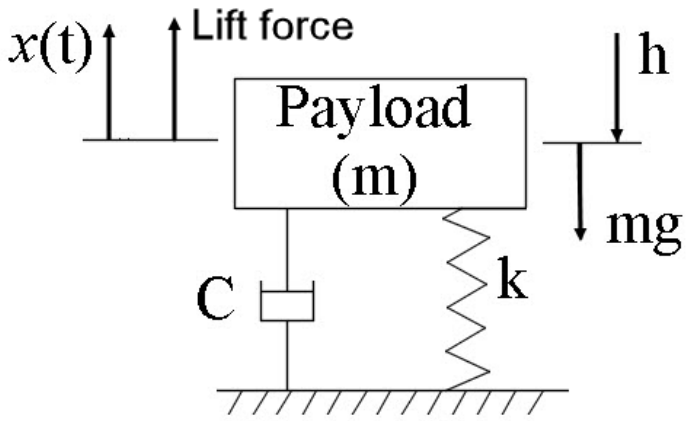

Fig. 5.2. SDOF representation of a helicopter model equipped with conventional SLG and passive EA.

In order to occupy smaller space to minimize the weight, under-damped EA system is preferred [71]. This requires that the damping ratio to be in the range $0 < \zeta < 1$. The damping coefficient, *c*, can be expressed as:

$$c = 2\zeta\, m\, \omega_n \tag{5.14}$$

By substituting (5.14) into Eq. (5.13), the governing equation of motion can be described as:

$$\ddot{x}(t) + 2\zeta\, \omega_n\, \dot{x}(t) + \omega_n^2\, x(t) = -\delta_{st}\,(1 - L) \tag{5.15}$$

Now, let the solution of (5.15) be:

$$x(t) = e^{-\zeta\,\omega_n t}(A_1\, sin\, \omega_d t + B_1\, cos\, \omega_d t) - \delta_{st}(1 - L) \tag{5.16}$$

where ω_d is the damped natural frequency of the system and given by $\omega_d = \omega_n\sqrt{1-\zeta^2}$. A_1 and

B_1 are constants to be determined from the initial conditions provided in Eq. (5.11). The velocity and acceleration responses are obtained by differentiating expression (5.16) with respect to time. Thus,

$$\dot{x}(t) = e^{-\zeta\,\omega_n t}[(\omega_d A_1 - \zeta\,\omega_n B_1)\,cos\,\omega_d t - (\zeta\,\omega_n A_1 + \omega_d B_1)\,sin\,\omega_d t] \tag{5.17}$$

$$\ddot{x}(t) = e^{-\zeta\,\omega_n t}\{\left[(\zeta^2\omega_n^2 - \omega_d^2)A_1 + 2\zeta\,\omega_n\omega_d B_1\right] sin\,\omega_d t + \left[(\zeta^2\omega_n^2 - \omega_d^2)B_1 - 2\zeta\,\omega_n\omega_d A_1\right] cos\,\omega_d t\} \tag{5.18}$$

To compare the performance of the damped system with respect to the reference undamped model, the displacement equation (5.16) is also normalized using the parameters provided in Eq. (5.6). Thus, the non-dimensional solution becomes:

$$\bar{x}(\bar{t}) = e^{-\zeta\,\bar{t}}\,(A_{1n}\,sin\,\bar{\omega}_d\bar{t} + B_{1n}\,cos\,\bar{\omega}_d\bar{t}) - \bar{\delta}_{st}(1-L) \tag{5.19}$$

where $\bar{\omega}_d$ is the normalized damped natural frequency with respect to ω_n and the constants A_{1n} and B_{1n} are non-dimesionalized with respect to stroke S. These non-dimensional parameters are given by

$$\bar{\omega}_d = \sqrt{1-\zeta^2}\;;\; A_{1n} = \frac{A_1}{S}\;;\; B_{1n} = \frac{B_2}{S} \tag{5.20}$$

The non-dimensional velocity and acceleration are then:

$$\dot{\bar{x}}(\bar{t}) = e^{-\zeta\,\bar{t}}\,[(\bar{\omega}_d A_{1n} - \zeta\,B_{1n})\,cos\,\bar{\omega}_d\bar{t} - (\bar{\omega}_d B_{1n} + \zeta\,A_{1n})\,sin\,\bar{\omega}_d\bar{t}] \tag{5.21}$$

$$\ddot{\bar{x}}(\bar{t}) = e^{-\zeta\,\bar{t}}\{\left[(\zeta^2 - \bar{\omega}_d^2)A_{1n} + 2\zeta\,\bar{\omega}_d B_{1n}\right]\sin\bar{\omega}_d\bar{t} + \left[(\zeta^2 - \bar{\omega}_d^2)B_{1n} - 2\zeta\,\bar{\omega}_d A_{1n}\right] cos\,\bar{\omega}_d\bar{t}\} \tag{5.22}$$

Solving Eqs. (5.19) and (5.21) for the initial conditions given in Eq. (5.11) yields the values of constants A_{1n} and B_{1n} as:

$$A_{1n} = \frac{1}{\bar{\omega}_d}(\zeta\,B_{1n} - \bar{v}_0)\;;\; B_{1n} = \bar{\delta}_{st}(1-L) \tag{5.23}$$

5.3.3 Helicopter equipped with conventional SLG and bi-fold MREA

The governing equation of motion of the SDOF helicopter model equipped with MREA, as shown in Figure 5.3, is similar to that for SLG with passive EA. One exception is applicable to the MREA is that the controllable yield force term (f_y) is added to the system to emulate the generation of the yield damping force which is activated and deactivated by the magnetic field [71]. The governing equation of motion can, therefore, be written as:

$$\ddot{x}(t) + 2\zeta\,\omega_n\,\dot{x}(t) + \omega_n^2\,x(t) = -\frac{f_y}{k}\,sgn\{\dot{x}(t)\} - \delta_{st}(1-L) \tag{5.24}$$

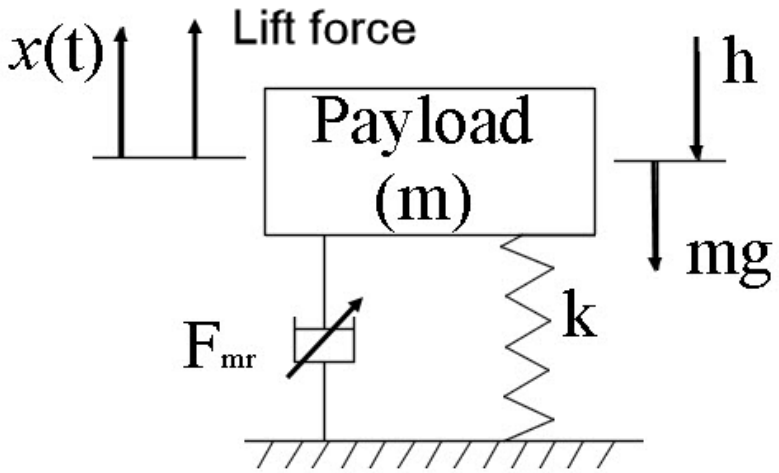

Fig. 5.3. SDOF representation of a helicopter model equipped with conventional SLG and MREA.

where the signum function $sgn\{\dot{x}(t)\}$ is defined as

$$sgn\{\dot{x}(t)\} = \begin{cases} 1 & if\ \dot{x}(t) > 0 \\ 0 & if\ \dot{x}(t) = 0 \\ -1 & if\ \dot{x}(t) < 0 \end{cases} \tag{5.25}$$

The MR yield force can be adjusted by varying the input current based on the direction of the piston velocity in the compression and rebound strokes. Hence, each stroke can be analyzed and optimized individually. In this case, the non-dimensional solution of the under-damped SDOF helicopter model which incorporates the MREA can be expressed as:

$$\bar{x}(\bar{t}) = e^{-\zeta\,\bar{t}}\,(L_{1n}\,sin\,\bar{\omega}_d\bar{t} + L_{2n}\,cos\,\bar{\omega}_d\bar{t}) \pm \frac{f_y}{k.s} - \bar{\delta}_{st}(1-L) \tag{5.26}$$

5.3.3.1 Non-dimensional compression stroke

Using expression (5.26), the non-dimensional displacement of the payload in the compression stroke can be expressed as:

$$\bar{x}(\bar{t}) = e^{-\zeta\,\bar{t}}\,(L_{1n}\,sin\,\bar{\omega}_d\bar{t} + \,L_{2n}\,cos\,\bar{\omega}_d\bar{t}) + \frac{f_{yc}}{k.s} - \,\bar{\delta}_{st}(1-L) \tag{5.27}$$

For the non-dimensional analysis, the yield force can be expressed in terms of Bingham number in the compression stroke, Bi_c, linear damping coefficient, c, and piston speed , v_0, as:

$$Bi_c = \frac{f_{yc}}{cv_0} \tag{5.28}$$

The substitution of Eqs. (5.6), (5.14) and (5.28) into (5.27) yields

$$\bar{x}(\bar{t}) = e^{-\zeta\,\bar{t}}\,(L_{1n}\,sin\,\bar{\omega}_d\bar{t} + \,L_{2n}\,cos\,\bar{\omega}_d\bar{t}) + 2\zeta\,Bi_c\bar{v}_0 - \,\bar{\delta}_{st}(1-L) \tag{5.29}$$

The differentiation of (5.29) gives the non-dimensional velocity and non-dimensional acceleration, respectively, as

$$\dot{\bar{x}}(\bar{t}) = e^{-\zeta\,\bar{t}}\,[(\bar{\omega}_d L_{1n} - \zeta L_{2n})\cos\bar{\omega}_d\bar{t} - (\bar{\omega}_d L_{2n} + \zeta L_{1n})\,sin\,\bar{\omega}_d\bar{t}] \tag{5.30}$$

$$\ddot{\bar{x}}(\bar{t}) = e^{-\zeta\,\bar{t}}\{\left[(\zeta^2 - \bar{\omega}_d^2)L_{1n} + 2\zeta\,\bar{\omega}_d L_{2n}\right]\sin\bar{\omega}_d\bar{t} + \left[(\zeta^2 - \bar{\omega}_d^2)L_{2n} - 2\zeta\,\bar{\omega}_d L_{1n}\right]cos\,\bar{\omega}_d\bar{t}\} \tag{5.31}$$

By solving expressions (5.29) and (5.30) for the initial conditions given in Eq. (5.11), the constants L_{1n} and L_{2n} are determined as:

$$L_{1n} = \frac{1}{\bar{\omega}_d}(\zeta\,L_{2n} - \,\bar{v}_0) \tag{5.32}$$

$$L_{2n} = -[2\zeta\,Bi_c\bar{v}_0 - \bar{\delta}_{st}(1-L)] \tag{5.33}$$

It is noted that when the compression stroke is terminated, the vertical velocity becomes zero. Thus, the elapsed duration from the touchdown until the system comes to instantaneous rest, designated by ($\bar{t}_c$), can be computed by equating Eq. (5.30) to zero so that:

$$\dot{\bar{x}}(\bar{t}) = \,\dot{\bar{x}}(\bar{t}_c) = 0 \tag{5.34}$$

or

$$\bar{t}_c = \frac{1}{\bar{\omega}_d} tan^{-1}\left(\frac{\bar{\omega}_d L_{1n} - \zeta L_{2n}}{\bar{\omega}_d L_{2n} + \zeta L_{1n}}\right) \tag{5.35}$$

The optimum Bingham number for the compression stroke is achieved when the EA stoke is fully utilized as:

$$\bar{x}(\bar{t}_c) = -1 \tag{5.36}$$

By equating expression (5.29) to (5.36), the optimum Bingham number for compression stroke is obtained as:

$$Bi_c^o = \frac{-1}{2\zeta\, \bar{v}_0}\left[1 + e^{-\zeta \bar{t}_c}(L_{1n}\, sin\, \bar{\omega}_d \bar{t}_c + L_{2n}\, cos\, \bar{\omega}_d \bar{t}_c) - \bar{\delta}_{st}(1 - L)\right] \tag{5.37}$$

5.3.3.2 Non-dimensional rebound stroke

The rebound stroke comprises the second half of the energy dissipation cycle and it commences after the completion of the compression stroke. With the generated optimum rebound yield force, the helicopter dissipates the energy stored in the spring in a controllable manner such that the system resettles to its reference position at touchdown with no further oscillatory motion. This protects the occupants from the consequences of post-impact vibratory force. Similar to Eq. (5.28), the Bingham number for the rebound stroke can be expressed as:

$$Bi_r = \frac{f_{yr}}{cv_0} \tag{5.38}$$

The equations of the non-dimensional responses of the rebound stroke are identical to those for the compression stroke except for the different constants. Considering Eq. (5.25), these response equations can be written as

$$\bar{x}(\bar{t}) = e^{-\zeta \bar{t}}\,(L_{3n}\, sin\, \bar{\omega}_d \bar{t} + L_{4n}\, cos\, \bar{\omega}_d \bar{t}) - 2\zeta\, Bi_r \bar{v}_0 - \bar{\delta}_{st}(1 - L) \tag{5.39}$$

$$\dot{\bar{x}}(\bar{t}) = e^{-\zeta \bar{t}}\,[(\bar{\omega}_d L_{3n} - \zeta L_{4n}) \cos \bar{\omega}_d \bar{t} - (\bar{\omega}_d L_{4n} + \zeta L_{3n}) sin\, \bar{\omega}_d \bar{t}] \tag{5.40}$$

$$\ddot{\bar{x}}(\bar{t}) = e^{-\zeta \bar{t}}\{\left[(\zeta^2 - \bar{\omega}_d^2)L_{3n} + 2\zeta\, \bar{\omega}_d L_{4n}\right] \sin \bar{\omega}_d \bar{t} + \left[(\zeta^2 - \bar{\omega}_d^2)L_{4n} - 2\zeta\, \bar{\omega}_d L_{3n}\right] cos\, \bar{\omega}_d \bar{t}\} \tag{5.41}$$

Constants L_{3n} and L_{4n} can now be found by solving the equations of non-dimensional displacement and velocity for the following initial conditions

$$\bar{x}(\bar{t}) = \bar{x}(\bar{t}_c)\,;\ \dot{\bar{x}}(\bar{t}) = \dot{\bar{x}}(\bar{t}_c) = 0 \tag{5.42}$$

and the solution gives

$$L_{3n} = e^{\zeta \bar{t}_c}\left[\bar{x}(\bar{t}_c) + 2\zeta\, Bi_r \bar{v}_0 + \bar{\delta}_{st}(1-L)\right] \frac{(\bar{\omega}_d \sin \bar{\omega}_d \bar{t}_c + \zeta \cos \bar{\omega}_d \bar{t}_c)}{\bar{\omega}_d} \tag{5.43}$$

and

$$L_{4n} = e^{\zeta \bar{t}_c}\left[\bar{x}(\bar{t}_c) + 2\zeta\, Bi_r \bar{v}_0 + \bar{\delta}_{st}(1-L)\right] \frac{(\bar{\omega}_d \cos \bar{\omega}_d \bar{t}_c - \zeta \sin \bar{\omega}_d \bar{t}_c)}{\bar{\omega}_d} \tag{5.44}$$

The optimum Bingham number of the rebound stroke measures the required amount of yield force so that the system returns to its original equilibrium point after completing one cycle from the instant of touchdown [71]. Equating Eq. (5.39) to zero gives the optimum Bingham number for the rebound stroke as:

$$Bi_r^o = \frac{1}{2\zeta\, \bar{v}_0}\left[e^{-\zeta \bar{t}_r}(L_{3n}\, sin\, \bar{\omega}_d \bar{t}_r + L_{4n}\, cos\, \bar{\omega}_d \bar{t}_r) - \bar{\delta}_{st}(1-L)\right] \tag{5.45}$$

The optimum Bingham numbers in expressions (5.37) and (5.45) are functions of themselves and can be calculated using an iterative numerical method. The non-dimensional time at which the non-oscillatory rebound stroke is terminated can be calculated as

$$\bar{t}_r = \bar{t}_c + \frac{\pi}{\bar{\omega}_d} \tag{5.46}$$

The non-dimensional force experienced by the helicopter occupants can be expressed as:

$$\bar{F}(\bar{t}) = \frac{m\ddot{x}(t)}{cv_0} \tag{5.47}$$

Also, the non-dimensional acceleration is given by:

$$\ddot{\bar{x}}(\bar{t}) = \frac{\ddot{x}(t)}{\omega_n^2\, S} \tag{5.48}$$

The substitution of Eqs. (5.6), (5.14), and (5.48) into (5.47) yields the non-dimensional force as

$$\bar{F}(\bar{t}) = \frac{\ddot{\bar{x}}(\bar{t})}{2\zeta\, \bar{v}_0} \tag{5.49}$$

5.4 Determination of the equivalent linear stiffness and damping coefficient using statistical methods

5.4.1 The equivalent linear stiffness

A considerable difference in the stiffness of the standalone baseline and optimum SLG configurations is observed due to variation in their cross sectional dimensions. To simplify the formulation of the equations of motion of the helicopter models and make them more suitable for the design of the semi-active control system, both the nonlinear spring constant and damping coefficient can be statistically linearized with good accuracy. Recall equations (2.18) and (3.30) which describe the force-deflection curves of the baseline and optimum SLG

Baseline SLG: $F_s = 934372\,x^3 - 935237\,x^2 + 318616\,x\,,\ R^2 = 1.0$ (2.18)

and

Optimum SLG: $F_s = 691093\,x^3 - 663521\,x^2 + 229377\,x\,,\ R^2 = 1.0$ (3.30)

In symbolic form the above equations can be expressed as

$$F_s = k_{b,c}\,x^3 - k_{b,q}\,x^2 + k_b\,x \tag{5.50}$$

and

$$F_s = k_{o,c}\,x^3 - k_{o,q}\,x^2 + k_o\,x \tag{5.51}$$

where subscripts *b* and *o* denote baseline and optimum SLG designs and the subscripts *c* and *q* refer to the cubic and quadratic coefficients. The above function can be written in terms of the linear spring modulus respectively as

$$F_s = K_b(\varphi\,x^3 - \varphi\,x^2 + \,x) \tag{5.52}$$

and

$$F_s = k_o(\varphi\,x^3 - \varphi\,x^2 + \,x) \tag{5.53}$$

Both Eqs. (5.52) and (5.53) can be represented in the following general form:

$$F_s = k(\varphi\,x^3 - \varphi\,x^2 + \,x) \tag{5.54}$$

here the factor φ relates the averaged nonlinear stiffness to the linear stiffness and approximated to $\varphi = 2.94$ for both systems. By comparing Eq. (2.18) to (3.30) it can be seen that there is a substantial decrease in the elastic linear stiffness of the optimum SLG compared to the baseline counterpart. Certainly, this affects the behavior of the SLG under different impact loading conditions. Furthermore, based on the available space for the MREA that to be assembled between the helicopter fuselage and the assembly point on the crosstube, as shown in Fig. 4.4, it is found that the maximum permissible stroke of the MREA piston is 20 cm. However, equations 2.18 and 3.30 reveal that both SLGs exhibit nonlinear behavior when the deflection exceeds 10 cm. As explained above, utilization of the entire MREA stroke means that the spring will undergo nonlinear behavior. However, the evaluation of the dynamic responses of the SDOF helicopter assumes linear spring constant and linear damping coefficient, as discussed in section 5.3. Thus, for the sake of computational simplicity and practical applications, it would be necessary to linearize nonlinear functions for both stiffness and damping forces and identify the equivalent stiffness and damping coefficients which could then be effectively utilized for linear analysis of SDOF system. The linearization is also more suitable from the perspective of the design of the semi-active control algorithm. the design and the implementation of the system in the semi-active control requires that the stiffness to be linearized with a reasonable accuracy.

Among the various linearization methods, the statistical linearization technique, also known as the difference minimization procedure, has found applications in the linearization of the non-linear single degree of freedom dynamical systems [73,74]. This method is based on minimizing the error between the proposed equivalent linear function and the actual exact non-linear function. Spanos [73] used the statistical approximation methods to linearize the nonlinear system under transient loading. The statistical linearization techniques have been well known in the approximation of the nonlinear dynamical responses with high accuracy. Since there is no coupling between the damping effect and the spring stiffness [73], the statistical linearization technique will be used to determine the equivalent linear stiffness of both baseline and optimal SLG configurations separately from the damping coefficient. Herein, the procedure presented in Refs. [73] and [74] will be used.

As mentioned before, the helicopter exhibits non-linear behavior in the event of high speed impact that can be simplified by a SDOF mass-spring or mass-damper-spring models depending

on whether the EA is integrated to the SLG or not. Based on Eq. (5.1), for the mass-spring system the equation of motion can be expressed in the nonlinear stiffness is in the following form

$$m\ddot{x} + k\,x + k(\varphi\,x^3 - \varphi\,x^2) = -mg(1-L) \tag{5.55}$$

The nonlinear terms can be replaced by the notation $\varphi f(x)$ and thus Eq. (5.55) can be rewritten as:

$$m\ddot{x} + k\,x + \varphi f(x) = -mg(1-L) \tag{5.56}$$

Ref. [73] reported that for cubic nonlinearity mass-spring system with very large values of coefficient φ, the difference is less than 7.5% between the exact solution and the approximate solution of the statistically linearized system. Now, let us assume that the equivalent linear system is given by [74]:

$$m\ddot{x} + k\,x + k_e\,x + \varepsilon(x) = -mg(1-L) \tag{5.57}$$

here k_e denotes the equivalent linear stiffness coefficient of the non-linear spring elements, and $\varepsilon\,(x)$ is the error. Subtracting (5.57) from (5.56) yields:

$$\varepsilon(x) = \varphi\,f(x) - k_e x \tag{5.58}$$

The mean squared error method can now be used to minimize the difference ε as [73]:

$$minimize\ \varepsilon^2 = [\varphi\,f(x) - k_e x]^2 \tag{5.59}$$

Differentiating Eq. (5.61) with respect to k_e and then equate it to zero [73,74]:

$$\frac{d\varepsilon^2}{dk_e} = [\varphi\,f(x) - k_e x]^2 = (\varphi\,f(x) - k_e x)x = 0 \tag{5.60}$$

The value of k_e can be evaluated by rearranging Eq. (5.60) and calculating the mean value by integrating the function over one cycle [74] as:

$$k_e = \frac{\frac{1}{2\pi}\int_0^{2\pi} \varphi f(x)x\,dt}{\frac{1}{2\pi}\int_0^{2\pi} x^2\,dt} \tag{5.61}$$

The substitution of the nonlinear force from (5.55) into (5.61) yields

$$k_e = \frac{\frac{1}{2\pi}\int_0^{2\pi} \varphi k(\, x^3 - \, x^2)x \, dt}{\frac{1}{2\pi}\int_0^{2\pi} x^2 \, dt} \tag{5.62}$$

The determination of the equivalent elastic stiffness is based on the solution of the mass-spring system in Section 5.3.1. By considering Eq. (5.3), one may write the solution for equivalent linear system as:

$$x(t) = (A\, cos\, \omega_{eq} t + B\, sin\, \omega_{eq} t) - \delta_{st}(1 - L) \tag{5.63}$$

Differentiate equation (6.63) once with respect to time yields:

$$\dot{x}(t) = -A\, \omega_{eq}\, sin\, \omega_{eq} t \mp B\, \omega_{eq}\, cos\, \omega_{eq} t \tag{5.64}$$

The initial condition for the problem are given by

$$x(0) = 0\,,\ \dot{x}(0) = \, - v_0 \tag{5.65}$$

The constants A and B are calculated by solving functions (5.63) and (5.64) using the above initial conditions so that:

$$A = \, \delta_{st}(1 - L) \quad , \quad B = -\frac{v_0}{\omega_{eq}} \tag{5.66}$$

The solution can be written in the form:

$$x(t) = R \cos\left(\omega_{eq} t + \emptyset\right) - \delta_{st}(1 - L) \tag{5.67}$$

where the amplitude R is given by:

$$R = \sqrt{((\delta_{st}(1 - L))^2 + (-\frac{v_0}{\omega_{eq}})^2)^2} \tag{5.68}$$

and the phase angle $\emptyset$ is defined as:

$$\emptyset = \, tan^{-1}(\frac{B}{A}) \tag{5.69}$$

After substituting Eq. (5.67) into (5.62) and conducting integration the equivalent linear stiffness associated with nonlinear stiffness terms can be obtained as:

$$k_e = \frac{3}{4}\,\varphi\, k[R^2 + 4\delta_{st}(1 - L)] \tag{5.70}$$

The overall equivalent linear spring stiffness is then easily found by adding k_e to k as:

$$k_{e,all} = k + k_e \tag{5.71}$$

5.4.2 The equivalent linear damping coefficient

As mentioned in Chapter 4, under high impact velocity the effect of minor losses cannot be ignored which results in nonlinear damping term. Figure 4.23 shows that the field-off damping force for MREA generated under high impact velocity is quadratic in nature and can be defined by recalling Eq. (4.42) the following function:

$$\mathrm{F_{off}} = 0.2165\,\dot{x}^2 + 1.9179\,\dot{x} \tag{4.42}$$

where c_q and c is the quadratic and linear damping coefficients which given as

$$c_q = 216.5\ \frac{Ns^2}{m^2} \quad \text{and} \quad c = 1918\ \frac{Ns}{m} \tag{5.73}$$

Similar to Eq. (5.71) the overall equivalent damping coefficient can be expressed as:

$$c_{e,all} = c + c_e \tag{5.74}$$

where c_e is the equivalent linear damping coefficient which can be determined using the procedure in Ref. [75]. First, the field-off pressure drop is calculated by combing Eqs. (4.12) and (4.17) to have

$$\Delta P_{off} = f\,\frac{\rho L V_d^2}{2D_h} + \rho\,\sum K_{ml\_i}\,\frac{V_d^2}{2} \tag{5.75}$$

where the hydraulic diameter $D_h = 2\,d$, and d is the MR valve thickness. The head loss can then be calculated as:

$$h = \frac{\Delta P_{off}}{\rho g} \tag{5.76}$$

which after substituting Eq. (5.75) yields:

$$h = \frac{\delta V_d^2}{2g} \tag{5.77}$$

where δ denotes the head loss coefficient due to the off-state pressure drop and is given by:

$$\delta = [f\frac{L}{2D_h} + \sum K_{ml\_i}] \tag{5.78}$$

Since the flow should remain laminar in the MR valve, f is defined by Eqs. (4.13) and (4.16) as

$$f = \frac{48\,\eta}{\rho\, d\, V_d} \tag{5.79}$$

here η is the viscosity of the MR fluid. The fluid velocity in the MR gap, V_d, can be calculated in terms of the piston (payload) velocity by substituting Eqs. (4.21) and (4.22) into the continuity equation (4.20). Once the friction loss coefficient, f, is found, one can obtain the head loss coefficient of the field-off MREA after substituting the factors of minor losses into Eq. (5.78). The equivalent linear damping coefficient of the nonlinear damping can now be determined as [75]:

$$c_e = \sqrt{\frac{2}{\pi}}\ \rho\, A_P \delta\, \sigma_{\dot{x}} \tag{5.80}$$

where $\sigma_{\dot{x}}$ is the standard deviation of the fluid velocity.

The equivalent linear damping coefficient can also be calculated using the classical approach by equating the energy due loss over one cycle due to nonlinear damping to that of equivalent linear damping force. The energy dissipated by the MREA due to quadratic damping term over one cycle can be expressed as:

$$E_{MREA} = c_q \int_{\frac{-\pi}{\omega}}^{\frac{\pi}{\omega}} \dot{x}^2\, sgn\{\dot{x}(t)\}\, dx \tag{5.81}$$

where $sgn\{\dot{x}(t)\}$ is defined in Eq. (5.25). By neglecting the phase angle, the velocity response for the equivalent linear system (ignoring the phase angle) can be represented as:

$$\dot{x}(t) = -\,\omega_{eq}\, R \sin\left(\omega_{eq} t\right) \tag{5.82}$$

The substitution of (5.82) into (5.81) and implementation of the signum function yields

$$E_{MREA} = 2c_q \omega_{eq}^3 R^3 \int_0^{\frac{\pi}{\omega_{eq}}} sin^3\left(\omega_{eq} t\right) dt \tag{5.83}$$

The equivalent linear damping coefficient can now be calculated by equating Eq. (5.83) to the energy dissipated by the equivalent linear damper per cycle as:

$$E_{MREA} = \pi c_e \, \omega_{eq} \, R^2 \tag{5.85}$$

From which, we can obtain

$$c_e = \frac{E_{MREA}}{\pi \omega_{eq} \, R^2} \tag{5.86}$$

It is noted that E_{MREA} in Eq. (5.83) can be easily obtained using numerical integration such as Simpson's rule.

5.5 The ratio of on-state to off-state damping coefficients

For the MREA working in the on-state condition, the activation of the magnetic field rises the apparent viscosity which in turn increases the equivalent damping coefficient. With the known value of the Bingham number, the ratio of the equivalent on-state damping coefficient, C_{on}, to the passive damping coefficient, c, can be expressed as [72] :

$$C_R = \frac{C_{on}}{c} = 1 + Bi \tag{5.89}$$

5.6 Parameters used in the analysis of the SDOF helicopter models

The non-dimensional analysis is conducted on eight versions of the SLG system based on the conventional SLG configuration and the type of the incorporated EA. The versions as designated as follows:

I. Configuration A: helicopter equipped with the standalone conventional baseline SLG

II. Configuration B: helicopter equipped with the standalone conventional optimum SLG

III. Configuration C: helicopter equipped with conventional baseline SLG and passive EA optimized for minimum acceleration

IV. Configuration D: helicopter equipped with conventional baseline SLG and passive EA optimized for full stroke

V. Configuration E: helicopter equipped with conventional optimum SLG and passive EA optimized for minimum acceleration

VI. Configuration F: helicopter equipped with conventional optimum SLG and passive EA optimized for full stroke,

VII. Configuration G: helicopter equipped with conventional baseline SLG and MREA, and

VIII. Configuration H: helicopter equipped with conventional optimum SLG and MREA.

To conduct non-dimensional analysis on the aforementioned models, the amplitude (R) was calculated numerically using Eq. (5.68) then substituted into Eq. (5.70) to determine the equivalent linear stiffness for the baseline and optimum SLG. The k_e values are calculated as 70469 and 66499 N/m for baseline and optimum SLG, respectively. In addition, the equivalent linear damping coefficient of the MREA was computed using Eq. (5.80) over the velocity up to 5 m/s as c_e = 303 N.s/m per single MREA. Thus, the overall equivalent linear damping coefficient for the four MREAs becomes equal to 8884 N.s/m. Using the second method the equivalent damping coefficient was calculated as 375 N.s/m with an overall equivalent damping coefficient of four MREAs of 9172 N.s/m. The difference between the above approximated damping coefficients is about 19%. The 9172 N.s/m equivalent linear damping coefficient will be used in the prediction of the behavior of the system in the event of impact. In addition, the SLG is treated as massless spring element due to its negligible mass compared to the helicopter mass and therefore, the only considered mass is the mass of the reminder structure of the helicopter lumped at the C.G. Table 5.1 summarizes these parameters that will be used in the analysis of the SDOF helicopter model. From the table, it is obvious that the difference in the stiffness of the springs will play a significant role is the determination of the dynamic response of different helicopter models.

5.7 Results and discussion

In this section, the non-dimensional responses of the three SDOF helicopter models are calculated and their performance in attenuating the impact force are assessed for the baseline and optimum SLGs.

Table 5.1. Parameters for the SDOF helicopter model.

Parameter	Designs A, C, E, G	Designs B, D, F, H
Overall equivalent elastic stiffness (k_e)	389085 N/m	295876 N/m
Helicopter mass (m)	2243 kg	
Impact velocity (v_0)	4.5 m/s	
Maximum permissible EA displacement (S)	200 mm	
Overall equivalent damping coefficient of MREA ($c_{e,all}$)	9172 N.s/m	

5.7.1 Optimum damping ratio of the passive energy absorber

The selection of the damping coefficient for the passive EA is of paramount importance in the mitigation of the shock loads for the particular helicopter model, as explained earlier. The displacement and acceleration responses of the passively damped system are normalized with respect to their respective peaks of the undamped SDOF model. The objective is to study the effect of damping ratio on achieving minimum acceleration and effective utilizing the available EA stroke. Unfortunately, passive EAs cannot fulfill these objectives simultaneously in a single optimum value of the damping ratio. Therefore, these objectives are dealt individually through design cases C to F over the damping ratio range $0 \leq \zeta \leq 1.0$ for $L = 1.0$ [18]. As a general sense, the high accelerative forces in the event of impact can result in severe injuries or death of rotorcraft occupants. Therefore, it is of paramount significance to maintain low acceleration levels. However, this might entail extending the damper's stroke beyond the available maximum permissible piston stroke that is imposed by the design and space constraints. Under this circumstance, the acceleration response will most probably be dominated by the end-stop impact and consequently very high acceleration on the occupant. This renders this choice of adjusting the damping ratio to comply with the requirement of minimum acceleration impractical and less favorite as will be demonstrated. However, determination of acceleration due to end-stop impact is out of scope of this dissertation and will not be discussed more. The utilization of the entire EA stroke while avoiding the end-stop impact, on the other hand, entails the damping coefficient be high.

Nevertheless, the consequence of experiencing higher damping force at the instant of contact is obvious, as will be demonstrated later in this section.

In Figs. 5.4 and 5.5, it is noticeable that the shapes of the corresponding non-dimensional displacement and acceleration curves are identical for baseline and optimum SLG models equipped with passive EA device. While the non-dimensional displacements keep decreasing with the increase in the damping ratio, ζ, the non-dimensional acceleration curves show different pattern. With the elastic spring assumption, the EA is the only energy dissipater. In this section, the reference acceleration values are taken as 59.23 and 51.7 m/s^2 for undamped designs A and B, respectively. By using the passive EA, the acceleration keeps decreasing with the increase in the damping ratio until the transmitted acceleration reaches minimum at an optimum value of the damping ratio, ζ. This point can be called the "turnover point". Beyond this point, i.e. when $\zeta > \zeta_{optimum}$, the stiffness of the EA device increases and as a consequence, the payload starts experiencing rise in the acceleration. For designs C and E, the non-dimensional accelerations were minimized to 0.81, i.e. 4.9 and 4.3 g's respectively by adjusting the damping ratios to 0.26 and 0.29. However, the end-stop impact is observed in both cases with theoretical non-dimensional displacements of 0.71 (24.0 cm) and 0.68 (26.6 cm). Both values exceed the maximum permissible stroke of 20 cm. to accommodate the 24% decrease in the stiffness of the optimum SLG compared to baseline design, the damping ratio of design E was increased by 11.5% over the design C.

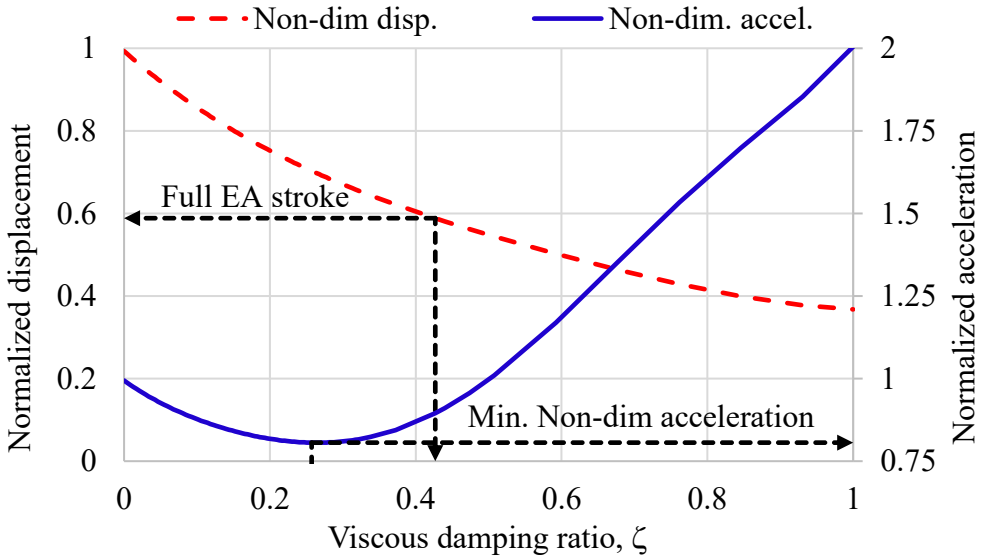

Fig. 5.4. Non-Dimensional displacement and acceleration response vs. viscous damping ratio for the helicopter equipped with the baseline SLG and passive EA at L = 1.0.

For configurations D and F where the objective is to utilize the full EA stroke, high accelerations were noticed. This is associated with high increase in the damping ratios of 65.4% for D and 96.6% for F compared to models C and E, respectively. This results in an undesirable increase in the corresponding accelerations form 4.9 and 4.3 to 5.4 and 6.0 g's. Though this bides to limiting the peak displacement at 20 cm, it has unfortunately risen the acceleration transmitted to the occupants. The discussion reveals that the requirements for minimum acceleration and utilization of full EA stroke are conflicting and could not be met concurrently by the passive EA devices as the two distinct values of damping ratio cannot be applied simultaneously. This renders

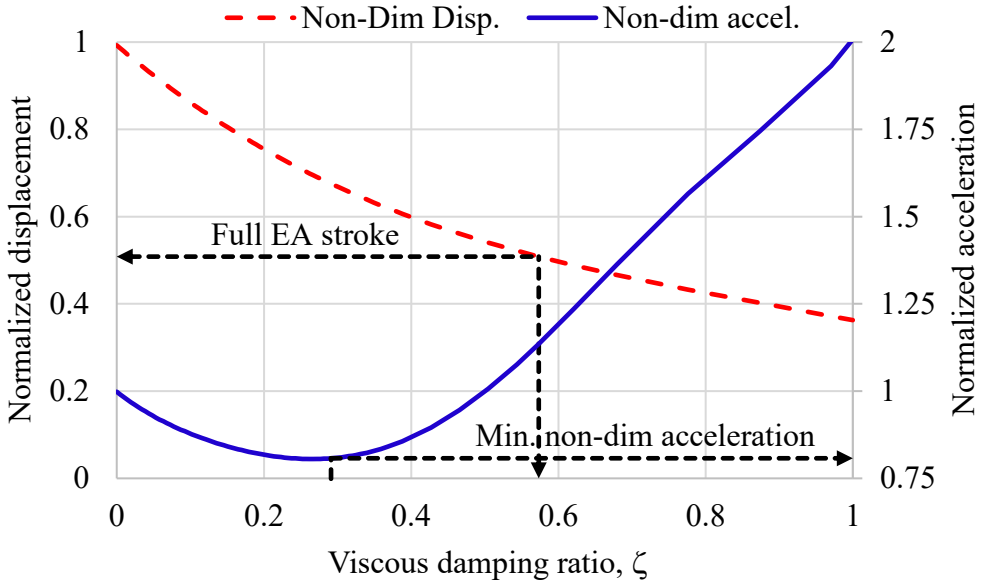

Fig. 5.5. Non-Dimensional displacement and acceleration response vs. viscous damping ratio for the helicopter equipped with the optimum SLG and passive EA at L = 1.0.

the device impractical from the perspective of the helicopter crashworthiness and necessitates incorporating the MREA with the conventional SLG system to successfully fulfill the above contradicting objectives. The key analysis results of the various configurations of the passive EA are summarized in table 5.2.

Table 5.2. Summary of key design results of the SLG equipped with passive EAs.

Parameter	Design C	Design D	Design E	Design F
ζ	0.260	0.430	0.290	0.570
$X(\zeta)/X_{max}$	0.700	0.600	0.680	0.510
$A(\zeta)/A_{max}$	0.810	0.900	0.810	1.140

5.7.2 Dynamic response of the helicopter model equipped with SLG and zero and passive damped EA

The responses of the helicopter models A to F are evaluated to assess the performance of the SLG systems in terms of non-dimensional displacement and acceleration at L = 1.0 and v_0 = 4.5 m/s. To establish a reference of comparison for the subsequent analysis, the displacements are normalized with respect to the maximum permissible EA stroke of 20 cm. in this context, fig. 5.6 shows that models C and E are infeasible solutions because their non-dimensional displacements exceeded the above maximum permissible even though they could hypothetically reduce the non-dimensional accelerations down by 30% for C and E compared to designs A and B, as shown in Fig. 5.7. Practically, the extended piston vertical travel results in the end-stop impact, which will highly likely expose the occupants to unsustainable peak acceleration loads. On the other hand, restricting the piston travel to 20 cm in models D and F has been fulfilled at the cost of the relatively high initial acceleration at touchdown, as explained in the preceding section. The restriction on the piston travel demanding higher damping ratio of the passive EA to compensate stroke shortage. The corresponding damping coefficients in this case are 25220 and 29540 N.s/m for models D and F, respectively.

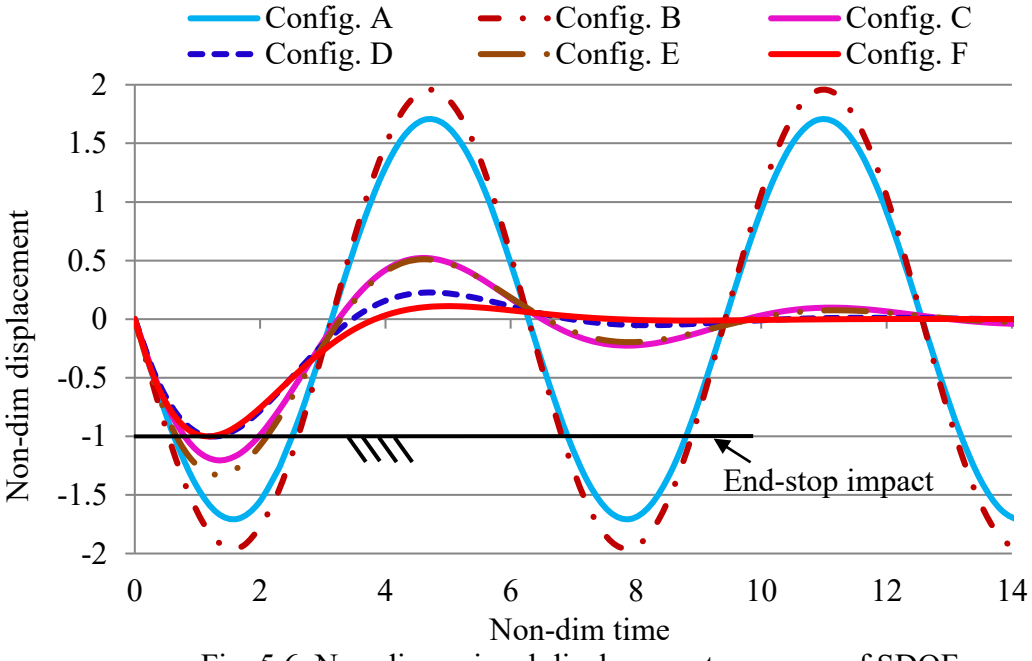

Fig. 5.6. Non-dimensional displacement response of SDOF helicopter model incorporating zero and passive dapmed EA.

Technically speaking, the passive energy absorber could not provide a compromised solution aims maintaining low acceleration level concurrently with avoiding the consequences of the end-stop impact. Therefore, the MREA is sought to be the promising device that can tackle the seemingly contradictory requirements as will be demonstrated in the next section.

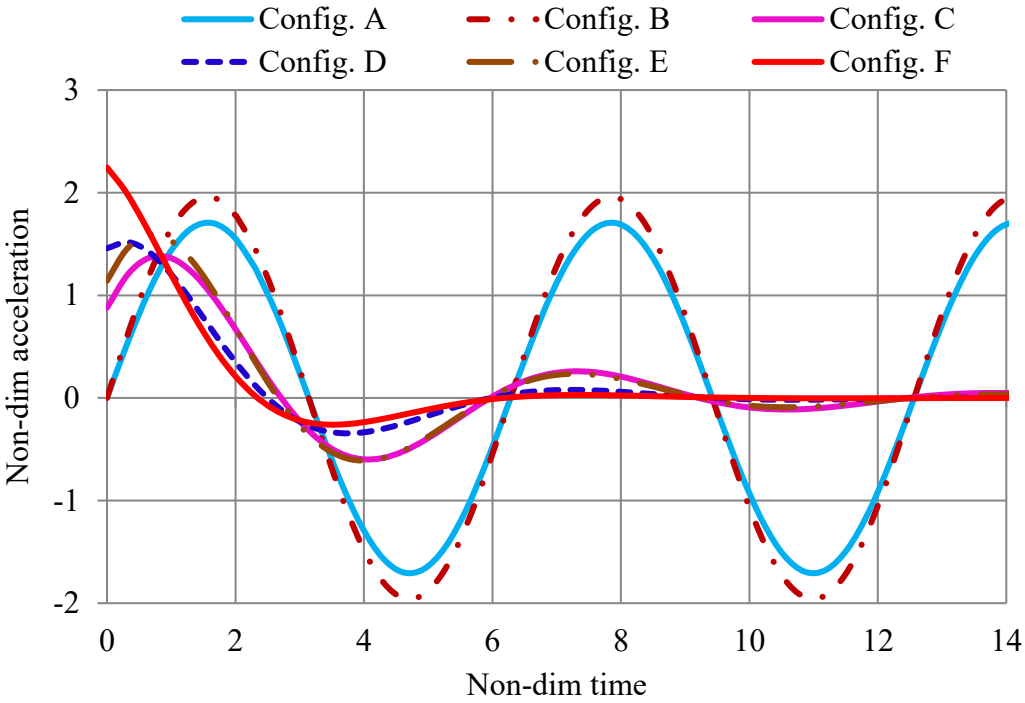

Fig. 5.7. Non-dimensional acceleration response of SDOF helicopter model incorporating zero and passive dapmed EA.

5.7.3 The chart of optimum Bingham numbers versus rotor lift factor

In this section, another contribution to the dissertation thesis is presented and discussed. It is all about expressing the optimum Bingham numbers for compression and rebound strokes in terms of the rotor lift factor in chart form known as $Bi^o - L$ chart. For helicopters equipped with SLGs and MREAs, one chart is developed per each model, i.e. models G and H, as shown in Figures 5.8 and 5.9. Using these charts, the optimum Bingham numbers at different sink rates can be easily determined as function of L. The MR yield force and the rotor lift load are normalized with respect to the field-off damping force and helicopter weight, respectively. These charts are very beneficial in the design of the semi-active control systems because the desired optimum MR yield force can be directly generated based on the measurement of the rotor lift force and then relate L to the optimum Bingham numbers according to the linear relation extracted for every impact velocity

during the loading and unloading strokes. To emulate the practical impact and to study the effect of variations of L, actual weight of the helicopter is used instead of the effective weight. The discussions in chapters two, three, and sub-sections 5.7.1 and 5.7.2 demonstrated that the conventional SLG and passive EAs could not dissipate impact energy effectively at high sink rates. The purpose of establishing the $Bi^o - L$ charts is to quickly determine the damping force required to dissipate the variably available impact energy at different impact speeds and loading conditions. This, protects the payloads from excessive acceleration loads and maintains the structural integrity around the occupants as well as of the SLG when the rotorcraft hits at a relatively high velocity. Another important reason is to accommodate the unexpectedly high impact energy when the proper amount of lift force is not activated at the instant of impact which may result in high impact loads. In the later case, the MREA is adapted to the event by generating the required damping force semi-actively. In these figures, it can be seen that the curves of the optimum Bingham number are inversely proportional with the rotor lift factor with high optimum Bingham number at low L. Low value of L means that high impact energy available at the contact instant. Therefore, the controller will instantaneously activate the MREA to generate the desired high damping force so that the consequences on the payload can be alleviated. Unlike the compression stroke, the optimum Bingham number for the rebound stroke is directly proportional with L. The slopes of the curves increase slightly with the decrease in the sink rate. In general, the optimum Bingham numbers for both strokes for velocities other than those plotted in the above two figures can easily be calculated by interpolating the consecutive curves. By generating the MR yield force according to the relations established from the charts the objectives of attaining soft landing at the end of the compression stroke and returning to the original equilibrium position at the conclusion of the rebound stroke are successfully fulfilled no matter what values of rotor lift force is intentionally or accidently generated. Thus, provides more protection to the helicopter occupants over a wide range of sink rates.

5.7.4 Dynamic response of the helicopter model equipped with bi-fold MREA

The dynamic response of the helicopter model incorporating both baseline conventional SLG configurations equipped with the optimized bi-fold MREA (design G) are graphed in figures 5.10 through 5.13. The shape of responses curves of the SLG comprising the optimum conventional structure and the bi-fold MREA are identical to those of design G. Therefore, the results of design

H will be numerically discussed and compared with G. By using fixed point iteration method, the optimum Bingham numbers for both systems were determined for L = 1.0, as tabulated in table 5.3. The table presents distinct optimum Bingham numbers for compression and rebound strokes for the analyzed G and H designs at sink rate of 4.5 m/s. Although the configurations G and H incorporate a MREA having same equivalent viscous damping coefficient, they generate different MR yield force so that optimum Bingham numbers due to their different responses. It is worth noting that with the generation of optimum Bingham numbers, soft landing is achieved, minimum acceleration is experienced by the occupants, and the payload returns to its original point of equilibrium at the end of the rebound stroke with no oscillations.

The response of design G is illustrated in terms of non-dimensional quantities: displacement, velocity, acceleration and the force for the following three sets of Bingham numbers:

Table. 5.3. Optimum Bingham numbers for two SLG configurations.

SLG system configuration	Bi_c^o	Bi_r^o
Baseline SLG + MREA (Design G)	1.1168	0.7146
Optimum SLG + MREA (Design H)	1.3533	0.5185

i) $\mathrm{Bi_c} = 0.5\ \mathrm{Bi}_c^o$ and $\mathrm{Bi_r} = 0.5\ \mathrm{Bi_r^o}$ (Underestimated),

ii) $\mathrm{Bi_c} = \mathrm{Bi}_c^o$ and $\mathrm{Bi_r} = \mathrm{Bi_r^o}$ (Distinct and optimum), and

iii) $\mathrm{Bi_c} = 1.250\ \mathrm{Bi_c^o}$ and $\mathrm{Bi_r} = 1.25\ \mathrm{Bi_r^o}$ (Overestimated)

The comparison of the above cases is intended to show the Superiority of incorporating the MREA with the conventional SLGs. The MREA can adaptably generate the desired damping force. The generated MR yield force can be expressed in terms of field-off damping force using the Bingham number (Bi). Referring to table 5.1, it is found that the single MREA can produce an off-state damping force of 10318.5 N at 4.5 m/s. Moreover, using the equation for FEMM provided in Fig. 4.22, it is found that the individual MREA device can generate 13476.5 N of MR yield force just prior magnetic saturation by activating the magnetic circuit with 2.6 Ampere. The dynamic range (D) in this case is 2.31. Hence, the corresponding maximum Bingham number is 1.31. This sets the upper limit at which the MREA can work effectively. However, when the helicopter impacts with vertical velocity higher than 4.5 m/s, then the MREA will no longer be able to work

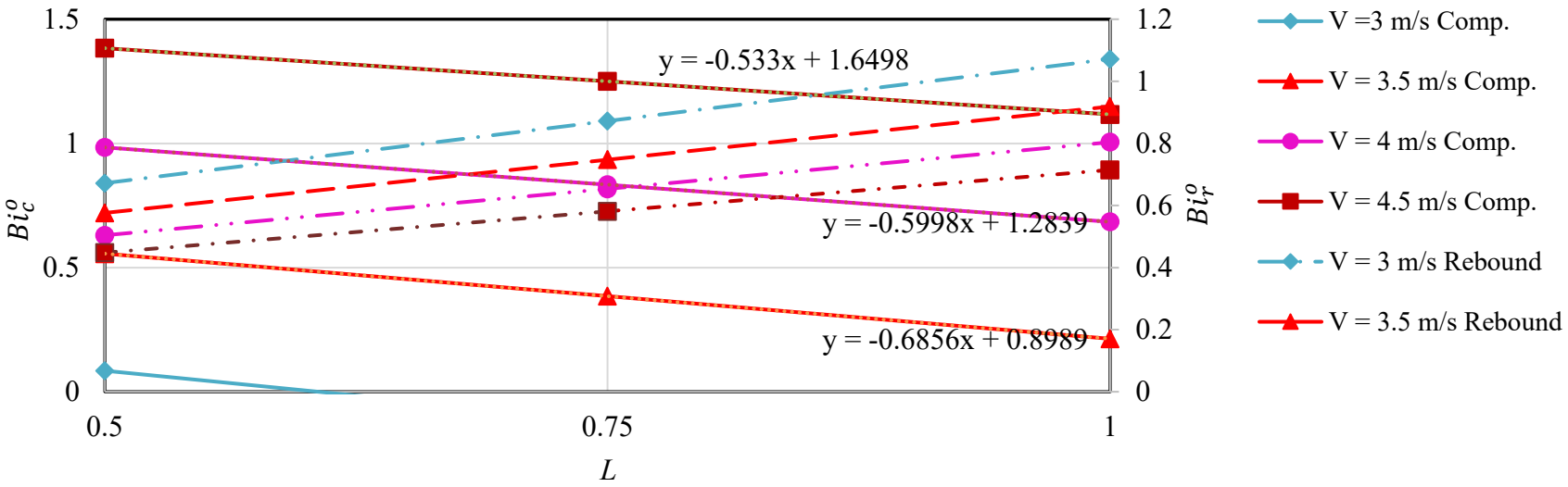

Fig. 5.8. Bi^o-L curve for different sink rates for model G.

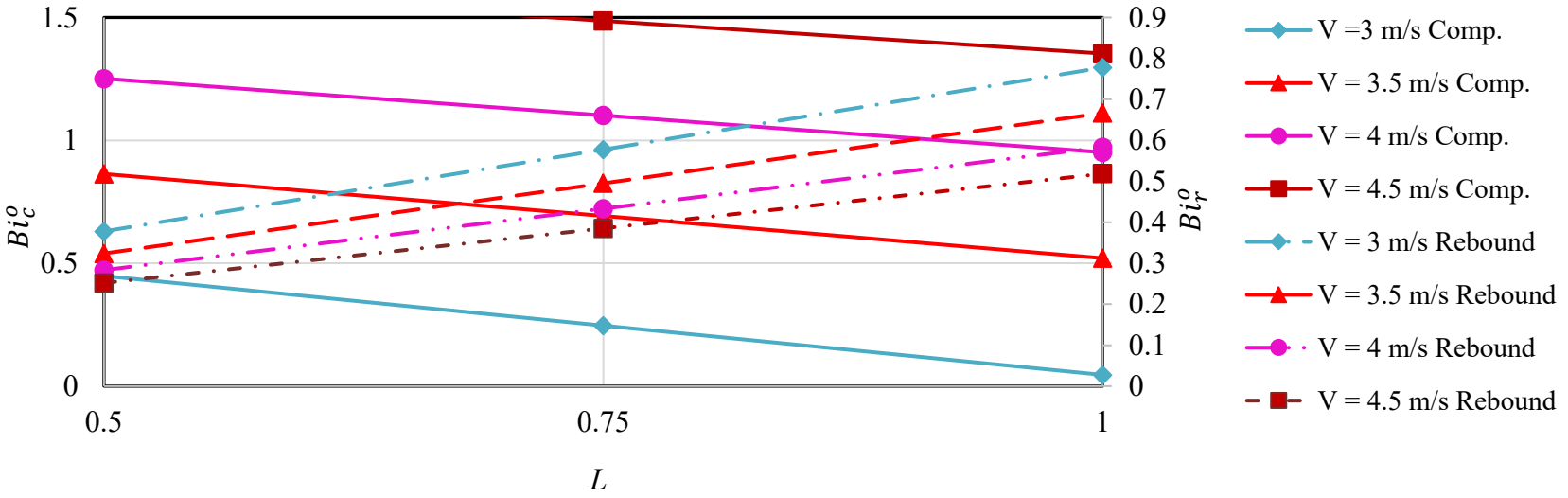

Fig. 5.9. Bi^o-L curve for different sink rates for model H.

effectively in dissipating the substantial amount of energy. In this case, the excessive energy will be dissipated by a simultaneous crush of the fuselage subfloor structure and by the occupant seat.

In Fig. 5.10, it can be seen that when the Bingham number for compression stroke of design G is underestimated, the generated yield force is insufficient and the solution becomes infeasible with an increase in the non-dimensional displacement of 17% (3.4 cm) over the maximum permissible EA stroke of 20 cm. Unfortunately, this results in the end-stop impact and degrades the performance of the system in attenuating the acceleration loads. In the second half of the cycle (the rebound stroke), the payload is overshot above the original equilibrium point to new non-dimensional equilibrium position of 0.41 (8.2 cm) due to the insufficient damper force. This renders the described MREA unreliable from the perspective of crashworthiness. On the other hand, when the overestimated Bingham numbers are considered, the MREA generates inadmissibly higher than optimum damping forces in both strokes. In this case, the MREA dissipates more impact energy in a relatively short compression stroke (about 7% shorter than the full EA stroke). Therefore, no soft landing is attained. In the rebound stroke, on the other hand, the payload is repositioned to new non-dimensional equilibrium reference of 0.195 (3.9 cm) below the original equilibrium position. The generated MR force is higher than the spring restoring force. Therefore, it prevents the full return of the payload to its initial equilibrium point. With the Bingham numbers set optimum and distinct, the soft landing is attained at the end of the compression stroke. Moreover, the model returned smoothly and with no post-impact oscillations to its original equilibrium position at the end of the rebound stroke, as shown in the figure. Figure 5.12 depicts the non-dimensional time history of the acceleration experienced by the payload. During the course of loading stroke, the payload in the underestimated case (*i*) is subject to the least acceleration of 1.54 or 5.4 g's which is associated with minimum jerk as well (the jerk is shown as a step change in the acceleration due to sudden change in the slope of the velocity as shown in Fig. 5.11). At the end of the rebound stroke, the second low magnitude jerk is noticed due to the change in the direction of the velocity as Fig. 5.11 illustrates. For the overestimated case, the payload experiences non-dimensional acceleration of magnitude 1.76 (6.2 g's) in the course of compression due to the increased stiffness of the MR fluid. This results in high jerk at the end of the compression stroke. In the rebound stroke, the spring's restoring force could not overcome the high MREA damping force and the least jerk is encountered as the momentarily

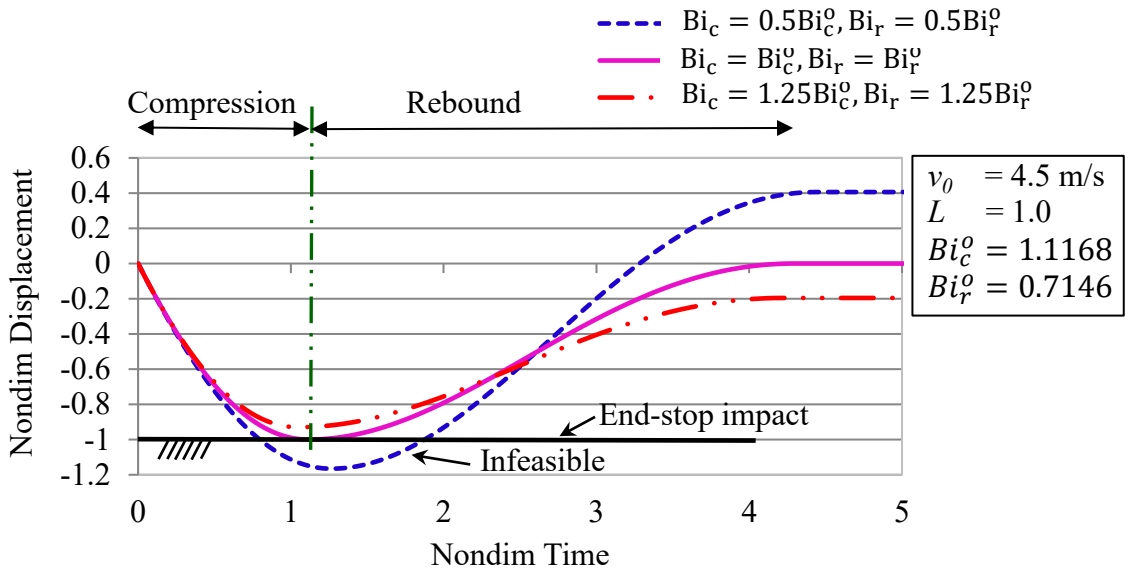

Fig. 5.10. Non-dimensional displacement of SDOF helicopter model equipped with bi-fold MREA.

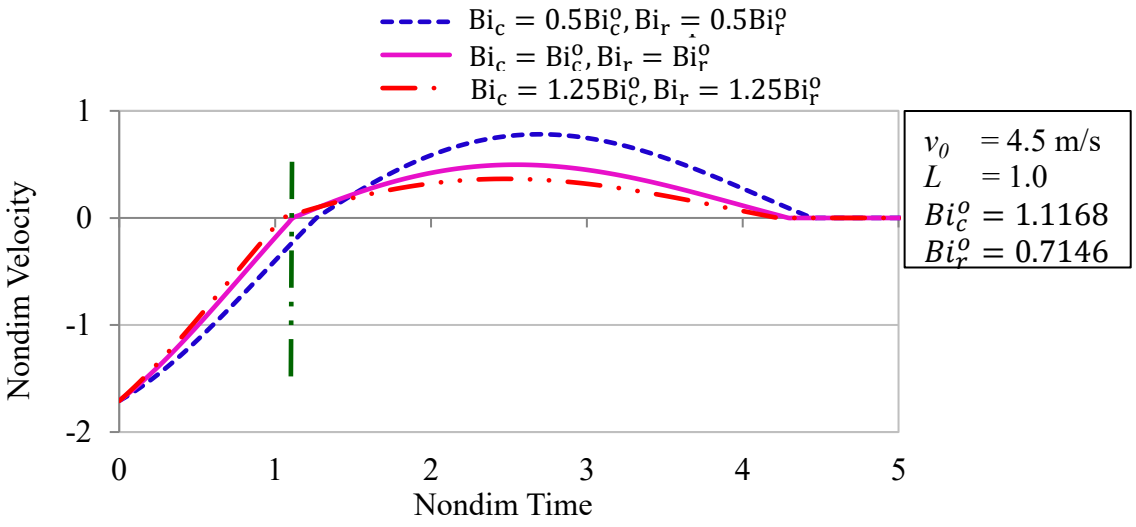

Fig. 5.11. Non-dimensional velocity of SDOF helicopter model equipped with bi-fold MREA.

change in the velocity direction is very slow due to the high stiffness of the MR fluid (shown as low change of velocity from the compression to rebound stroke in Fig. 5.11). At the end of rebound stroke, the model experiences an acceleration of nearly 1 g as it comes to complete stop with incomplete recovery of the stroke. The optimum behavior of the payload is observed with the optimum Bingham numbers for compression and rebound strokes. The occupants experience maximum non-dimensional acceleration of 1.68 during the compression stroke which results in

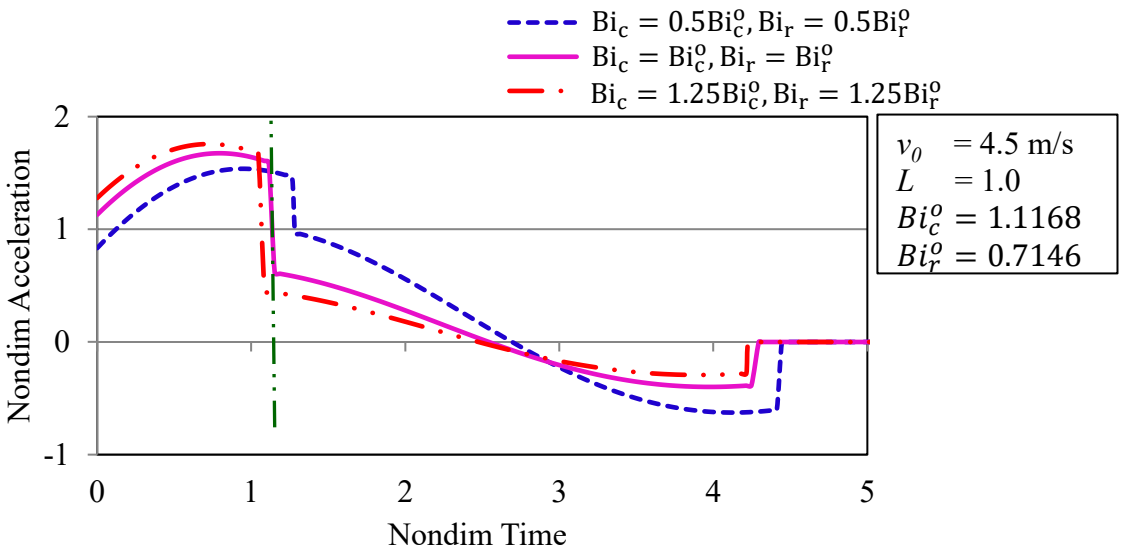

Fig. 5.12. Non-dimensional acceleration of SDOF helicopter model equipped with bifold MREA.

moderate jerk. The soft landing is achieved by the end of this stroke. the optimum MR force in the rebound stroke insured a smooth return of the payload to its equilibrium position at initial contact with no further oscillation.

Figure 5.13 depicts the variations in the non-dimensional force on the payload. The force is plotted against the non-dimensional displacement for the above three sets of Bingham numbers. The figure shows that for the underestimated condition, the solution is infeasible due to the end-stop impact as a consequence of low damping force. Hypothetically, the system experiences low force in this case due to the extended compression stroke beyond maximum permissible. For the overestimated Bingham numbers, the relatively high non-dimensional force experienced in the compression stroke is attributed to the high Bingham number. The distinct and optimum Bingham numbers for the compression and rebound strokes are found to be the only solution to fulfill the objective and compromise the requirements of experiencing sustainable force and the obligation of avoiding the end-stop impact.

The same discussion and conclusions can be projected on the three similar cases of model H. However, low stiffness of the optimum conventional SLG decreases the amount of elastic energy absorbed by the crosstubes. This entails that the MREA should produce more damping force to dissipate the excessive impact energy as shown in table. 5.3. In this condition, the required

Bingham number for compression is 1.4186 which is slightly higher than the maximum capability of the MREA. This means that the evaluation is restricted to the responses determined for Bingham numbers less than or barely equal to the optimum ones. Table 5.4 compares the results of analysis for cases (*i*) and (*ii*) for designs G and H at the end of each stroke.

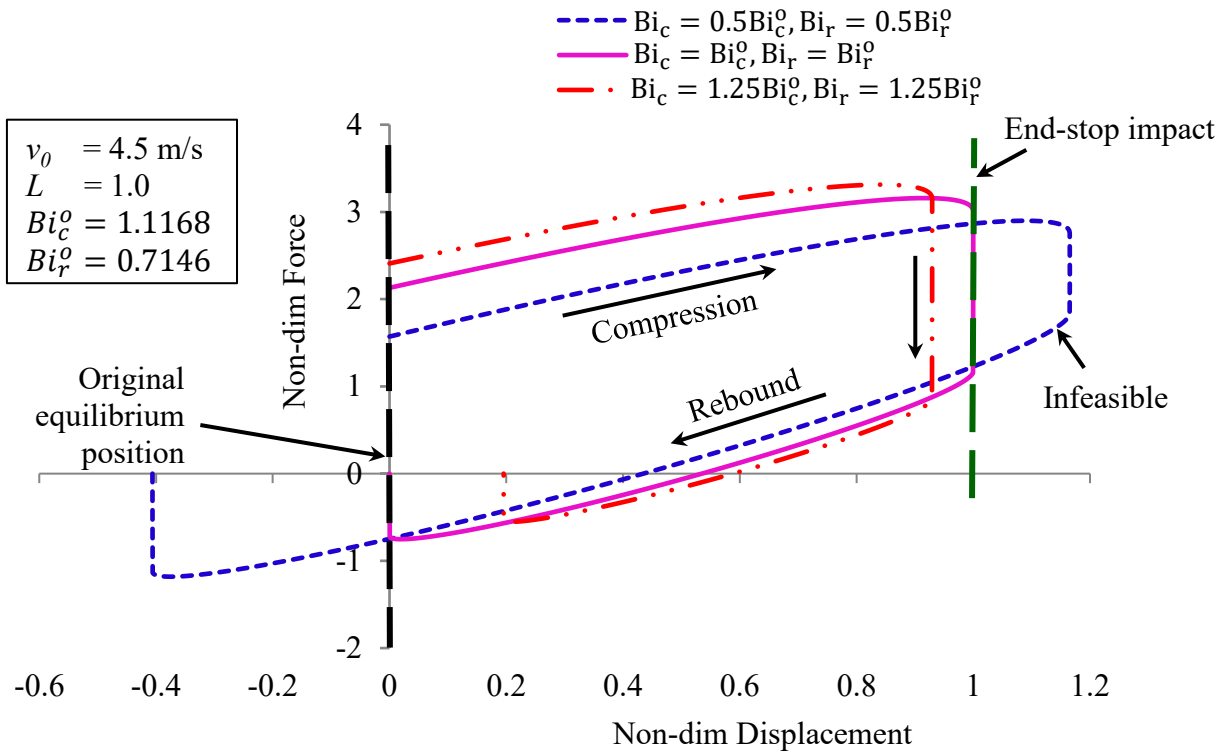

Fig. 5.13. Non-dimensional force vs. non-dimensional displacement for SDOF helicopter model equipped with bi-fold MREA.

Table 5.4. Peak non-dimensional responses of Configuration G and H.

Peak non-dimensional response	Configuration G				Configuration H			
	0.5 Bi_c^o	Bi_c^o	0.5Bi_r^o	Bi_r^o	0.5 Bi_c^o	Bi_c^o	0.5Bi_r^o	Bi_r^o
Displacement	-1.17	-1.0	0.406	0	-1.22	-1.0	0.41	0
Acceleration	1.54	1.68	0	0	1.81	2.09	0	0

5.8 Summary

In the present chapter, an extensive study on the helicopter is carried out using single degree of freedom models. Several designs of the skid landing gear were considered and analyzed. The single degree of freedom modeling serves as a good and a minimum cost predictor of the

helicopter's response in the event of impact. The comparison of the zero and passively damped models reveals that the helicopters equipped with the standalone conventional SLG in designs A and B were vulnerable to displacements beyond the allowable stretch of the stroke. This conclusion is also applied to systems designed to attain minimum acceleration using passive energy absorbers in configurations C and E although their non-dimensional acceleration responses were hypothetically reduced. On the other side, when the passively damped systems in D and F were tuned to not exceeding the maximum EA stroke, acceleration increased especially for model F which has less spring stiffness. The passive EAs are mono-mode objective devices rather than multi-mode category. Therefore, they cannot adapt to the variations in the impact scenarios. The poor performance of the conventional SLG and the SLG equipped with the passive EA device at could significantly be improved by incorporating the bi-fold MREA devices. The MREA could attenuate the impact load to reasonable levels without exposing the occupants to sudden increase in the acceleration as it dissipated the impact energy efficiently and prevented the end-stop impact. The MREA can be tuned to meet broader range of energy dissipation requirements in order to fulfill the crashworthiness objectives. The performance of the MREA is indexed in terms of the Bingham numbers of compression and rebound strokes. New charts were introduced in this chapter which relate the optimum Bingham numbers to the variation in the rotor force factor, or simply the Bi^o-L chart. This objective is to facilitate the mission of the semi-active controller by providing it with the updates loading on the helicopter which considers the activated rotor lift force at touchdown. For the considered three verification sets of the Bingham numbers, the analyses ascertained that the optimum and distinct Bingham numbers for impact and rebound strokes could meet the requirements set at the beginning of the chapter as the non-dimensional acceleration responses were fairly maintained low without exceeding the maximum preset piston stroke.

CHAPTER 6
Semi-Active Control of the SLG System

6.1 Introduction

The importance of semi-active control system in mitigating the undesirable dynamic responses in the event of harsh landing and crash is described briefly in the present chapter followed by description of two control strategies used in SLGs equipped with MREAs; namely, the constant stroking load regulation policy and the adaptive control scheme based on the optimum Bingham numbers for compression and rebound stroke. While the passive EA controls the generation of the damping force by sizing the valve based on the impact condition of maximum sink rate and mass, the semi-active control system tunes the rheological properties of the MR fluid in the MR gap in the real time to achieve the optimal performance over a wide range of impact velocity [82]. In this chapter, the relationship between the input current and the sink rate is developed for use in the inverse model to automatically generate the desired MR force. In the crashworthiness of helicopter's SLG, the objective is to minimize the transferred peak accelerations to the payload and to extend the fatigue life of the crosstubes as well. The subsequent section describes how the semi-active control system can be practically implemented in the helicopter's SLG system when it is equipped with the MREAs.

6.2 Semi-active control system for helicopter's SLG equipped with MREA

The vulnerability of the helicopter to high impact loads raises a big concern for the occupant's safety. Therefore, impact loads have to be mitigated in a controlled manner to assure subjecting the occupants to tolerable level of acceleration. To achieve this objective, the vertical energy absorbing capabilities are integrated at three locations, the landing gear, the sub-floor structure, and the occupant seat. The passive EAs have proven unfit to accomplish these tasks, as demonstrated in the preceding chapter. On the other hand, despite the fully active control systems have proven to be very efficient in providing the desired protection and minimized the transfer of the detrimental shock loads in the event of impact, their limitations such as the increased cost, complexity, high power requirement, and the instability of the actuator due to the failure of the controller have limited their use in SLGs as they may result in a catastrophic turnoff [76-80]. In

lightweight helicopters, the energy dissipation capabilities of the skid gears can be further enhanced by incorporating semi-active devices such as MREAs which are having the reliability of the passive system yet maintaining the adaptability of the fully active system. However, the compactness of the MREA to fit in the allocated volume should be confirmed without compromising the performance of the MREA device. The merits of the semi-active control systems over the passive and fully active control systems have made them feasible and practical solution. To successfully employ the semi-active control system in the helicopter skid gear to attenuate the impact loads, the following challenges should be carefully addressed [69, 80]:

i) Duration of the impact. The impact is typically very short-time event and lasts 50 to 200 milliseconds,
ii) Device compactness and lightness. The MREA should be as compact as possible to fit in the allocated space and be light in weight yet strong enough to withstand high loads.
iii) Adaptability and continuity in load generation. The system should be capable of varying the generated damping force based on the variation in the mass and the velocity of impact.

The MREA based semi-active control system is schematically presented in Figure 6.1. The system consists of two controllers; the system controller and the damper controller [19]. The system controller produces the required damping force based on the dynamic response of the model (plant). The damper controller, on the other hand, varies the input current to the MREA device to ensure that the generated damping force is regulated in the real time with the desired one according to the control algorithm The system constitutes of four MREAs. The sensors sense different parameters such as height and velocity and transmit them to the system controller to generate the required damping force accordingly.

The practical implementation of the semi-active control system is based on Figure 4.4. As the helicopter approaches ground, the attitude of the helicopter is continuously monitored using the gyroscopic sensors to determine at what attitude the helicopter will hit ground to activate the corresponding MREAs. For instance, when the attitude is level, then all the four MREAs will be activated, whereas for impact at pitched up nose, the two rear MREA will be activated. Conventionally, the sink rate is estimated using the altimeter. The most modern and more accurate

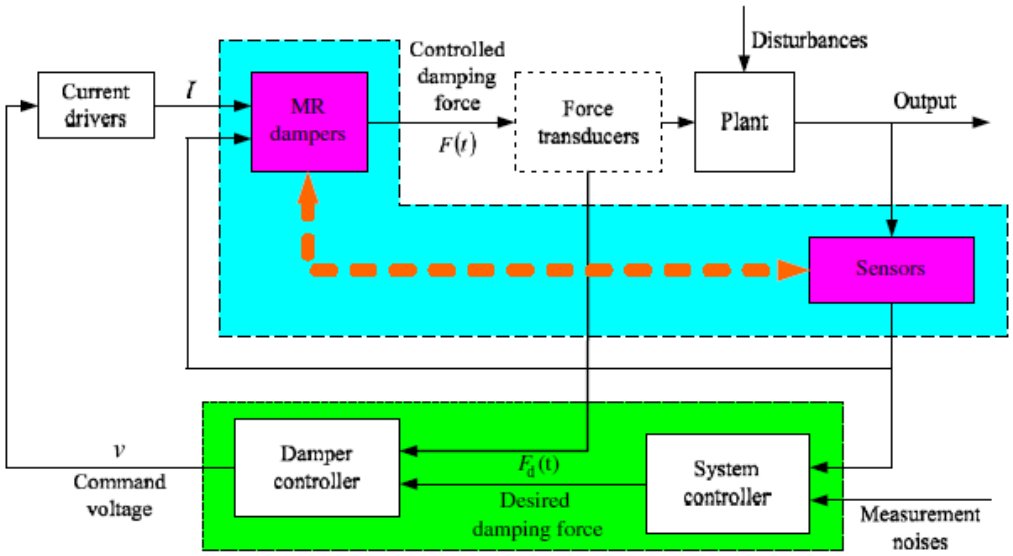

Fig. 6.1. schematic of the MREA-based semi-active control system [19].

method is to use instruments such as low power radar, ultrasound or photo laser sensors [82]. The helicopter mass can be estimated by storing takeoff data such as the payload (occupants and structure weight) and the mass of fuel in the tank. Since the fuel in the tank is calculated in real time by the helicopter instrument, the consumed fuel can be subtracted from the takeoff weight so that the exact helicopter mass at the instant of impact can be computed. In addition, the pilot can use the collective control to change the pitch of the main rotor blades in order to generate the rotor lift force at touchdown. Based on the above stored data, which are estimated at the contact between the skids and the ground, the anticipated initial current input is determined by the system controller and the signal is sent to the MREA through the command voltage and the current driver to produce the optimal controllable damping force in addition to the field-independent damping force at touchdown. As the compression stroke progressing and the energy is dissipating, the sensors measure the relative position between the MREA's cylinder and piston in addition to the relative velocity and send these readings back to the controller. The controller compares the readings from the feedback signals with the desired ones and adjusts the input current accordingly so that the generation of the optimum damping force continues until attaining soft landing (at the maximum permissible compression stroke). From this point forward, the rebound stroke begins. Since the elastic energy stored in the crosstubes is known and constant with all optimum Bingham numbers ($\frac{1}{2}k_{e,all}S$), the initial input current at the beginning of the rebound stroke is always constant no

matter what the impact velocity is. As the helicopter rebounds, the measured responses of the helicopter are compared to the instantaneous desired optimum and adjusted accordingly until the stroke is concluded and the helicopter is resettled to the initial point of equilibrium without encountering oscillations. At this moment the velocity and acceleration are zero. This ensures that the optimum damping force is generated throughout the rebound stroke by generating the desired input current which is calculated based on the measurements of the velocity, mass, and L.

6.3 Semi-active algorithms for the helicopter's SLG equipped with MREA

Unlike the low speed applications, the high velocity impacts can cause severe injuries or potential fatalities when the helicopter occupants incur excessive accelerative loads above their tolerable levels. In addition, maintaining a positive clearance between the fuselage and the impacting surface is very desirable to keep the fuselage intact and to provide the required livable volume around the occupant so that the height of the cockpit and compartment is not reduced by more than 15% of the original height [7]. In compliance with the crashworthiness regulations, however, the skid landing gear is allowed to deform plastically to absorb kinetic energy. Moreover, when the MREAs are integrated with the conventional SLG structure, it is important to ensure that the distance travelled by the payload does not exceed the maximum permissible stroke of the EA, which is a design specification, to avoid bottoming out or end-stop impact. Considering this, a suitable semi-active control strategy that can fulfill these objectives in addition to dissipating tremendous amount of impact energy during the compression-rebound cycle, as explained in Chapter five, is required. The above design conditions can be expressed mathematically as

$$\ddot{x}_{max} \leq \ddot{x}_{pemissible} \quad \text{and} \quad x_{max} < x_{end-stop} \tag{6.1}$$

In the following subsections, two control algorithms developed for semi-active skid landing gears are discussed in some detail.

6.3.1 Constant stroking load regulator

Every payload mass can accommodate a maximum limiting stroking load depending on the impulse profile and the excitation level. The constant stroking load control policy is proposed in [81] to bring the payload to rest at the instant when the available stroke is fully utilized without encountering end-stop impact, i.e. soft landing. The scheamtic representation of the damping

force-velocity profile for the constant stroke control startegy is shown in Fig. 6.2. In the developed control strategy, four different acceleration profiles of the shock signal are stored in the system. Namely, triangular, half-sine, square, and combination of the above profiles. The acceleration profile is pre-selected. Just prior to the impact, the duration of the acceleration pulse is anticipated based on the acceleration profile and the measured impact velocity. Using this information, the peak acceleration is determined. By estimating the payload mass at contact and using the calculated acceleration, the external (impact) force on the payload, the left hand side of Eq. (6.2), is computed. By assuming that the EA stroke is fully utilized and L is known at the instant of contact, the desired stroking load, F_y, is determined as:

$$\ddot{x}(t) = \frac{-1}{m}[c\,\dot{x}(t) + k\,x(t) + f_y\,sgn\{\dot{x}(t)\} + mg\,(1 - L)] \tag{6.2}$$

where m is the payload mass, and k is the elastic stiffness (equivalent) of the conventional SLG. F_y is the stroking load. The current signal can be varied to adjust the yield force. To maintain stroking load constant, the adjustment of the yield force compensates the contribution of the passive component of the damping force. This can be achieved by implementing the classical on-off control ploicy. The input current in this case can be expressed as [69]:

$$I = \begin{cases} X\,A, & if \quad (\varepsilon F_y - F) > 0 \\ 0\,A, & if \quad (\varepsilon F_y - F) \leq 0 \end{cases} \tag{6.3}$$

where X is the magnitude of the input current signal and ε is the gain control.

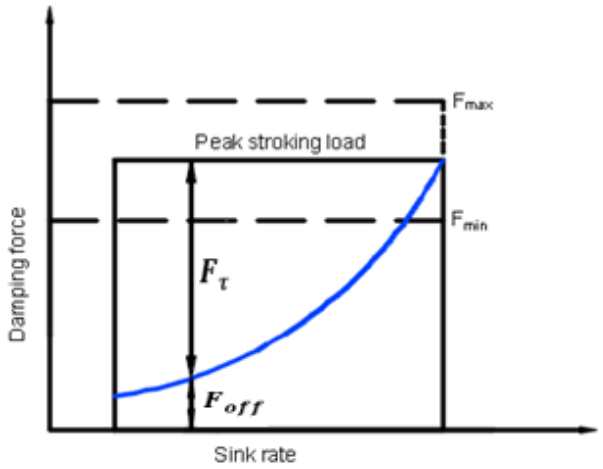

Fig. 6.2 Damping force vs. velocity for constant stroking load control policy.

6.3.2 Semi-active control based on the optimum Bingham numbers

Although the above control policy permits attaining soft landing during the compression stroke, the occupants may experience highly undesirable acceleration loads during the rebound stroke because the stroking load is maintained constant throughout the loading/unloading strokes [83]. The constant stroking load control strategy can be further improved by optimizing the Bingham numbers for both compression and rebound strokes, as demonstrated in Chapter five. Here, a semi-active control strategy can been implemented to fulfill the objectives of minimizing the acceleration loads on the occupants and attaining soft landing without incurring end-stop impact at the completion of the compression stroke. Furthermore, ensuring the return of the payload back to its equilibrium position at the end of the rebound stroke. To do so, an inverse dynamic model was first developed to represent the relationship between the applied current and the sink rate are developed for helicopter configurations G and H. Using formulation in Chapter 5, the expressions of current in terms of sink rate (range is from 3 to 4.5 m/s) in the compression stroke can be written as:

$$\text{Configuration G: I} = 0.748\, v_0^2 - 4.5532\, v_0 + 6.9293 \quad \text{(A)} \tag{6.4}$$

$$\text{Configuration H: I} = 0.7546\, v_0^2 - 4.2406\, v_0 + 5.9731 \quad \text{(A)} \tag{6.5}$$

The role of the MREA in the rebound stroke is to return the payload mass to its original equilibirum point by controlling the release of the energy stored in the spring during compression stroke. Thus, the values of the input current at the biginning of the rebound strokes of both designs is constant no matter what the impact velocity is. It, therefore, can be computed as

$$\text{Configuration G: I} = 0.8285 \ \text{(A)} \tag{6.6}$$

$$\text{Configuration H: I} = 0.5922 \ \text{(A)} \tag{6.7}$$

The computed current is then used to determine the required yield force using yeild force-current relations (4.40) and (4.41).

MATLAB Simulink was used to study the dynamic behavior of the SLG and the MREA during the impact. In the model, the damping coefficient and the stiffness of the spring are conisdered to be the equivalent linear quantities as evaluated in the preceding chapter. The schematic diagram of the semi-active control system is illustrated in Figure 6.3. It is worth noting

that the developed control strategy does not require storing the acceleration profiles in the system like in [81]. It rather generates the damping force based on the measured sink rate and the payload mass. This makes the present control system more adapatable and accurate as it avoids the error of estimating the acceleration profile. In the present control scheme for configuration G, for example, every individual MREA can generate passive damping force of 10318.5 N the touchdown at velocity 4.5 m/s. Since the optimum Bingham number for compression stroke is 1.1168, the controllable damping force becomes 11523.7 N. Therefore, the total desired damping force at skid-ground contact is nearly 21842.2 N. After touchdown, the controller adjusted the value of the input current as the process of energy dissipation continues until the system comes to temporary stop at the conclusion of the compression stroke. When the MREA piston reverses it direction at the start of the rebound stroke, the values of the current signal is equal to those given in Eqs.(6.6) and (6.7) based on the SLG configuration. The closed feedback loop circuit adjusts the input current instantaneously until the system comes to complete rest at the end of the optimum rebound stroke where the helicopter C.G. returns to its initial point of equilirum. Table 6.1 compares the initial current input and initial damping force generated by the MREA at the beginning of each stroke in Configurations G and H per single MREA per stroke at impact velocity of 4.5 m/s and L = 1.0.

Table. 6.1 Initial input parameters of the semi-active control system based on Bingham numbers.

Configuration	Current, A	Yield force, N	Desired stroking load, N
G	1.59 (Compression)	11523.7	21842.2
	0.83 (Rebound)	7373.6	17692.1
H	2.187 (Compression)	13153.0	23471.5
	0.6 (Rebound)	5350	15668.5

Using the Eqs. (6.4) and (6.5), the desired initial input currents are found for the given sink rate for Configurations G and H. Figure 6.4 shows the variation of the desired initial input current versus sink rate. From the figure it can be realized that the current demand increases nonlinearly with the increase in the impact velocity for both configurations with more demand for model H. Also, at velocity of 3 m/s the magnetic field is not activated in both model. This means that the impact load is relatively low and can be dissipated by the field-off stroking load. Moreover, the increase in the input current demand of model H over G is attributed to the relatively low stiffness

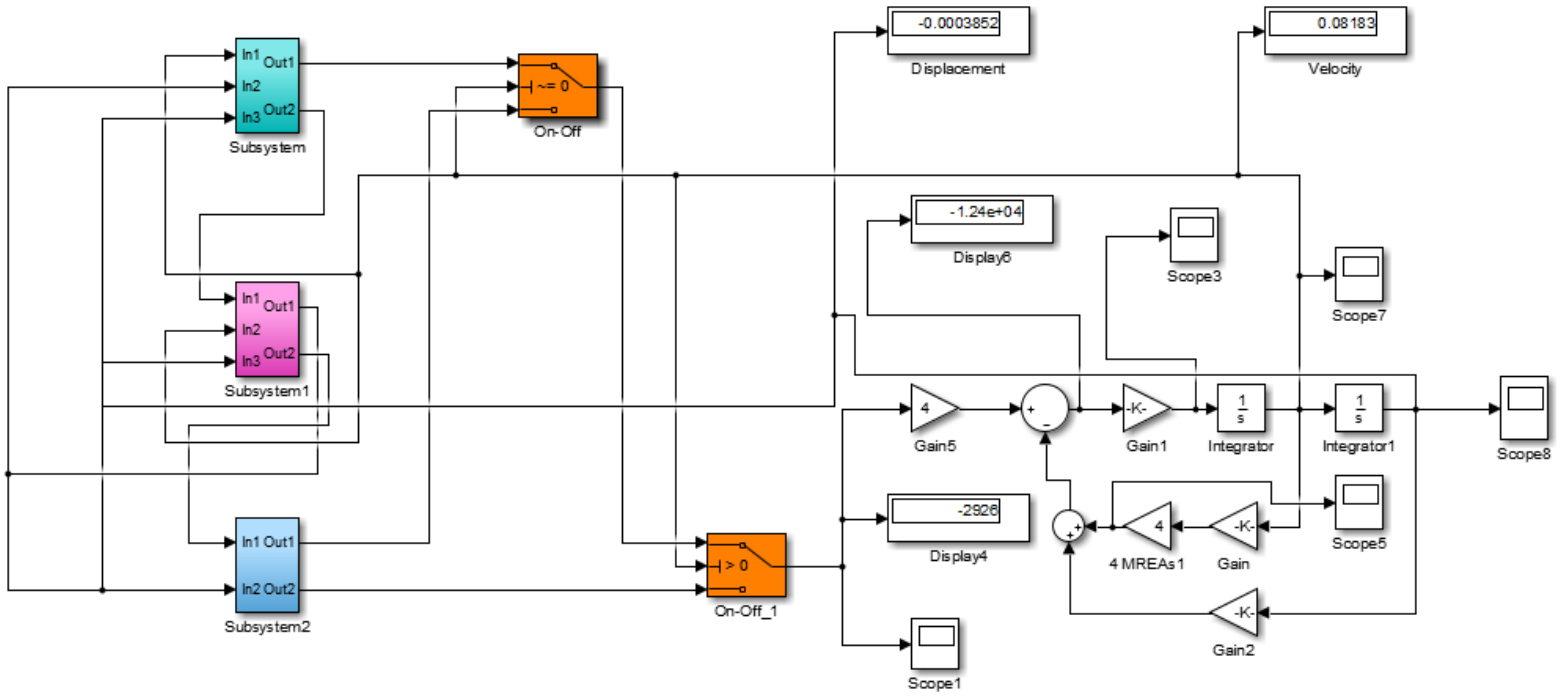

Fig. 6.3. Block diagram of semi-active control system for SDOF helicopter model.

of the optimum SLG compared to the stiffness of the baseline configuration in which the former absorbs and stores less elastic energy within the identically traveled strokes. The dimensional displacement and acceleration responses of the helicopter configurations A, C, E, and G are presented in Figures 6.5 and 6.6.

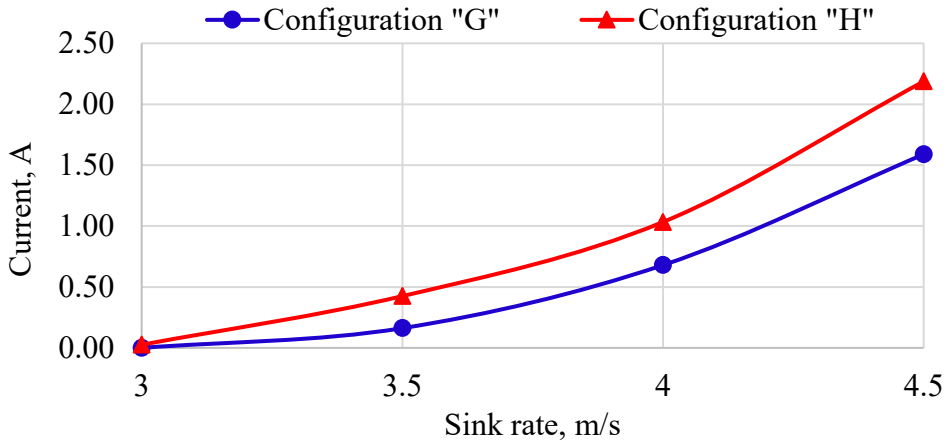

Fig. 6.4. Current vs. sink rate for compression strokes.

In Figure 6.5, it can be seen that only the helicopter configurations E and G utilized the entire stroke and attained soft landing. However, configurations A, C, and E continued oscillating after one cycle, as the same figure depicted. Under the particular condition of v_0 4.5 m/s and L =1.0, the peak acceleration experienced by configuration A (undamped) could be decreased from 60 m/s^2 to 56 m/s^2 s (configuration G). Although the reduction in peak accelration is slightly more (~ 8%) when the damping coefficient of the passive EA was adjusted to utilize the full EA stroke, it is obvious that the helicopter returned to its original point of equilibirum after only one cycle with the MREA. On the contrary, the helicopter continued to oscillate when the passive EA incorporated into the SLG instead of the MREA. Practically, this would cause the occupants to experince the post-impact vibrotion loads. Furthermore, in real situations, the helicopter will bounce off the ground and hits the ground for the second impact. This, however, would have detrimental effect on the passengers and helicopter crew.

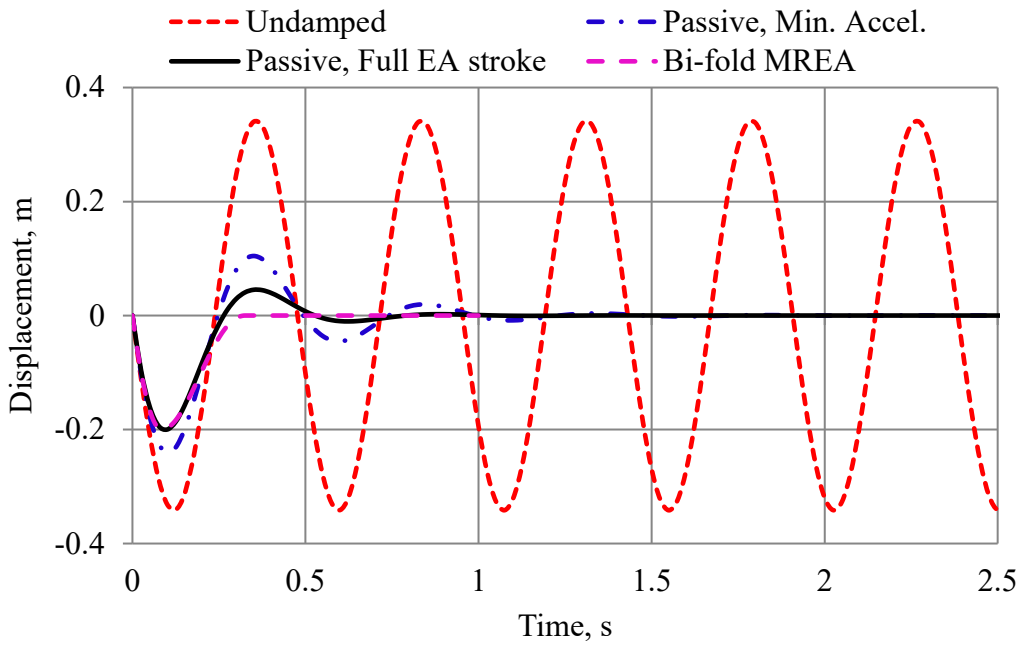

Fig. 6.5. Displacement time history of SDOF helicopter model G equipped with SLG and bi-fold MREA.

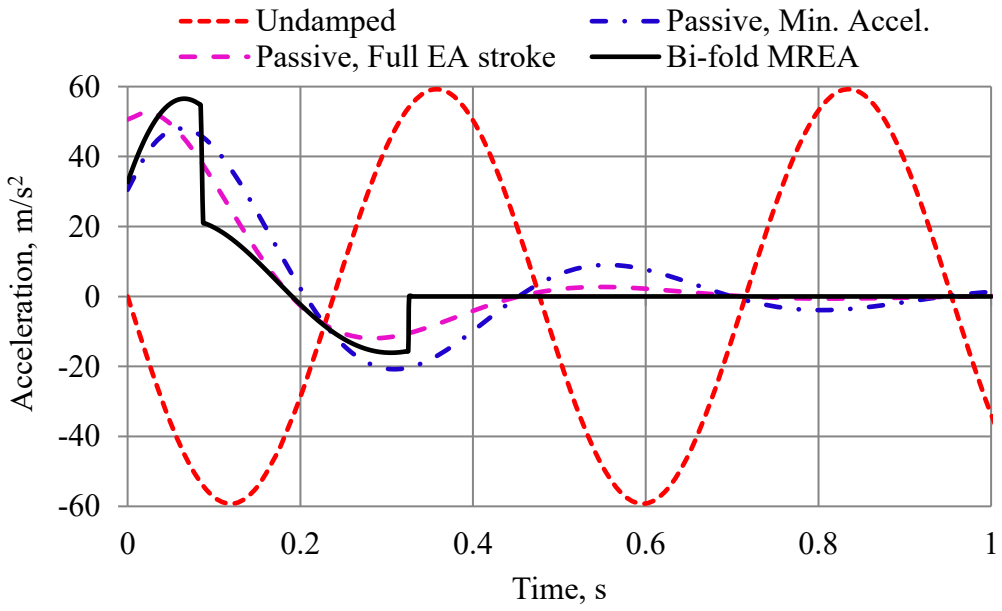

Fig. 6.5. Acceleration time history of SDOF helicopter model G equipped with SLG and bi-fold MREA.

6.4 Summary

In this chapter, a brief description of the semi-active control strategy is presented and two control systems suitable for use with the helicopter equipped with skid landing gear systems is discussed in more detail. Namely, the constant stroking load and the adaptive control system based on the optimum Bingham numbers. Two inverse models were developed to determine the required input current according to the impact velocity and the required MR damping force based on the determined current. The dimensional displacement and acceleration responses of the helicopter equipped with baseline and passive EA and with MREA were compared. It can be seen from the plots that the MREA could attenuate impact force in a single cycle to avoid exposing the occupants to post impact vibration loads while the soft landing was attained at the end of the compression stroke. Moreover, at the end of the rebound stroke, the helicopter returned to its initial point of equilibrium.

CHAPTER 7

Conclusions, Contributions, and Future Recommendations

7.1 Conclusions

Providing safety to helicopter occupants in the event of harsh impact and crash is a challenging task and is of paramount importance to the helicopter industry. Among the three crashworthy systems of lightweight rotorcrafts, the skid landing gear is intended to dissipate about half the impact energy. However, due to its structural simplicity and inadequate strength, the conventional skid gear cannot handle this task at high impact velocities because it dissipates energy through the plastic deformation. On the other hand, the incorporation of passive energy absorbers is effective when the rotorcraft impacts at the design condition of maximum velocity and mass. Its performance drops drastically and the device is rendered impractical when the helicopter impacts at conditions different from the designed ones. Therefore, to overcome the drawbacks of the above mentioned devices and to assure that the potential energy dissipation device fits in the predefined space, an adaptive bi-fold MREA has been design optimized to provide minimum dynamic range of about two at design impact speed of 5 m/s. The conventional SLG is then integrated with design optimized smart MREA to increase the energy dissipation of the skid landing gear for a sink rate of up to 4.5 m/s.

Based on the above circumstance, the present dissertation research was challenged by the objectives of increasing the energy absorption of the SLG system while adhering to the preset constraints on the size of the proposed device which are imposed by the design and assembly requirements of the helicopter. By the end of this work, the objective of protecting the occupants is fulfilled by design optimization a MREA device capable of dissipating the energy of the impact of up to 4.5 m/s. The device compactness makes it is simple to fit in the allocated space by restricting the travel of the piston to 20 cm. Thus, avoiding the end-stop impact and concurrently minimizing the sudden acceleration experienced by the payload in the event of impact.

To achieve the overall goal of the present research study, the research work has been conducted through several interrelated phases. These phases are briefly explained in the next points:

- **Phase I**: The dynamic responses of the baseline SLG system were determined to verify the SLG's utmost capability of impact energy dissipation. The helicopter was numerically modeled and drop tested in ABAQUS platform according to the testing and certification conditions provided in the crashworthiness standards AWM chapter 527 and FAR Part 27 for civilian helicopters. The FE model included detailed modeling of the SLG while the mass properties of the helicopter's reminder structure were lumped at the center of gravity. The dynamic responses of the model in terms of C.G. displacement, velocity, and the acceleration shows that the baseline SLG could survive the impact for sink rate of up to 2.44 m/s but with very low margin of safety from the ultimate design envelop. To increase the energy absorption capacity of the SLG without incurring weight penalty, the cross sectional dimensions of the crosstubes were optimized.

- **Phase II**: The relatively high stiffness of the baseline SLG could be relaxed further to allow more energy absorption. Hence, reduced the exposure of occupants to high abrupt acceleration. Moreover, the design optimization of the crosstubes could reduce the mass by 2.2 kg. The mass reduction permitted assembling the MREAs without encountering undesirable increase in the overall mass of the SLG system. Thus, complied with the general requirements of aircraft airworthiness. In chapter three, the sizes of the forward and aft crosstubes were optimized using sequential quadratic programming methodology. The objective was to maximize the specific energy absorption (SEA) of the cross members while adhering to the mass, maximum permissible vertical displacement, and the structural load factor constraints. In numbers, the crosstubes mass is constrained to be less than 9.06 kg, the C.G. is allowed to travel 350 mm, and the load factor is not permitted to exceed 3.5 g's. Instead of performing the design optimization using the finite element method based softwares, which are very expensive and their results are noisy, the design of experiment and the response surface methods were implemented. The optimization objective was successfully fulfilled. Moreover, external diameters of the crosstubes decreased by about 5 mm and the tube thickness by 0.5 mm in comparison to the original configuration (Design A). This resulted in a mass reduction of 2.2 kg and the elastic and in-elastic piecewise linear stiffness by 31% and 25%, respectively. The dramatic decrease in the stiffness increases the deflection and benefits increasing the SEA to 134.3% from 702 to 943 J/kg. Though both the baseline and the

optimum SLG designs meet the certification requirements for the skid landing gears of civilian helicopter, they cannot sustain impact loads at 2.46 m/s impact velocity and higher. To attenuate impact loads at higher sink rates, external energy dissipation devices should be incorporated in the system. In this and the preceding phase, new plots of the governing parameters of the rotorcraft, i.e. the effective mass, desired deflection and the sink rate have been introduced. The ready to use curves are established based on the simulation results of drop tests at different impact speeds and are intended to eliminate the need to perform enormous calculations prior to every drop test. With these curves, the testing team can specify the required effective helicopter mass to deflect the model to specific value at each single value of the sink rate.

- **Phase III**: In this phase, the bi-fold MREA was optimized to attain dynamic range of about two at 5 m/s impact velocity. In this study, the size, the 15 kN field-off stroking load, and the laminar flow in the MR passage constraints were successfully met. The MREA could generate controllable damping force of more than 14 kN. To accurately predict the dynamic behavior of the MREA at high impact velocity, the Bingham plastic model with minor loss factors was used. Two optimization approaches were used to obtain the optimization solution. First, the genetic algorithm technique was employed to search for the local optimum solution in the vicinity of the global solution. Second, the search was further refined using the sequential quadratic programming method to capture the global optimization solution. Based on the analysis results, the relationship between the yield damping force and the desired input current was derived to be used in the design of the semi-active control system.

- **Phase IV:** The SLG was equipped with the optimized MREA in a single degree of freedom helicopter model and the helicopter's responses were evaluated and compared to the responses of two models: Helicopter incorporating the conventional SLG and helicopter incorporating SLG equipped with passive EA. The SLG with passive EA was optimized either for attaining minimum acceleration or utilizing the full EA stroke. It was observed that the optimum damping coefficients under these conditions were different. This is attributed to the mono-objective nature of the passive EA devices which cannot handle these requirements concurrently. The incorporation of the tuneable MREA in the SLG, on the other hand, has met the set goals of achieving relatively low acceleration levels while utilizing the maximum

permissible EA stroke without encountering end-stop impact. The performance of the device was characterized in terms of two distinct Bingham numbers for compression and rebound strokes. With the system tuned to the optimum Bingham numbers, the device generated the desired damping force so that the soft landing could be attained at the end of the compression stroke and the payload returned to its original point of equilibrium with no oscillations at the end of the rebound stroke. In the compression stroke, the equivalent damping coefficients for configurations G and H were reduced by 23.4% and 27.3% in comparison to the respective coefficients of models D and F, respectively. It is noticeable that due the lowest stiffness of the optimum conventional SLG in design H, the MREA generated more damping force to attenuate the excessive energy in comparison to design G. In this phase, new charts have been introduced. These charts take into account the effect of the variation in the loading, which is expressed in rotor lift factor, on the generated damping force. This variation could be intentionally or accidently. However, such variation has major impact on the level of the acceleration experienced by the occupants and therefore, it should be controlled to minimize the impact of high acceleration on the backup structure and the seated occupants. The best way is to implement the charts in the semi-active control system.

- **Phase V**: The semi-active control system was proposed for use in versions G and H of the present SLG system. The semi-active controller design was based on the calculation of the optimum Bingham numbers for compression and rebound strokes. This makes the strategy simpler than the constant stroking load. The developed algorithm used the inverse model to determine the required input current based on the measured impact speed and the estimated helicopter mass. The current command was then supplied to the MREA to produce the desired MR yield force to ensure dissipating the entire impact energy by the end of the compression stroke. In designs G and H, the current inputs and hence the generated damping force in the loading (compression) stroke were different based on the amount of impact energy. In the rebound stroke, however, the semi-active control system programmed to supply constant and distinct current for each configuration because the MREA dissipated the elastic energy of the fully compressed spring no matter what is the impact velocity. Moreover, smooth return to the equilibrium position was attained as no oscillations were observed at the end of the rebound half cycle.

7.2 Contributions

The present dissertation research addresses the incorporation of the bi-fold MREA in the conventional skid landing gear system to meet the requirements of generating high damping force while ensuring that the device fit in the constrained space between the fuselage substructure and the SLG. Therefore, the thesis contributions can be summarized as follows:

I. In regard to the standalone conventional SLGs, studying the dynamical response of the under various drop testing conditions is made easy by avoiding tedious calculations before every drop test. This goal is achieved by using the impact governing parameters charts which enable the prediction of the required effective mass of the helicopter based on the test conditions of the permissible deflection and the desired impact velocity. These charts are produced based on two drop tests required by the crashworthiness regulations of civilian helicopters.

II. A design optimization strategy using combined DoE and RSM techniques has been developed to efficiently size optimize the conventional SLG. The developed strategy reduced substantially the cost of performing optimization studies on the commercial softwares such as ABAQUS. Also, it generated high accurate approximate results and eliminated the noisy outputs which are associated with the commercial results in the analysis of the highly nonlinear phenomenon such as in the analysis of impacting structures.

III. The present dissertation demonstrated the capability of the optimized bi-fold MREA of generating the desired high stroking load while maintaining the device's volume compact to fit in the allocated space between the fuselage subfloor structure and the SLG.

IV. The analysis of the helicopter as a single degree of freedom system has led to introducing a new chart called optimum Bingham number-rotor lift factor chart, or in short $Bi^o - L$ chart. This chart could be generated for compression as well as rebound stroke. The chart can directly estimate the required damping force to dissipate the impact energy which varies based on the activated rotor lift force in the instant of contact between the skids and the ground. This makes the process of generating the desired damping force fully automated to avoid the human errors in the activation of

the rotor lift force. Thus, reduces the abrupt acceleration transmitted to the payload. The charts can be used efficiently with the semi-active control systems.

7.3 Publications

The present research has resulted in several publications as:

Conference papers

1. M. Saleh, R. Bhat, and R. Sedaghati, "Crashworthiness Design Optimization of a Conventional Skid Landing Gear Using Response Surface Method," *Proc. The Canadian Society for Mechanical Engineering International Congress 2016*, June 26-29, 2016, Kelowna, BC, Canada. (published)

2. M. Saleh, R. Sedaghati, and R. Bhat, "Design Optimization of a Bi-Fold Magnetorheological Damper Subject to Impact Loads," *Proc. of The ASME 2017 Conference on Smart Materials, Adaptive Structures and Intelligent Systems*, September 18-20, 2017, Snowbird, Utah, USA. (Published)

3. M. Saleh, R. Sedaghati, R. Bhat, "Crashworthiness Study of a Helicopter Model Equipped with a Bi-Fold Magnetorheological Energy Absorber," *Proc. of The ASME 2017 Conference on Smart Materials, Adaptive Structures and Intelligent Systems*, September 18-20, 2017, Snowbird, Utah, USA. (Published)

Journal papers

1- Design Optimization of a Bi-Fold MREA Subjected to Impact loading for Skid Landing Gear Applications. Submitted to the *Journal of Intelligent Material Systems and Structures*.

2- Dynamic analysis of a SDOF helicopter model featuring skid landing gear and MR damper by considering rotor lift factor and Bingham number. Submitted to the *Journal of Smart Material and Structures.*

7.4 Recommendations for future work

While this research study has considerably advanced the state-of-the art in attenuating the impact load experienced by the rotorcraft skid landing gear using passive and adaptive energy absorption devices, there are still few important issues which deserve further future investigation as follows:

a. Using more realistic SLG model than the SDOF helicopter model. This means considering multi-degree of freedom systems which are encountered in impact attitudes other than the level one. The certification of the SLG system under the former attitudes are generally required by the more stringent crashworthiness standards such as the Military Standard of the US Army, MIL-STD 1290A (AV). This specification includes the drop test conditions with pitch and roll angles at impact velocity of up to 6.1 m/s. This broadens the applicability of the methods used in the current dissertation.
b. Conducting experimental drop tests on standalone conventional SLGs based on the charts of the impact governing parameters introduced in this thesis. The objective is to validate the charts experimentally.
c. Develop a semi-active control strategy that implements $Bi^o - L$ charts to achieve maximum protection in the event of impact by automating the generation of the optimum rotor lift and the damping forces.
d. Fabrication of the design optimized bi-fold MREA and testing under impact load conditions to better understand the effect of minor losses at different impact velocities.

References

[1] D. F. Shanahan, "Human Tolerance and Crash Survivability," Madrid, Spain, RTO-EN-HFM-113, 2004.

[2] SIMULIA INC., "Aircraft Survival Design guide-Volume III," Fort Eustis, VA, USA, Ad-A218 436, 1989.

[3] D. F. Shanahan, "Basic Principles of Helicopter Crashworthiness," Fort Rucker, AL, USA, USAARL Report No. 93-15, 1993.

[4] Guohua Li and Susan P. Baker, Eds., *Injury Research: Theories, Methods, and approaches, 1st Ed.* New York, USA: Springer, 2012.

[5] W. R. Mckenney, "Human Tolerance to Abrupt Acceleration: a Summary of the Literature," Phoenix, AZ, USA, Dynamic Science Report 70-13, May 1970.

[6] P. Minderhoud, "Development of Bell helicopter's model 429 sleigh type skid landing gear," in *AHS 64th Annual Forum*, Montreal, 2008.

[7] U.S. Army, "MIL-STD-1290A(AV)," Washington, D. C., 1989.

[8] A. Del Prete, T. Primo, G. Papadia, and B. Manisi, "Design for Manufacturing for Energy Absorption Systems," in *The 14th Inter. ESAFORM Conf. Mater. forming*, vol. 1353, Belfast, UK, 2011, pp. 1620-1625.

[9] FARs Part 27. [Online]. http://www.flightsimaviation.com/data/ FARS/part_27. html

[10] S. A. Mikhailov, L. V. Korotkov, S. A. Alimov, and D. V. Nedel'ko, "Modeling of landing gear of a helicopter with skid landing undercarriage with regard for the second landing impact," *Russian Aeronautics*, vol. 54, no. 3, pp. 247-253, 2011.

[11] Max Chernoff, "Analysis and Design of Skid Gears for Level Landing," *J. American Helicopter Society*, vol. 7, no. 1, pp. 33-39, 1962.

[12] C.-H. Tho, C. E. Sparks, A. K. Sareen, M. R. Smith, and C. Johnson, "Efficient Helicopter Skid Landing Gear Dynamic Drop Simulation Using LS-DYNA," *J. American Helicopter Society*, vol. 49, no. 4, pp. 483-492, Oct. 2004.

[13] A. K. Sareen, M. R. Smith, and J. V. Howard, "Helicopter Skid Gear Dynamic Drop Analysis and Test Correlation," in *54th Annual forum of AHS*, Washington, DC, USA, 1998, pp. 1267-1274.

[14] L. C. Williams and A. O. Bolukbasi, "A Nonlinear Analysis Methodology for the Design of Skid Landing Gears," in *AHS 48th Annual forum*, Washington, DC, USA, Oct. 1992, pp. 1451-1456.

[15] B. E. Stephens and W. L. Evans, "Application of Skid Landing Gear Dynamic Drop Analysis," in *AHS 55th Annual forum*, Alexandria, VA, USA, 1999, pp. 1644-1652.

[16] D.-H. Kim and Y.-S. Kim, "Nonlinear Impact Dynamic Analysis and Comparison with Experimental Data for the Skid Gear," *Int. J. Modern Physics B*, vol. 22, no. 9, 10 & 11, pp. 1403-1408, 2008.

[17] X. Élie-dit-Cosaque, A. Gakwaya, and J. Lévesque, "Design and Drop Test Simulation of a Helicopter Skid Landing Gear with Abaqus/CAE," in *2009 SIMULIA Customer Conf.*, London, England, 2009, pp. 1-15.

[18] Engineering Department, Passive Shock Isolation (Reprint).

[19] D. H. Wang and W. H. Liao, "Magnetorheological fluid Dampers: A Review of Parametric modelling," *Smart Mater. Struct.*, vol. 20, pp. 1-34, 2011.

[20] D. C. Batterbee, N. D. Sims, R. Stanway, and Z. Wolejsza, "Magnetorheological Landing Gear: 1. A Design Methodology," *Smart Mater. Struct.*, vol. 16, pp. 2429-2440, 2007.

[21] D. C. Batterbee, N. D. Sims, R. Stanway, and M. Rennison, "Magnetorheological Landing Gear: 2. Validation Using Experimental Data," *Smart Mater. Struct.*, vol. 16, pp. 2441-2452, 2007.

[22] X. Hengbo, F. Qin, G. Ziming, and W. Hao, "Experimental Investigation into Magnetorheological Damper Subjected to Impact Loads," *Trans. Tianjin Univ.*, vol. 14, pp. 540-544, 2008.

[23] Y.-T. Choi, R. Robinson, W. Hu, and N. M. Wereley, "Analysis and Control of a Magnetorheoligical Landing Gear System for a Helicopter," in *68th AHS Inter. Annual Forum & Tech. Display*, vol. 2, Fort Worth, TX, USA, 2012, pp. 850-858.

[24] M. Mao, W. Hu, N. M. Wereley, A. L. Browne, and J. C. Ulicny, "A Nonlinear Analytical Model for Magnetorheological Energy Absorbers Under Impact Conditions," in *ASME 2009 Conf. on Smart Mater., Adapt. Struct. and Intellig. Sys.*, Oxnard, CA, USA, 2009, pp. 1-12.

[25] M. Mao et al., "Experimental Validation of a Magnetorheological Energy Absorber Design Analysis," *J. Intell. Mater. Sys. Struct.*, vol. 25, no. 3, pp. 352-363, 2013.

[26] H. J. Singh, W. Hu, N. M. Wereley, and W. Glass, "Experimental Validation of a Magnetorheological Energy Absorber Design Optimized for Shock and Impact Loads," *Smart Mater. Struct.*, vol. 23, pp. 1-17, 2014.

[27] M. Mao, W. Hu, N. M. Wereley, A. L. Browne, and J. Ulicny, "Shock Load Mitigation Using Magnetorheological Energy Absorber with Bifold Valves," in *Industrial and Commercial Applications of Smart structures Technologies 2007*, vol. 652710, San Diego, CA, USA, 2007, pp. 652710-1 - 652710-12.

[28] M. Mao, W. Hu, Y.-T. choi, and N. M. Wereley, "A Magnetorheological Damper with Bifold Valves for Shock and Vibration Mitigation," *J. Intel. Mater. Syst. Struct.*, vol. 18, pp. 1227-1232, 2007.

[29] M. Mao et al., "Nonlinear Modeling of MR Energy Absorbers Under Impact Conditions," *Smart Mater. Struct.*, vol. 22, pp. 1-12, 2013.

[30] T. Belytschko, "On Computational Methods for Crashworthiness," *Computers & Structures*, vol. 42, no. 2, pp. 271-279, 1992.

[31] Aiwei Su, Analysis of Explosion Load Effects in Pipe-racks, 2012.

[32] J. Lonn and J. Navred, Drop Test of a Soft Beverage Package-Experimental Tests and a Parameter Study in ABAQUS, 2006.

[33] N. Jaksic and K.-F. Nilsson, Numerical Simulation of the One Meter Drop Test on a Bar for the Castor Cask-Initial ans Sensitive Analysis, 2007.

[34] ABAQUS INC. (2005) imechanica. [Online]. imechanica.org/files/0-overview%20Explicit.pdf

[35] E. L. Fasanella and K. E. Jackson, "Best Practices for Crash Modeling and Simulation," Washington, DC, USA, NASA/TM-2002-211944, 2002.

[36] *Atlas of stress and Strain Curves, 2nd Ed.* OH, USA: ASM International, 2002.

[37] D. Crist and L. H. Symes, "Helicopter Landing Gear Design and Test Criteria Invistigation," Fort Worth, TX, USA, USAAVRADCOM-TR-81-D-15, 1981.

[38] B. Milwitzky and D. C. Lindquist, "Evaluation of the Reduced-Mass Method of Representing Wing-Lift Effects in Free-Fall Drop Tests of Landing gears," Washington, DC, USA, Technical Note 2400, 1951.

[39] ABAQUS DOCs. [Online]. http://abaqusdoc.ucalgary.ca/books/usb/default.htm?startat=pt01ch02s03aus18.html

[40] M. Saleh, R. Sedaghati, and R. Bhat, "Crashworthiness Design Optimization of a Conventional Skid Landing Gear Using Response Surface Method," in *CSME International Congress 2016*, Kalowna, B.C., Canada, 2016.

[41] R. Vignjevic and M. J. Cavalcanti, "Numerical Simulation of the Lynx Helicopter Main Lift Frame Component Collapse," *Int. J. Crashworthiness*, vol. 2, no. 1, pp. 25-38, 1997.

[42] V. Dias da Silva, *Mechanics and Strength of Materials*. Coimbra, Portugal: Springer, 2006.

[43] G. K. Miller, "Failure Criteria for Evaluating Accidental Drops of Fuel Containers at INTEC," Lockheed Martin, Idaho Falls, Idaho, Rep. INEEL/EXT-98-01083, 1998.

[44] A. Airoldi and L. Lanzi, "Multi-Objective Genetic Optimization for Helicopter Skid Landing Gears," in *46th AIAA/ASME/ASCE/AHS/ASC Struct., Structural Dynamics & Mater. Conf.*, Austin, TX, USA, 2005, pp. 1-9.

[45] A. Airoldi and L. Lanzi, "Design of Skid Landing Gears by Means of Multibody Optimization," *J. Aircraft*, vol. 43, no. 2, pp. 555-563, 2006.

[46] C.-H. Tho and B. P. Wang, "An Effective Crashworthiness Design Optimization methodology to Improve Helicopter Landing Gear Energy Absorption," *J. AHS*, vol. 54, no. 4, pp. 042003-1 - 042033-10, 2009.

[47] K. Shrotri, Composite Skid Landing Gear Design Invistigation, August 2008.

[48] K. M. Carley, N. Y. Kamneva, and J. Reminga, "Response Surface Methodology," School of Computer Sci., Carnegie Mellon Univer., Pittsburgh, PA, USA, CASOS Technical Report CMU-ISRI-04-136, 2004.

[49] M. Papila and R. T. Haftka, "Response Surface Approximations: Noise, Error Repair, and Modeling Errors," *AIAA J.*, vol. 38, no. 12, pp. 2336-2343, 2000.

[50] C.-H. Tho, Crashworthiness Design Optimization Using Surrogate Models, August 2006, Ph.D. Dissertation.

[51] Minitab 17 User's Manual, 2016.

[52] J. Antony, *Design of Experiments for Engineers and Scientists, 1st Ed.* Burlington, MA, USA: Butterworth-Heinemann, 2003.

[53] M. Manohar, J. Joseph, T. Selvaraj, and D. Sivakumar, "Application of Box Behnken Design to Optimize the Parameters for Turning Inconel 718 Using Coated Carbide Tools," *Inter. J. Sci. & Eng. Research*, vol. 4, no. 4, pp. 620-642, April 2013.

[54] H. Ibrahim, Design Optimization of Vehicle Structures for Crashworthiness Improvement, 2009, Ph.D. Dissertation.

[55] J. S. Arora, *Introduction to Optimum Design, 3rd Ed.* Oxford, UK: Elsevier, 2012.

[56] W. W. Chooi and S. O. Oyadiji, "Mathematical Modeling, Analysis, and Design of Magnetorheological (MR) Dampers," *J. Vibration Acoustics*, vol. 131, pp. 061002-1 - 061002-10, Dec. 2009.

[57] A. G. Olabi and A. Grunwald, "Design and Application of Magneto-rheological Fluid," *Materials & Design*, vol. 28, pp. 2658-2664, 2006.

[58] J. D. Carlson, "MR Fluids and Devices in the Real World," *Inter. J. modern Physics B*, vol. 19, no. 7, 8 &9, pp. 1463-1470, 2005.

[59] M. Aslam, Y. Xiong-liang, and D. Zhong-chao, "Review of Magnetorheological (MR) Fluids and its Applications in Vibration Control," *J. Marine Sci. App.*, vol. 5, no. 3, pp. 17-29, Sep. 2006.

[60] E. M. Abouobaia, Hybrid Torsional Damper for Semi-Active Control of Torsional Vibration in Rotating Machines, Nov. 2015, Ph.D. Dissertation.

[61] P. P. Phule, Magnetorheological (MR) Fluids: Principles and Applications, Feb. 2001.

[62] S.-B. Choi and Y.-M. Han, *Magnetorheological Fluid Technology Applications in Vehicle Systems*. Boca Raton, FL, USA: CRC Press, 2013.

[63] F. M. White, *Fluid Mechanics, 4th Ed.*, Boston, U.S.A., 2003.

[64] J. C. Dixon, The Shock Absorber Handbook, 2nd Ed., 2007.

[65] MRF-132DG Magneto-Rheological Fluid. [Online]. https://www.lord.com/sites/./TechnicalDataSheet/DS7015_MRF-132DGMRFluid.pdf

[66] Q.-H. Nguyen, Y.-M. Han, S.-B. Choi, and N. M. Wereley, "Geometry Optimization of MR Valves Constrained in a Specific Volume Using the Finite Element Method," *Smart Mater. Struct.*, vol. 16, pp. 2242-2252, 2007.

[67] T. Planche, "ARIEL Dogleg Vertical Dipoles design note EHBT:MB0 & EHBT:MB5A," Document: 104392, Release No. 1, 2013.

[68] Y.-J. Nam and M.-K. Park, "Electromagnetic Design of a Magnetorheological Damper," *J. Intellig. Mater. Sys. Struct.*, vol. 20, pp. 181-191, 2009.

[69] Y.-T. Choi, R. Robinson, W. Hu, and N. M. Wereley, "Analysis and Control of a Magnetorheological Landing Gear System for a Helicopter," *J. American Helicopter Society*, vol. 61, pp. 032006-1 - 032006-8, 2016.

[70] A. Hadadian, R. Sedaghati, and E. Esmailzadeh, "Design Optimization of Magnetorheological Fluid Valves Using Response Surface Method," *J. Intellig. Mater. Sys. Struct.*, vol. 25, no. 11, pp. 1352-1371, 2014.

[71] H. J. Singh and N. M. Wereley, "Adaptive Magnetorheological Shock Isolation Mounts for Drop-Induced Impacts," *Smart Mater. Struct.*, vol. 22, pp. 1-10, 2013.

[72] N. M. Wereley and L. Pang, "Nondimensional Analysis of Semi-active Electrorheological and Magnetorheological Dampers Using Approximate Parallel Plate Models," *Smart Mater. Struct.*, vol. 7, pp. 732-743, 1998.

[73] P-T. D. Spanos, Linearization Techniques for Non-Linear Dynamical Systems, 1977, Ph.D. Dissertation.

[74] T. K. Caughey, "Equivalent Linearization Techniques," *J. Acoustical Society America.*, vol.35, no. 11 pp. 1706-1711, 1963.

[75] J. Y. Wang, Y. Q. Ni, J. M. Ko, and Jr. B. F. Spencer, "Semi-Active TLCDS Using Magnetorheological Fluids for Vibration Mitigation of Tall Buildings," *Advances in Bulding Tech.*, vol. 1, pp. 537-544, 2002.

[76] C. Yue, Control Law Designs for Active Suspensions in Automotive Vehicles, 1998, M.S. Thesis.

[77] H. R. Karimi, "A Semi-active Vibration Control Design for Suspension Systems with MR Dampers," in *Vibration Analysis and Control - New Trends and Developments*.: InTech, 2011, pp. 115-130.

[78] A. Bolukbasi et al., "Rotorcraft Active Crash Protection Systems," in *67th AHS Annual forum*, Virginia Beach, VA, USA, 2011, pp. 906-918.

[79] F. D. Goncalves, Dynamic Analysis of Semi-Active Control Techniques for Vehicle Applications, 2001, M.Sc. Thesis.

[80] G. M. Mikulowski, Adaptive Impact Absorbers Based on Magnetorheological Fluids, 2008, Ph.D. Dissertation.

[81] G. Wang, G. Hiemenz, W. Hu, and N. M. Wereley, "A Constant Stroking Load Regulator for Shock Absorption," in *The ASME 2011 Conference on Smart Materials, Adaptive Structures and Intelligent Systems*, Scottsdale, AZ, USA, 2011, pp. 1-8.

[82] G. M. Mikułowski and J. Holnicki-Szulc, " Adaptive Landing Gear Cncept—Feedback Control Validation," *Smart Mater. Struct.*, vol. 16, pp. 2146-2158, 2007.

[83] H. J. Singh and N. M. Wereley, " Influence of Occupant Compliance on a Vertically Stroking Helicopter Crew Seat Suspension," J. Aircraft., vol. 52, no. 4, pp. 1286-1297, 2015.